Spatial and Temporal Changes of the Photospheric Magnetic Field in Solar Flares

Nawal Abed M Alanazi

SUBMITTED IN FULFILMENT OF THE REQUIREMENTS FOR THE DEGREE OF
DOCTOR OF PHILOSOPHY

SCHOOL OF PHYSICS AND ASTRONOMY

COLLEGE OF SCIENCE AND ENGINEERING

MAY 2026

In memory of my father, Abed, the strongest and kindest man I have ever known. You were my greatest encouragement. This work is dedicated to you, with endless love and gratitude.

Abstract

Solar flares are understood to be driven by the rapid release of energy in the solar corona through magnetic reconnection. However, the response of the photospheric magnetic field to this process remains not fully clear, particularly in terms of its temporal and spatial relationship with chromospheric emission and signatures of coronal energy release. This thesis investigates the evolution of the photospheric magnetic field during solar flares, with a focus on its association with flare ribbon emission and coronal energy-release signatures.

Using observations from the Solar Dynamics Observatory (SDO), including the Helioseismic and Magnetic Imager (HMI) and Atmospheric Imaging Assembly (AIA), we analyse multiple flare events through high-cadence magnetograms and ultraviolet imaging. In the first study (Chapter 3), we examine the spatially and temporally varying line-of-sight magnetic field within flare ribbon regions for six M-class flares. These regions trace the chromospheric footpoints of reconnecting coronal magnetic field lines. We find that in four out of six events, the changes in the line-of-sight magnetic field precede the UV emission by several minutes on average. In addition to previously reported monotonic changes, oscillatory variations are detected, suggesting the presence of non-flare-related signals. In addition, a moderate correlation is identified between magnetic field strength and its rate of change, indicating that stronger fields evolve more rapidly.

To establish more general behaviour, and motivated by the need to characterise the full magnetic vector, in Chapter 4, we extend the analysis to the horizontal magnetic field component (B_h), which is expected to respond strongly to flare-related magnetic restructuring. A sample of 35 flares spanning C-, M-, and X-class events is analysed using unsupervised

machine learning (k-shape clustering) to identify regions exhibiting step-like changes in $\boldsymbol{B}_h$. We find that in 14 events, stepwise increases in $\boldsymbol{B}_h$ are concentrated near polarity inversion lines and are closely associated in space and time with the onset of flare ribbon emission. The peak rate of increase of $\boldsymbol{B}_h$ generally lags the ultraviolet brightening by several minutes, with no statistically significant dependence on flare class. Furthermore, the time lag increases systematically with distance from the polarity inversion line, while decreases in $\boldsymbol{B}_h$ are more spatially dispersed. The outward progression of $\boldsymbol{B}_h$ enhancements provides strong observational evidence for a photospheric response to the sequential relaxation and downward contraction of coronal magnetic fields during energy release, consistent with the coronal implosion scenario.

Finally, the relationship between photospheric magnetic evolution and coronal energy release is examined using the time derivative of the GOES soft X-ray flux as a proxy (Chapter 5). The timing of magnetic field changes is found to closely coincide with impulsive energy release, with delays around 2 minutes, indicating near-simultaneous evolution. Spatially, these changes also exhibit an outward progression from the polarity inversion line.

Overall, these results show that photospheric magnetic changes are closely linked to flare ribbon emission and impulsive coronal energy release. Increases in the horizontal magnetic field near polarity inversion lines are consistent with coronal field contraction, supporting the coronal implosion scenario and improving our understanding of how energy is transferred through the solar atmosphere.

Contents

List of Tables

List of Figures

Acknowledgements

I would like to express my deepest gratitude to my supervisor, Prof. Lyndsay Fletcher, for her continuous support throughout the past three and a half years. Her guidance introduced me to the field of solar physics and encouraged me to explore the use of machine learning in my research. She also supported me in writing my first paper and showed great patience throughout my learning process. She has been a true role model, and I feel honoured to have completed my PhD under her supervision.

I would also like to thank my second supervisor, Dr Iain Hannah, for his valuable discussions during my annual progress review meetings. My sincere thanks also go to Dr Hugh Hudson for his helpful discussions and scientific insight.

I am grateful to all the PhD students in Room 604 for their support and assistance whenever I needed help.

I would like to express my heartfelt gratitude to my beloved husband Bader, who moved across the world with me to support my PhD journey. This work would not have been possible without your constant encouragement and support. To my son, Wesam, thank you for bringing joy and motivation into my life.

Finally, I would like to thank my mother, my sisters and my brothers for their continuous support and encouragement. I am especially grateful to my friends, who believed in me, supported me and kept me motivated.

I am also sincerely grateful to King Saud University for providing me with the opportunity to pursue my studies abroad and to the Saudi Embassy for their support during my PhD.

Declaration

I declare that, except where explicit reference is made to the contribution of others, that this dissertation is the result of my own work and has not been submitted for any other degree at the University of Glasgow or any other institution

---

Nawal Abed M Alanazi

Chapter 1

Introduction

Section 1.3 is based on material published in Alanazi and Fletcher (2025) and Alanazi and Fletcher (2026).

1.1 The Sun

The Sun is a G-type main-sequence star that contains more than 99% of the total mass of the Solar System and serves as the primary source of energy for the Earth. It has a radius of $\sim 6.96 \times 10^8$ m, a mass of $\sim 1.99 \times 10^{30}$ kg, and a luminosity of $\sim 3.8 \times 10^{26}$ W. Energy in the Sun is generated through nuclear fusion reactions in its core, where hydrogen is converted into helium. The Sun lies at an average distance of ~ 149.6 million km from Earth. As the closest star to our planet, it strongly influences the space environment and modern technological systems, highlighting the importance of understanding solar activity.

1.1.1 The Solar Atmosphere

The solar atmosphere is the outer region of the Sun, extending above its visible surface and consists of four main layers. Figure 1.1 shows the variation of temperature and plasma density across the layers of the solar atmosphere. Although the plasma density continuously decreases with height, the temperature rises sharply in the transition region and corona. The lowest layer is the photosphere, the visible surface of the Sun, where the temperature decreases with height from approximately ~ 6500 K at the base to about ~ 4500 K at the top, with a thickness of approximately ~ 0.5 Mm. The photosphere also contains features known as sunspots, which are regions of strong magnetic fields. Above the photosphere lies the chromosphere, an optically thick layer in which the temperature initially decreases and then rises with height. It is observed in spectral lines such as Hα and in the ultraviolet. It has a thickness of ~ 2.5 Mm and a temperature of $\sim 10^4$ K. Above the chromosphere is a thin transition region, where the temperature increases rapidly over a short distance from tens of thousands of kelvin to more than one million kelvin. The corona is a hot and highly structured region with temperatures of about 1–3 MK, where the plasma is strongly influenced by magnetic fields and where many dynamic phenomena occur.

1.1.2 Solar Magnetic Fields

The Sun's magnetic field plays a fundamental role in shaping the structure and dynamics of the solar atmosphere. It is believed to originate from a dynamo process operating in the solar interior, where the combined effects of differential rotation and convective motions in the convection zone generate and amplify magnetic fields (Priest, 2014; Charbonneau, 2014). These magnetic fields rise through the convection zone and emerge at the photosphere in the form of concentrated magnetic flux, forming bipolar structures associated with sunspots and active regions (Solanki, 2003). Once in the solar atmosphere, magnetic

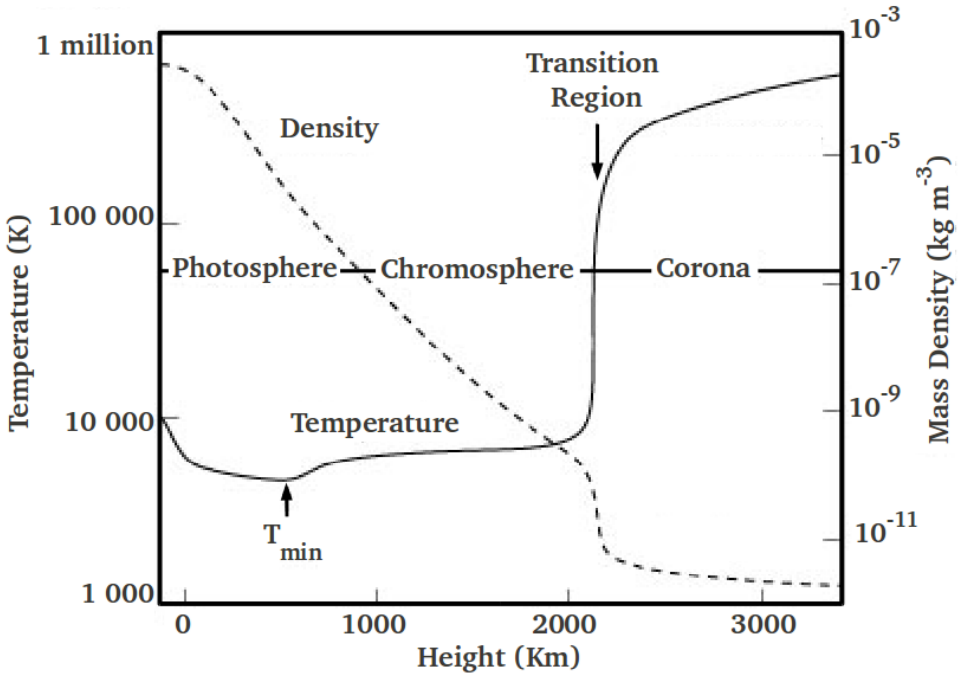

Figure 1.1: Schematic representation of the variation of plasma temperature and density with height in the solar atmosphere. Adapted from Lang (2001).

field lines extend into the chromosphere and corona as loops that confine and guide the motion of the hot plasma. This confinement arises because the plasma is highly ionised and conductive, so magnetic field lines are effectively frozen into the plasma, forcing charged particles to move primarily along them (Aschwanden, 2004). Through processes such as twisting, shearing, and stressing by photospheric motions, the magnetic field is moved away from its potential state, generating electric currents in the plasma and leading to the gradual buildup of magnetic free energy that can be released during energetic events such as solar flares.

In addition to these large-scale fields, small-scale magnetic fields are widely observed in the quiet Sun, particularly in internetwork regions where they are weak, mixed in polarity, and highly dynamic, suggesting that they are generated locally by near-surface convective processes (De Wijn et al., 2009).

1.1.3 Active Regions

Solar active regions are areas on the solar surface characterised by strong and complex magnetic fields. They usually appear as groups of sunspots, which are darker and cooler regions of the photosphere formed where intense magnetic fields inhibit the transport of convective heat (Solanki, 2003). An example of a solar active region is shown in Figure 1.2, where panel (a) displays the continuum intensity image obtained by the Helioseismic and Magnetic Imager (HMI) aboard the Solar Dynamics Observatory (SDO), revealing the sunspot structure, including the dark umbra and the surrounding brighter region known as the penumbra. Panel (b) shows the corresponding line-of-sight magnetogram, where black and white regions represent opposite magnetic polarities, corresponding to negative and positive line-of-sight magnetic field, respectively, illustrating the distribution of magnetic flux across the active region (see Section 2.1.1 for further details on magnetograms). Panel (c) presents an extreme ultraviolet (EUV) image from the Atmospheric Imaging Assembly (AIA) at 171 Å, highlighting the coronal loops that trace the magnetic field connecting regions of opposite polarity.

Therefore, active regions exhibit bipolar magnetic structures consisting of areas of opposite magnetic polarity connected by coronal magnetic loops, as seen in Figure 1.2(c). The boundary separating opposite polarities is known as the polarity inversion line (PIL), where magnetic shear and strong gradients in the magnetic field often develop. These conditions allow magnetic energy to accumulate in the coronal magnetic field, making active regions the primary sites for energetic solar phenomena such as solar flares and coronal mass ejections (Priest, 2014).

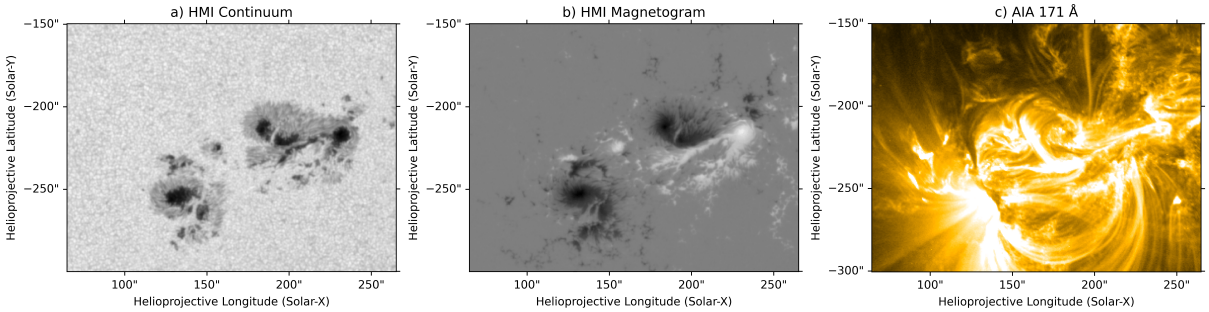

Figure 1.2: Example of a solar active region (NOAA AR 11158) observed by the Helioseismic and Magnetic Imager (HMI) onboard the Solar Dynamics Observatory (SDO). (a) Continuum intensity image showing the sunspot structure. (b) Line-of-sight magnetogram illustrating the bipolar magnetic field distribution, where white and black represent opposite magnetic polarities. (c) EUV image from AIA at 171 Å highlighting the coronal loops that trace the magnetic field connecting regions of opposite polarity.

1.2 Solar Flares

Solar flares, which Carrington and Hodgson first observed in 1859 (Carrington, 1859; Hodgson, 1859), are among the most energetic and dynamic phenomena observed on the Sun, characterised by sudden and localised enhancements of electromagnetic emission throughout the solar atmosphere. They occur over a wide range of magnitudes classified according to their peak soft X-ray (SXR) flux at 1–8 Å as measured by GOES (the Geostationary Orbiting Environmental Satellites) operated by the National Oceanic and Atmospheric Administration (NOAA). They are classified into A, B, C, M and X classes, where each class represents an order-of-magnitude increase in X-ray flux, with X-class flares being the most energetic. A summary of this classification is provided in Table 1.1. The energy released during solar flares can vary greatly between events, with smaller-scale flares occurring much more frequently than major ones (e.g. Crosby et al., 1993). Solar flares are three-dimensional events that involve the coupled response of the solar atmosphere from the photosphere to the corona. They are powered by the rapid release of magnetic energy stored in stressed and non-potential magnetic fields within active regions. Typical flares release energies of order 10^{29}–10^{32} erg over timescales of minutes (Shibata and Magara, 2011).

Flare Class	SXR Flux (W m^{-2})
A	$< 10^{-7}$
B	10^{-7} – 10^{-6}
C	10^{-6} – 10^{-5}
M	10^{-5} – 10^{-4}
X	$> 10^{-4}$

Table 1.1: GOES soft X-ray (1–8 Å) flare classification based on peak flux levels, as defined by the NOAA/GOES operational system.

Flares are multi-wavelength events that span radio to hard X-rays and gamma rays (Fletcher et al., 2011). At radio wavelengths, observations provide important diagnostics of accelerated electrons and plasma processes in the solar atmosphere. During a radio burst, the solar radio irradiance may increase by several orders of magnitude (Benz, 2017). At optical wavelengths, flare emission is concentrated in small footpoints and occasionally in ribbon structures, as first observed by Carrington and Hodgson, where these regions mark where much of the flare energy is deposited and radiated. At shorter wavelengths, ultraviolet and extreme-ultraviolet observations reveal the chromospheric and coronal response to flare energy release, mostly through the appearance of bright elongated structures called flare ribbons that mark the footpoints of newly reconnected magnetic field lines (Fletcher et al., 2011). At even higher energies, X-ray observations show intense bursts of emission from hot plasma and accelerated particles, with soft X-rays tracing thermal emission from heated coronal loops and hard X-rays indicating non-thermal electron acceleration (Lin, 2011).

1.2.1 Standard Eruptive Flare Models

The standard model explaining how solar flares form is illustrated in Figure 1.3, referred as the CSHKP flare model (Carmichael, 1964; Sturrock, 1966; Hirayama, 1974; Kopp and Pneuman, 1976). In this framework, a solar flare is initiated by the destabilisation and upward eruption of a magnetic flux rope or prominence, which stretches the overlying coronal magnetic field and leads to the formation of a vertical current sheet beneath the erupting structure. Then, plasma inflows from either side of the current sheet converge

toward a localised diffusion region where magnetic reconnection occurs, changing the magnetic connectivity and rapidly releasing stored magnetic energy. This energy is converted into plasma heating, bulk flows, and the acceleration of non-thermal particles (e.g. Miller et al., 1997; Zharkova et al., 2011). The newly reconnected field lines are expelled from the reconnection site as two directional outflows: upward flows contribute to the expansion of the eruption and may drive a coronal mass ejection, while downward-directed flows form newly closed magnetic loops in the corona. When accelerated particles (typically electrons in the standard beam model) travel along these field lines and impact the dense chromosphere, they deposit energy that heats the chromosphere and produces bright chromospheric flare ribbons and drives the upward expansion of heated plasma into the corona through chromospheric evaporation (e.g. Cheng et al., 1983; Mariska et al., 1989). However, energy transport may also occur via alternative mechanisms, such as Alfvén waves (Fletcher and Hudson, 2008). Overall, the CSHKP model provides a coherent framework linking coronal magnetic reconnection, plasma flows, shock formation, and the observed multi-wavelength signatures of solar flares.

It is worth noting that not all flares follow this two-ribbon configuration, in some cases, flares occur in more complex magnetic topologies, such as the spine–fan configuration associated with magnetic null points, where a central polarity is surrounded by opposite polarity, producing a circular polarity inversion line (e.g. Priest and Titov, 1996; Aulanier et al., 2000; Wyper et al., 2017). However, the flares studied in this work are predominantly two-ribbon events and are therefore well described by the standard CSHKP model.

While the CSHKP model captures the essential physics of eruptive flares, it can not fully describe the complex three-dimensional magnetic topology of solar flares. In three-dimensional extensions of the standard flare model, magnetic reconnection occurs along extended quasi-separatrix layers (QSLs), whose photospheric footprints form J-shaped

structures that coincide with flare ribbons and localised electric currents (Janvier et al., 2014). Together, the two-dimensional and three-dimensional models emphasise that solar flares are highly dynamic processes, where the geometry and rate of magnetic reconnection evolving in time, naturally giving rise to different phases during the flare evolution.

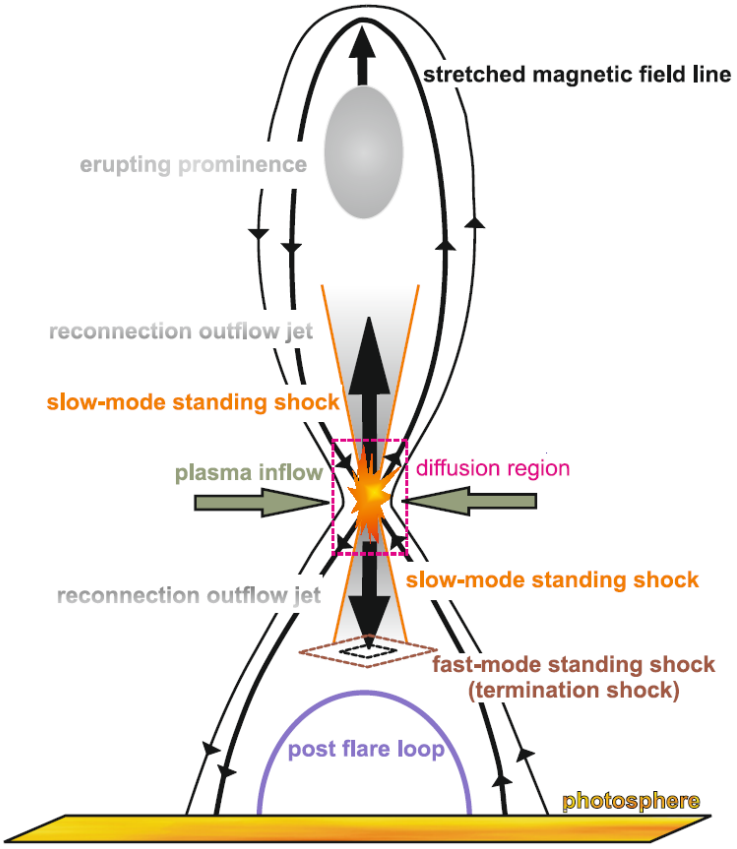

Figure 1.3: Schematic of the CSHKP model showing how emerging magnetic fields become unstable, driving plasma flows that force field lines to reconnect and release energy as a solar flare. Taken from Mann et al. (2009).

1.2.2 Flare Phases

The temporal evolution of solar flares varies from one event to another, with durations ranging from a few seconds to several hours, depending on the magnitude and magnetic configuration of the flare (Fletcher et al., 2011; Benz, 2017). This temporal evolution is often divided into three main phases. These phases are typically identified from the soft X-ray light curves recorded by the GOES satellites.

- **Pre-flare phase:** The flare is often preceded by a short pre-flare phase, observed in soft X-rays and lasting a few minutes, which may represent the onset of magnetic instability (Fletcher et al., 2011; Veronig et al., 2002b; Sterling and Moore, 2005). This phase is typically characterised by weak SXR emission and small-scale brightenings occurring shortly before the impulsive phase.
- **Impulsive phase:** The impulsive phase is characterised by a rapid release of magnetic energy, intense particle acceleration, and strong bursts of hard X-ray and radio emission (Holman et al., 2011). During this phase, flare ribbons appear and rapidly brighten in the chromosphere, while energetic electrons deposit energy in the lower atmosphere and drive chromospheric evaporation that fills newly formed coronal loops with hot plasma (Fletcher et al., 2011).
- **Gradual phase:** After the impulsive phase, the flare enters the gradual phase, also referred to as the decay phase, where thermal emission from hot coronal loops dominates the soft X-ray and EUV radiation. During this stage, the flare loops cool and gradually fade while the magnetic configuration relaxes toward a more stable state (Shibata and Magara, 2011).

These phases provide an observational framework for understanding the temporal evolution of flare energy release.

1.2.3 Flare Ribbons as Tracers of Magnetic Reconnection

Flare ribbons serve as visible markers of the chromospheric endpoints of magnetic field lines that undergo reconnection in the Sun's corona. They appear as bright, elongated structures in the chromosphere and are often observed in ultraviolet and extreme-ultraviolet wavelengths. Typically, flare ribbons form in pairs on opposite sides of the magnetic po-

larity inversion line (PIL) within solar active regions (Li and Zhang, 2009). However, more complex ribbon morphologies are also observed in many flares. In the standard flare model, these ribbons correspond to the chromospheric footpoints of newly reconnected magnetic field lines in the corona.

As a flare evolves, flare ribbons typically move away from the magnetic polarity inversion line. This apparent ribbon separation reflects the progressive reconnection of magnetic field lines at increasing heights in the corona, as predicted by the standard flare model, producing the observed motion of the ribbons (Qiu et al., 2017). An example of this behaviour is shown in Figure 1.4, where the temporal evolution of flare ribbons is mapped onto the underlying photospheric magnetic field (Qiu, 2009). In addition, the speed of ribbon separation which is typically of the order of a few to several tens of km s^{-1} (Hinterreiter et al., 2018), combined with measurements of the local photospheric magnetic field strength, can be used to estimate the magnetic reconnection rate and the rate of magnetic flux transfer which is order $\sim 10^{18}$–10^{19} Mx s^{-1} during flares (Qiu et al., 2004b).

In this thesis, flare ribbons are used as spatial tracers of magnetic reconnection. In particular, Chapter 3 focuses on analysing the spatial and temporal evolution of flare ribbons to study their connection with magnetic field changes during solar flares.

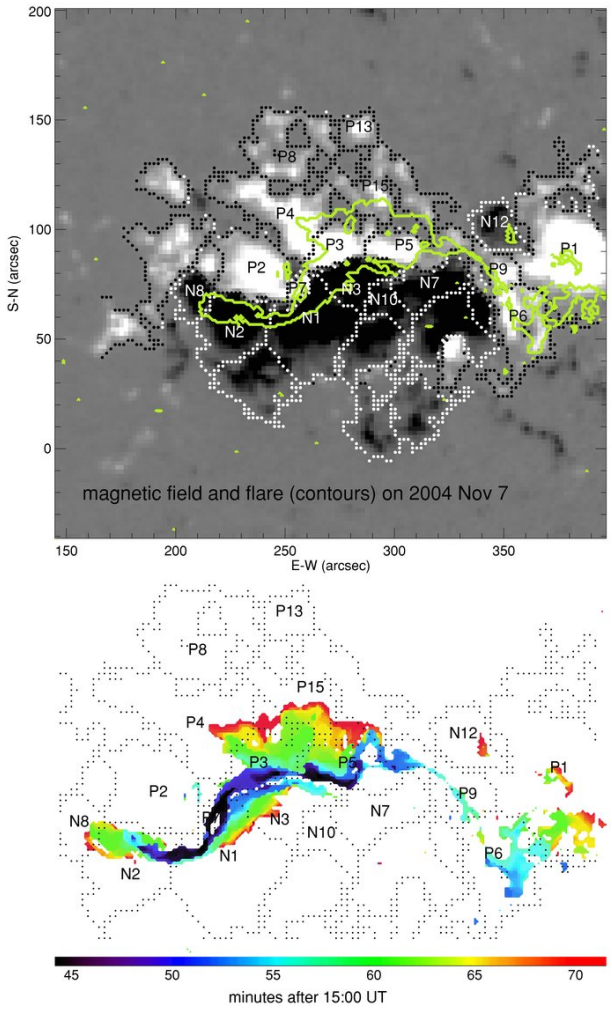

Figure 1.4: Example of flare ribbon evolution during the 2004 November 7 solar flare. Top panel: photospheric magnetic field with contours outlining flare ribbon locations. Bottom panel: colour-coded map showing the temporal progression of flare ribbon brightening, where colours indicate the time of ribbon appearance after 15:00 UT. The expansion of the ribbons away from the polarity inversion line reflects the progressive reconnection of magnetic field lines in the corona. Adapted from Qiu (2009).

1.3 Magnetic Field Changes During Flares

Since the coronal magnetic field is rooted in the photosphere, the restructuring of the coronal magnetic field has a photospheric imprint (Hudson, 2011). Numerous studies have reported abrupt and permanent changes in solar flares. Examples of these changes are illustrated in Figure 1.5, which shows both abrupt variations in the line-of-sight magnetic field (B_{los})and spatially localised changes in the horizontal magnetic field. The following subsections provide a detailed review of the observational and theoretical studies that have explored these photospheric magnetic field changes during flares.

1.3.1 Observation of Magnetic Field Changes

Early observational studies identified evidence for changes in the photospheric magnetic field during solar flares. Tanaka (1978) reported one of the first detections of such changes, reporting that magnetic field changes appeared before the onset of any Hα brightenings. Later, Sudol and Harvey (2005) conducted the first systematic study of abrupt, step-like magnetic field changes, characterised by fitting a step-function to time series of magnetic fields in magnetograms from the Global Oscillation Network Group (GONG). They demonstrated that these changes were both rapid and permanent, usually occurring over timescales of less than 10 minutes, with amplitudes of order $\sim$ 30–300 G. These changes primarily occur in the sunspot penumbra and, less frequently, in the umbra, and are found to be spatially and temporally coincident with flare UV emission within one to a few minutes.

Subsequent studies built on their findings, with numerous investigations applying the step-function method further to examine field changes (e.g. Petrie and Sudol, 2010; Cliver et al., 2012; Kleint, 2016; Wang et al., 2019; Liu et al., 2018; Castellanos Durán et al., 2018; Liu et al., 2022; Yadav and Kazachenko, 2022; Ferrente et al., 2023). These studies

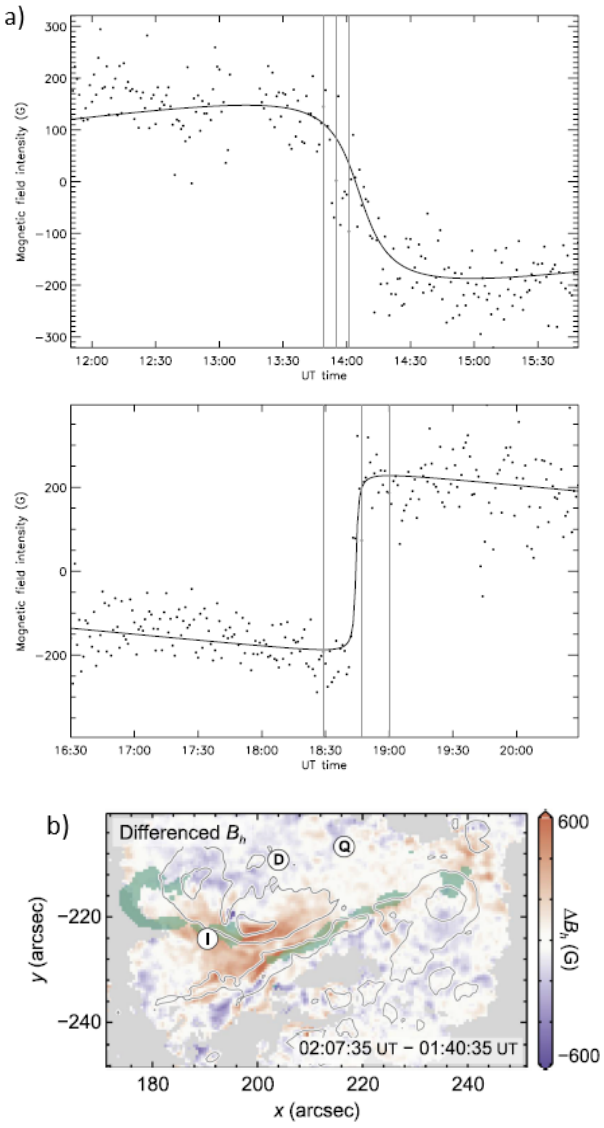

Figure 1.5: Examples of photospheric magnetic field changes during solar flares. (a) Time series of the line-of-sight magnetic field showing abrupt, step-like and permanent changes during flare events, with vertical lines indicating GOES soft X-ray timings (start, peak, and end) (Petrie and Sudol, 2010). (b) Difference map of the horizontal magnetic field (ΔB_h), showing spatially localised changes concentrated near the polarity inversion line (Sun et al., 2017).

show that the most changes occur in the horizontal magnetic field component (B_h), which exhibits permanent, step-like increases of order $\sim$ 100–300 G, typically concentrated near the magnetic polarity inversion line (PIL). In contrast, changes in the vertical magnetic field component are generally less pronounced and tend to be distributed in smaller, more fragmented patches across the active region (Yadav and Kazachenko, 2022). Additionally, variations in the line-of-sight magnetic field have been reported, with rates of change of approximately 20.7 Mx cm^{-2} min^{-1} (Castellanos Durán et al., 2018).

In addition to establishing the presence of abrupt magnetic field changes, several studies have investigated their spatial and temporal relationship with flare emission. Johnstone et al. (2012) evaluated individual pixels from an active region and focussed on fields exhibiting step-like changes in longitudinal field. Using 1600Å images from the Transition Region and Coronal Explorer satellite, and GONG magnetograms for four X-class solar flares, they found that chromospheric emission and photospheric field changes were spatially coincident, and the start of the photospheric field changes tended to lag that of the chromospheric UV emission by 4-9 minutes. They proposed that the temporal relationship was due to energy transport by an Alfvénic disturbance transmitted through the atmosphere. This starts heating the chromosphere at a lower wave energy, but the photospheric signature is only seen later on when sufficient wave energy can penetrate the steep atmospheric gradient in the Alfvén speed and disturb the photosphere. Such a scenario differs from energy deposition by energetic particles, where chromospheric heating is expected to occur rapidly and locally at the particle precipitation sites, often closely associated with hard X-ray footpoint emission. In contrast, Alfvénic energy transport may produce more gradual downward propagation of energy and delayed photospheric responses as the wave energy penetrates into deeper atmospheric layers. In the visible domain, Durán and Kleint (2020) found that white-light emission and step-like line-of-sight magnetic field changes are spatially linked and often overlap. However, they do not provide any information about the timing relationship.

Similarly, other studies have examined the relationship between magnetic field changes and high-energy flare emission. Hard X-rays are expected to be more strongly correlated in time than UV emission is with the energy release in flares, so Burtseva et al. (2015) studied the link between GONG magnetic field variations and HXR emission for X-class flares. They found that chromospheric HXR emission was well-correlated spatially with locations of strong field changes at the beginning of the flare, but later on this spatial correspondence was not so strong. But in contrast to UV, the observed start of the field changes tended to lead, or be coincident with, the start of the HXRs, and the peak amplitude of the field change tended to lead the HXR peak by a few minutes. They explained that the formation of a current sheet could lead to substantial magnetic field changes prior to reconnection and the main particle acceleration phase, assumed by them to be in the corona.

With the availability of vector magnetic field measurements, later studies also examined the behaviour of the horizontal magnetic field component during flares. Using vector field measurements rather than B_{LoS}, Sun et al. (2017) investigated rapid changes in the horizontal component of the magnetic field (B_h) during major flare X class using the HMI. They reported that the largest increases in B_h in one part of the active region tended to occur well before the SXR and HXR peaks, but another part of the same region exhibited a significant number of delayed responses, showing that the midpoint of the field change could occur more than ten minutes after the SXR peak. They also found that almost all selected pixels ($\sim 99\%$), identified based on significant step-like magnetic field changes, began to change during the flare, with onset times occurring within approximately 22 minutes after the flare onset. It is important to note that this percentage refers to a subset of strong-field pixels exhibiting clear magnetic changes, rather than all pixels within the active region. Yadav and Kazachenko (2022) also investigated the vector field and found that UV emission starts 4-19 minutes before the start of vector changes in the photosphere magnetic field, a similar behaviour to that seen by Sudol and Harvey (2005), Johnstone et al. (2012) and also by Liu et al. (2022).

Finally, several studies have explored the relationship between magnetic reconnection, energy release, and the transfer of magnetic flux during solar flares. Coronal magnetic reconnection is expected to liberate energy to form the flare ribbons and also to launch magnetic disturbances, and several studies have shown a strong spatial and temporal correlation between the reconnected flux transfer rate and HXR emission (e.g. Qiu et al., 2004a; Miklenic et al., 2009). However, Naus et al., 2022 showed that the peak of the total flux transfer rate leads both the peak in the AIA 1600 Å light curve, and the peak in the HXR lightcurves by several minutes.

Overall, these observational studies demonstrate that photospheric magnetic field changes are closely linked to flare energy release and provide important insight into the coupling between coronal magnetic reconnection and the lower solar atmosphere. In addition, the temporal relationship between magnetic field changes and flare emission is not uniform: in some cases, magnetic field changes are observed to precede flare signatures, while in others they lag behind. This variation partly reflects differences in how flare onset is defined, which depends on the wavelength and sensitivity of the observing instrument, as well as the background emission level. As a result, care must be taken when interpreting the timing between magnetic field changes and flare signatures.

1.3.2 The Nature of the Magnetic Field Changes

It has been known that the evolution of the photospheric magnetic field can be interpreted within the framework of the coronal implosion scenario proposed by Hudson (2000) and further discussed by Hudson et al. (2008). In this model, the release of magnetic free energy during a solar flare reduces the magnetic pressure in the corona, leading to a contraction or "*implosion*" of the coronal magnetic field. This contraction results in a restructuring of the photospheric magnetic field, particularly near the polarity inversion line (PIL), as illustrated in Figure 1.6. On the other hand, magnetic fields farther from the PIL may become more vertical during the post-flare restructuring of the active region

in some regions, reflecting changes in the surrounding magnetic topology. Observational evidence supporting this behaviour was reported by Wang and Liu (2010), who found that flare-associated decay of peripheral penumbrae is consistent with a transition of the magnetic field toward a more vertical configuration after flares, although the underlying physical mechanism remains uncertain.

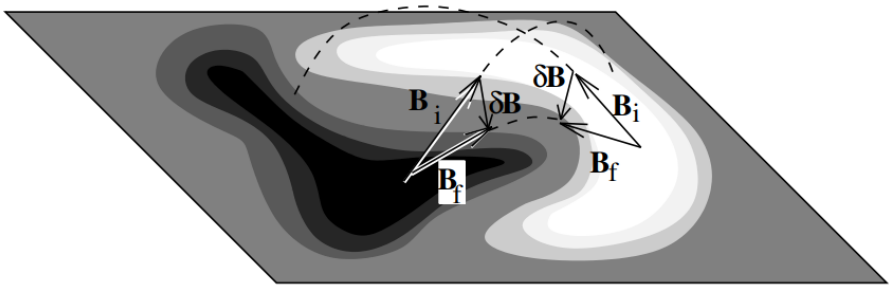

Figure 1.6: Conceptual illustration of flare-associated magnetic field changes near the polarity inversion line (PIL). The magnetic field vector changes from an initial state $\boldsymbol{B_i}$ to a final state $\boldsymbol{B_f}$, producing a difference $\boldsymbol{\delta B}$. Such changes are interpreted in terms of the coronal implosion scenario, where the release of magnetic energy during a flare causes the coronal magnetic field to contract, leading to an increase in the horizontal component of the photospheric magnetic field near the PIL. Adapted from Hudson et al. (2008).

1.3.3 Polarity Inversion Line

The magnetic field configuration near the polarity inversion line (PIL) plays a key role in the storage and release of magnetic energy during solar flares. In the 2D model and its extension into 3D, the behaviour of the magnetic field around the PIL is particularly important in the context of energy release. The “implosion” concept proposes that the release of flare magnetic energy is accompanied by a shrinkage of the magnetic field (Hudson, 2000). This can be interpreted in two ways (i) as a contraction of ‘peripheral’ or overlying magnetic field, in response to the release of energy in the core of an active region or (ii) since the PIL is typically a region of energy storage, the contraction of newly-reconnected fields straddling the PIL which also release energy as they shrink (Wang et al., 2016). In the photosphere, the latter would be observed as the horizontal magnetic field, $\boldsymbol{B}_{\mathrm{h}}$, or alternatively the angle of inclination between the field and the local vertical, increasing near the PIL.

Observational studies have provided evidence supporting such changes in the magnetic field configuration near the PIL during flares. Such changes have been detected previously. Li et al. (2009) analysed the X3.4 flare of 2006 December 13 and found that, near the neutral line the magnetic field became more horizontal, with the angle between the field and the local horizontal plane decreasing by $\sim 5^{\circ}$ (while the peripheral penumbral fields became more vertical by $\sim 3^{\circ}$). Wang et al. (2012) reported a rapid and irreversible increase of the horizontal field, $\boldsymbol{B}_{\mathrm{h}}$, during the X2.2 flare on 2011 February 15. Wang et al., 2018 found a rapid $\sim$150–220 G enhancement in $\boldsymbol{B}_{\mathrm{h}}$ in the 2015 June 22 M6.5 flare near the PIL, accompanied by strong shear flows.

More recently, Liu et al. (2022) demonstrated that increases in $\boldsymbol{B}_{\mathrm{h}}$ around the PIL are common. Note, though the usual interpretation of this behaviour is as a result of implosion of the type described in (ii) above, Kleint (2016) interpreted the $\boldsymbol{B}_{\mathrm{h}}$ enhancement detected in the chromospheric magnetic field in one event as a consequence of magnetic untwisting, a more general relaxation of the coronal magnetic system rather than the downward contraction predicted by the coronal implosion model.

1.4 Open Questions: Detection, Timing, and Spatial coincidence

Questions remain regarding the detection and characterisation of magnetic field changes. Many studies have focused on abrupt step-like transitions identified through step-function fitting of magnetogram time series. While this approach has been successful in identifying rapid and permanent field changes, it may not capture the full range of magnetic field evolution that occurs during flares. More gradual or complex changes in the magnetic field may also carry important physical information about the response of the photosphere to coronal magnetic restructuring.

Despite significant progress in understanding photospheric magnetic field changes associated with solar flares, several important questions remain unresolved. One key open question concerns the timing of photospheric magnetic field changes relative to flare emission coming from the chromosphere (UV) or corona (SXR). Some studies have reported that magnetic field changes occur nearly simultaneously with chromospheric flare signatures, while others suggest that the onset of the field change may lag or even precede indicators of the hard X-ray emission. These differences raise important questions about whether photospheric magnetic field changes represent an immediate response to coronal reconnection or whether there are other factors.

Another important issue is the spatial coincidence between flare emission and magnetic field evolution. Flare ribbons mark the chromospheric footpoints of newly reconnected magnetic field lines, and several studies have shown some spatial coincidence between flare ribbons and locations of strong magnetic field changes. However, the degree to which the evolution of flare ribbons traces the locations and timing of magnetic field restructuring remains an active area of investigation, particularly when examining the detailed spatial behaviour of the magnetic field.

Addressing these questions requires careful examination of both the temporal and spatial relationships between flare emission and magnetic field evolution. In particular, combining observations of flare ribbons, photospheric magnetic fields, and indicators of coronal energy release provides a powerful framework for investigating the coupling between different layers of the solar atmosphere during flares.

1.5 Objectives of This Thesis

This thesis aims to investigate the evolution of the photospheric magnetic field during solar flare activity. The specific objectives are as follows.

1. Investigate the temporal and spatial relationship between flare UV emission and line-of-sight magnetic field changes in the photosphere, including both step-like and more gradual magnetic field variations (Chapter 3).
2. Study the development of step-like horizontal magnetic field changes around the polarity inversion line (PIL) and their temporal and the spatial relationship with the onset of flare ribbon emission (Chapter 4).
3. Examine the temporal and spatial relationship between photospheric horizontal magnetic field changes and coronal energy released during solar flares (Chapter 5).

1.6 Thesis Structure

This thesis is organised as follows. Chapter 2 describes the instrumentation, data sources, and machine learning methods used in this work. Chapter 3 investigates the relationship between solar flare ribbons and magnetic field changes in the solar photosphere. Chapter 4 examines the systematic time evolution of the horizontal magnetic field around the polarity inversion line during 35 flares. Chapter 5 explores the temporal relationship between photospheric magnetic field changes and coronal energy release. Finally, Chapter 6 summarises the main findings of this thesis and discusses their implications.

Chapter 2

Instrumentation and Methods

This chapter presents the instruments and methods used in this thesis. The primary data sets were derived from the Solar Dynamics Observatory (SDO), specifically from HMI and AIA, which provide magnetic field measurements and ultraviolet imaging data, respectively. In addition, GOES soft X-ray flux data was used. A detailed overview of the capabilities and data products of these instruments, as well as their relevance to the analysis conducted in this thesis, is provided in this chapter. Furthermore, this chapter also introduces the data analysis techniques applied in this work, which is K-Shape clustering, a machine learning time-series clustering method.

2.1 Helioseismic and Magnetic Imager (HMI)

The Helioseismic and Magnetic Imager (HMI), aboard SDO and positioned at the Sun-Earth L1 Lagrange point, is designed to study the origin of solar variability by characterising the Sun's interior structure and magnetic activity. Its primary scientific objectives include probing convection-zone dynamics, investigating the solar dynamo, and measuring the evolution of photospheric magnetic fields through continuous observations of solar oscillations and polarized spectral-line radiation (Scherrer et al., 2012).

Structurally, HMI comprises a refracting telescope with a 14 cm aperture, a polarization selector, an image stabilization system, a narrow-band tunable filter, and dual 4096×4096 pixel CCD cameras. One camera captures Doppler velocity and continuum intensity data every 45 s, while the other obtains vector magnetic field information derived from multiple polarised filtergrams on a 720 s cadence. These observations facilitate the generation of high-cadence Dopplergram, continuum, line-of-sight magnetogram, and vector magnetogram data products.

2.1.1 Line-of-Sight Magnetograms

The line-of-sight (LoS) magnetic field provides a measure of the component of the photospheric magnetic field aligned with the observer's viewing direction. LoS magnetograms are primarily obtained from the `hmi.M_45s` data series, which provides full-disk line-of-sight magnetic field measurements at a 45-second cadence (Hoeksema et al., 2014). These magnetograms are derived from sequences of filtergrams recorded by HMI's Doppler camera, which samples the Fe I 6173.3 Å spectral line in left- and right-circular polarisation states.

The magnetic field is obtained via the Zeeman effect, where spectral lines split into polarised components in the presence of a magnetic field. Line-of-sight fields produce circularly polarised components whose wavelength separation is proportional to the field strength, while transverse fields generate linearly polarised components used in vector measurements. The HMI instrument samples multiple polarisation states and wavelengths to reconstruct the full Stokes vector and derive the photospheric magnetic field (Scherrer et al., 2012; Hoeksema et al., 2014).

The LoS magnetic field is computed using the "MDI-like" algorithm, which estimates Doppler shifts and Zeeman-induced wavelength separations from the circularly polarised filtergrams (Couvidat et al., 2012). This approach enables rapid production of magnetic maps while preserving sufficient sensitivity for the active region analysis. The high temporal resolution of the `hmi.M_45s` product makes it particularly valuable for analysing rapidly evolving flare intervals. In Chapter 3, these data are used to characterise the magnetic configuration of solar flares.

2.1.2 Vector Magnetograms

In this thesis, vector magnetic field measurements are obtained from the `hmi.B_135s` data series Sun et al. (2017), which is derived from the HMI Vector camera operating on a 135-second cadence. These observations contain the full Stokes *I, Q, U, V* profiles sampled at six wavelength positions across the Fe I 6173 Å line, from which the vector magnetic field is inferred using the Very Fast Inversion of the Stokes Vector (VFISV) Milne–Eddington inversion code (Borrero et al., 2011), followed by a disambiguation procedure to resolve the 180° ambiguity in the azimuthal direction of the transverse field (Metcalf et al., 2006). The `hmi.B_135s` series provides higher-cadence vector magnetic field information compared to the standard 720-second products, making it well suited for timing analysis of rapid magnetic evolution. These data are derived from Stokes profile inversions and provide the magnetic field in terms of strength, inclination, and azimuth, which are subsequently transformed into heliographic components after disambiguation. The magnetic field vector is decomposed into the radial component B_r, approximately normal to the solar surface, and the horizontal components B_θ and B_ϕ, which lie tangential to the surface.

In contrast to line-of-sight measurements, which represent the projection of both radial and horizontal field components along the observer's direction, vector magnetograms allow these contributions to be explicitly separated (Sun et al., 2017). These representations are complementary: the line-of-sight field captures projected magnetic variations, while the

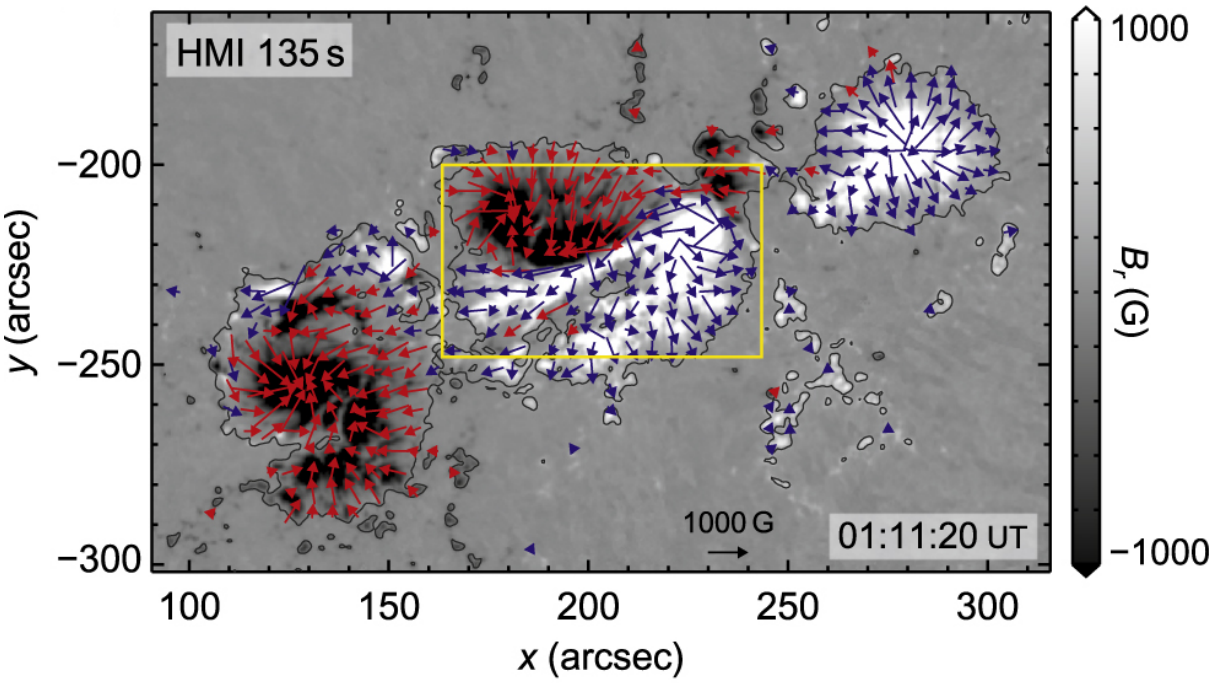

Figure 2.1: Example comparison of vector magnetic field components from Sun et al. (2017). The background image shows the radial field B_r, while arrows indicate the horizontal field B_h. This illustrates how vector magnetograms separate the magnetic field into its components, in contrast to line-of-sight measurements which provide only the projected field.

vector components provide access to the full magnetic field geometry. An example of this comparison is shown in Figure 2.1, adapted from Sun et al. (2017), where the radial field (B_r) and horizontal field (B_h) are displayed for the same active region. Near disk centre, the line-of-sight field closely resembles B_r, while the horizontal field highlights transverse structures, particularly along the polarity inversion line, that are not directly visible in LoS measurements.

2.2 Atmospheric Imaging Assembly (AIA)

AIA on board SDO provides full-disk ultraviolet and extreme-ultraviolet observations with 1.5 arcsec spatial resolution and a nominal 12-second cadence (Lemen et al., 2012). AIA consists of four normal-incidence telescopes that image the solar atmosphere in ten EUV and UV channels spanning temperatures from the upper photosphere to the flaring corona. In this thesis, we particularly used the 1600 Å channel, which is suited for identifying flare ribbons because it responds strongly to impulsive heating in the lower atmosphere, producing sharp, localised brightening that traces newly reconnected magnetic field lines. Accordingly, AIA 1600 Å images are used throughout this work to detect and track the spatiotemporal evolution of flare ribbons. Although hard X-ray (HXR) emission provides a more direct tracer of the timing of peak non-thermal energy deposition, AIA 1600 Å observations offer high spatial resolution and continuous full-disk coverage, making them particularly well suited for studying the spatial and temporal evolution of flare ribbons across large flare samples.

2.3 GOES Soft X-ray Observations

GOES series provides continuous monitoring of the Sun's soft X-ray emission through the X-ray Sensor. The XRS measures broadband flux in two channels, the long-wavelength 1–8 Å band and the short-wavelength 0.5–4 Å band, using ion-chamber detectors. These measurements have been available at high temporal cadence since the mid-1970s and form the basis for the operational classification of solar flares (C-, M-, and X-class events) (Garcia, 1994). The classification scheme is summarised in Table 1.1 (Chapter 1). In this thesis, GOES 1–8 Å soft X-ray flux data are used primarily to determine the timing and magnitude of solar flares associated with the studied events.

In addition, the GOES soft X-ray derivative is used as a coronal energy release proxy. This is motivated by the Neupert effect, which relates the time-integrated non-thermal energy input during a flare to the observed thermal soft X-ray emission. In this framework, accelerated electrons deposit energy in the lower atmosphere, leading to chromosphere heating and evaporation, which fills coronal loops with hot plasma. As a result, the soft X-ray flux represents the accumulated thermal energy, while its time derivative approximates the instantaneous energy deposition rate (Neupert, 1968; Dennis and Zarro, 1993; Veronig et al., 2002a). Therefore, the GOES soft X-ray derivative is used as a proxy for energy release in Chapter 5.

2.4 K-Shape Time-Series Clustering

Traditional analyses of flare-related magnetic field changes have often relied on fitting step-like functions to individual pixel time series (e.g. Sudol and Harvey, 2005), which are effective for identifying abrupt changes. However, this approach assumes a specific functional form and treats each pixel independently, limiting its ability to capture more complex temporal behaviours and coherent patterns across an active region. To address this, a machine learning approach was adopted, allowing a more data-driven analysis where time-series clustering identifies groups of pixels with similar temporal evolution without imposing a predefined model.

In this thesis, we used the k-Shape clustering algorithm implemented in the *tslearn* Python package (Tavenard et al., 2020). K-Shape is specifically designed for clustering time series based on the similarity of their temporal shapes rather than their absolute amplitudes (Paparrizos and Gravano, 2015). The algorithm relies on a shape-based distance (SBD) measure derived from normalised cross-correlation, which allows it to compare the overall

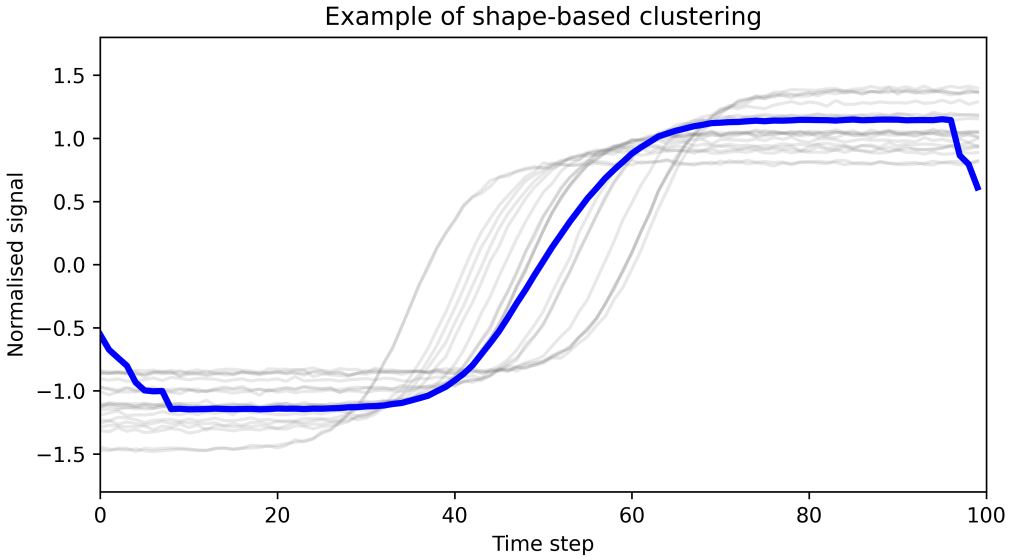

Figure 2.2: Schematic example of shape-based clustering for normalised step-like time series. The grey curves represent individual time series with similar temporal evolution but different transition times, while the blue curve shows the corresponding cluster centroid.

morphology of time series while remaining sensitive to small temporal shifts. This property makes the method suitable for solar flare studies, where magnetic field variations may exhibit similar temporal evolution but occur with different magnitudes and with timing offsets.

A schematic example of the shape-based clustering approach is shown in Figure 2.2. The grey curves represent normalised time series with similar step-like temporal evolution but slightly different transition times, while the blue curve represents the cluster centroid. This illustrates how k-Shape groups time series according to their overall temporal morphology, rather than requiring identical timing or amplitude.

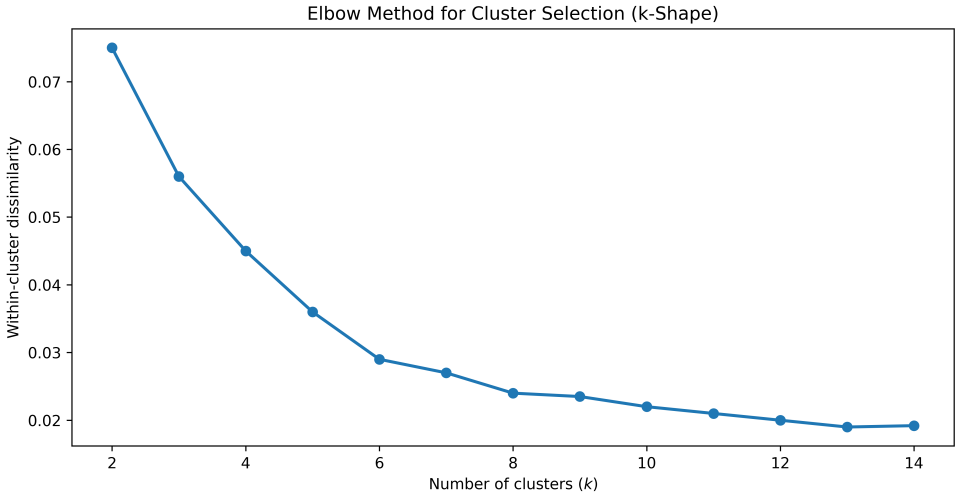

Figure 2.3: Example of the Elbow method used to estimate the optimal number of clusters for k-Shape clustering. The within-cluster dissimilarity decreases as the number of clusters increases, with the elbow indicating the point beyond which additional clusters produce only a marginal reduction in dissimilarity.

Before clustering, the optimal number of clusters was estimated using the Elbow method, by evaluating the within-cluster dissimilarity (based on the shape-based distance) as a function of cluster number. Increasing the number of clusters generally reduces the within-cluster dissimilarity, since the time series are partitioned into progressively more homogeneous groups. The "elbow" corresponds to the point beyond which adding additional clusters produces only a marginal reduction in dissimilarity. An example of the Elbow-method analysis used in this work is shown in Figure 2.3.

The k-Shape algorithm then iteratively groups time series by minimising the distance between each time series and its assigned cluster centroid. At each iteration, cluster memberships are updated based on shape similarity, and the centroids are recomputed to represent the characteristic temporal pattern of each cluster, until convergence is reached (Paparrizos and Gravano, 2015). This clustering approach enables the identification of characteristic patterns in the magnetic field evolution and provides a systematic way to distinguish different types of magnetic field changes during solar flares.

Chapter 3

The Relationship Between Solar Flare Ribbons and LoS Magnetic Field Changes

The work presented in this chapter was published in Alanazi and Fletcher (2025). The analysis, data processing, and interpretation were carried out by the author, with guidance and discussion of the results and manuscript revision provided by the co-author.

3.1 Introduction

The changing magnetic field in solar flares has a complex association with the ultraviolet (UV) emission of flare ribbons. These ribbons are visual markers indicating the chromospheric endpoints of the magnetic field undergoing coronal reconnection, a process thought to be the driver of flares. The relationship between these field changes and ribbons is not entirely clear. These studies (e.g. Sudol and Harvey, 2005; Johnstone et al., 2012; Burtseva et al., 2015; Sun et al., 2017; Yadav and Kazachenko, 2022), as well as the survey published by Kazachenko et al. (2022a), suggest that the temporal and spatial relationship between variations in the magnetic field during a solar flare and chromospheric emissions coming from the flare ribbons is complex and varied. In this work, we aim to investigate spatially-resolved behaviour exclusively over the flare ribbon area, in comparison to others who look at whole active regions or, at the other extreme, single pixels. Whereas previous work, such as Sudol and Harvey (2005), focused on step-like changes in the magnetic field due to their strong temporal and spatial correlation with flare emissions, Castellanos Durán et al. (2018) visually identified 12 different forms of the variation of the line-of-sight (LoS) magnetic field, $B_{\mathrm{LoS}}(t)$ and emphasised the need to examine magnetic field behaviour during flares beyond just step-like variations. We will therefore examine all types of variations in the LoS magnetic field inside the ribbon area and their temporal and spatial correlation with UV emissions, using high-cadence (45 s) LoS magnetograms obtained from HMI/SDO. This approach allows us to build on past studies by considering a wider variety of field changes, which introduces new complexity in understanding the magnetic field dynamics during flares. Lastly, rather than investigate the relationship between the start times of field changes and ribbon emissions, we look at the temporal relationship between the maximum rate of change of the photospheric LoS field and the peak of the UV emission. We made this choice in part because the start

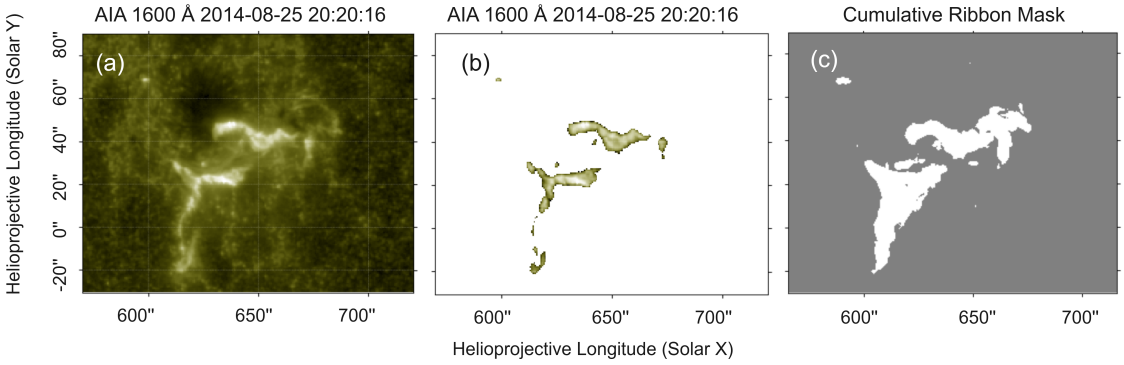

Figure 3.1: Example of the cumulative ribbons identifying processing of the AR NOAA 12146 flare class M3.9 on August 25, 2014, at 20:20:00 UT. (a) displays the original AIA 1600 Å cutout map of the active region, and (b) displays the same map following the flare ribbon identification procedure using the threshold method. (c) displays a binary map that only displays the cumulative ribbons' area over the duration of interest.

time of an event is usually defined when an increasing signal reaches a particular multiple of a pre-event background, and therefore depends on the noise floor of an instrument (or indeed of a particular observation), but also because the time of maximum rate-of-change of the field should be related to the time of the most rapid magnetic reconfiguration.

In this Chapter, in Section 3.2, we show the data sources used in the study, with methodologies for data processing, determining magnetic field changes, and detecting UV emission peaks described in Section 3.3. In Section 3.4, we detail the result of the correlation between UV ribbon emission and field change. Section 3.5 presents a discussion of our findings and we end with conclusions in Section 3.6.

3.2 Data Sources

This study utilises data from two instruments aboard SDO (Pesnell et al., 2012b). Firstly, AIA (Lemen et al., 2012) provides full-disk ultraviolet images with a cadence of 12 s. In particular, the 1600 Å channel is used to identify flare ribbon emission in the chromosphere. Secondly, the HMI instrument (Scherrer et al., 2012). We use the line-of-sight magnetic field measurements from the `hmi.M_45s` data series, which provides magnetograms at a cadence of 45 s (Hoeksema et al., 2014). A detailed description of the SDO instruments and the data products used in this work is provided in Chapter 2. Access to SDO data was enabled through the joint Science Operations Center (JSOC) database website, which provides open access to SDO data. We chose to analyse a subset of the flares selected by Bi et al. (2018), which were chosen based on the following criteria:

1. Flare class limitation: Flares selected for analysis were limited to those classified as M5.0 and below. This limitation was applied to reduce the inclusion of active regions (ARs) known for their high flare productivity, which could lead to image saturation in the AIA 1600 Å wavelength which would lower the accuracy of ribbon location detection.
2. The location of the AR: Active regions selected as the source of flares were required to be situated within 60 degrees of the solar disk centre to minimise potential observational errors as we deal with line-of-sight magnetic fields.

Bi et al. (2018) had a further criterion of 135s-cadence HMI vector data available for at least 2 hours before and after the flare. Though we are not using vector data in this study, selecting from their list means future work can examine vector field changes. Table 3.1 displays six flares which satisfy these criteria.

The flare start, peak and end times are identified using GOES 1 - 8 Å X-ray flux.

Table 3.1: List of the flares.

Number	Flare Class	NOAA Number	GOES Peak time (UT)
1	M1.3	11748	2013/05/16 21:53:00
2	M3.7	11974	2014/02/12 04:25:00
3	M1.5	12127	2014/08/01 18:13:00
4	M3.9	12146	2014/08/25 20:20:00
5	M3.7	12443	2015/11/04 13:52:00
6	M3.9	12449	2015/11/09 13:12:00

3.3 Methods: Using Flare 4 as an Example

3.3.1 Identifying the Flare Ribbons

We first create a mask to isolate the regions in the AIA 1600 Å images representing flare ribbons, utilizing the method of Toriumi et al. (2017). Pixels considered part of the ribbon must have an intensity greater than or equal to 40 times the standard deviation above the mean intensity of the quiet Sun. The quiet Sun intensity was estimated from a selected quiet region on the solar disk and the mean intensity of this region was used as the background level. Thereafter, we created a map sequence of the AIA 1600 Å masked flare ribbons at each timestep for ninety minutes to create a map of the cumulative ribbons. An example of this is shown in Figure 3.1. The active region's original AIA 1600 Å cutout map at a single time in the flare is shown in panel 3.1(a), and panel 3.1(b) shows the same map after the flare ribbon thresholding. A binary map which exclusively shows the cumulative ribbons' area throughout the time of interest is shown in panel 3.1(c).

3.3.2 Reprojection and Co-alignment of AIA and HMI

The ribbons defined in AIA 1600 Å images need to be projected onto the SDO/HMI magnetogram image. We employ the Astropy (Astropy Collaboration et al., 2022) 'reproject' package, with fast interpolation, to transform the data. We decided to reproject the AIA data to the HMI grid instead of vice versa, because interpolation can eliminate small-scale changes in the LoS magnetic field, which are important in this context, and also the fact that the range of the HMI data contains both positive and negative values as mentioned in The SunPy Community et al. (2020). This approach results in coaligned HMI and reprojected AIA images, correcting the pixel size difference between the two instruments.

3.3.3 Magnetic Field Changes

3.3.3.1 Data Generation

For each of the selected flares we obtained 108 full disc, 45-second cadence HMI line-of-sight magnetograms, over 90 minutes. The region of interest around the flare ribbons was cut out and AIA and HMI aligned as described in Section 3.3.2. We divided each cumulative ribbon into boxes of 3×3 pixels. This box size was chosen as a compromise between spatial resolution and noise reduction. An example of flare 4 is illustrated in the upper panel of Figure 3.2. Then, the mean LoS magnetic field value $\overline{B}_{LOS}$ is obtained for each box and a time series of $\overline{B}_{LOS}$ within each box constructed.

For the purpose of identifying the primary trend in the magnetic field time series, we implemented Savitzky-Golay filtering (Savitzky and Golay, 1964), which convolves the signal with a low-degree polynomial fitted through successive groups of points via linear least squares, which reduces noise while preserving the signal trend. This has been used

previously in solar time series data by (e.g. Gontikakis et al., 2020; Hayes et al., 2021). After some experimentation, we decided on a Savitzky-Golay filter using a 3rd-degree polynomial to smooth the data. This polynomial is generated on each time series point t_i by considering its closest points, which range from t_{i-3} to t_{i+3} (Gontikakis et al., 2020). The lower panel of Figure 3.2 shows an example from the box highlighted in yellow in the upper panel. The black solid line indicates the smoothed data of the mean LoS magnetic field values obtained using this technique.

3.3.3.2 Derivatives as Magnetic Field Change Indicators

As shown in Section 3.3.3.3 the variations with time of $\overline{B}_{LOS}$ have a range of behaviours and cannot typically be fitted with the step-like function used by previous authors. So for our timing comparison we have chosen to look at the derivative of the field which has been smoothed using the Savitzky-Golay filter to identify the time when it is changing most rapidly. This is motivated by Gontikakis et al. (2020) who also employed temporal derivatives of Savitzky-Golay filtered flare temperature and emission measure, and by Pesnell (2024) who employed the temporal derivative to analyse the temporal variation of the number of sunspots on the solar cycle.

The derivative of the magnetic field in the flare ribbons is expressed as:

$$\left|\frac{d\overline{B}_{\mathrm{LoS},i}}{dt}\right| = \left|\frac{\overline{B}_{\mathrm{sm},i+1} - \overline{B}_{\mathrm{sm},i}}{\Delta t}\right| \tag{3.1}$$

where $\overline{B}_{\mathrm{sm},i}$ is the value of the smoothed, box-averaged, line-of-sight magnetic field at timestep i. This analysis was performed on each box on the cumulative ribbons region of each flare, and an example is shown in the lower panel of Figure 3.2. The blue curve, which is the derivative of $\overline{B}_{\mathrm{LoS}}$, shows a strong peak when the LoS magnetic field value changes by a significant amount. Note, in this case there is a clear oscillation in B_{LoS}, and the maximum of $d\overline{B}_{\mathrm{LoS}}/dt$ occurs at the rise of the first oscillation. There are still some small fluctuations on the smoothed black curve but overall, the absolute derivative curve displays a sudden and significant spike, indicating a shift in the magnetic field values. So we consider the timing of this peak to be a good indicator of the LoS magnetic field line change.

3.3.3.3 Clustering B_{LoS} Time Series Types

To capture the different temporal variations in the line-of-sight magnetic field, we clustered the time series extracted from each 3×3 box within the cumulative flare ribbons. The clustering was performed using the k-Shape time-series clustering algorithm implemented in the *tslearn* Python package. The optimal number of clusters was selected using the Elbow method. Further details of the k-Shape clustering technique are provided in Section 2.4. This algorithm can effectively manage the variations in scale and temporal shifts, making it ideal for analysing the diverse behaviours of the LoS magnetic field, which show such variations at different locations in the flare ribbons.

For example, as demonstrated in Figure 3.3, the application of the k-Shape algorithm to the data from flare 4 resulted in six different clusters, showcasing the variety of LoS magnetic field behaviours within the flare ribbons. Note, the scaled values shown are with respect to an average, so a changing sign does not mean that the field is changing polarity (as does appear to happen in magnetic transients, e.g Song et al. (2018), due to disturbances in the formation of the 6173.3Å Fe I spectral line used to determine the magnetic field). We find groups showing roughly monotonic changes, but also groups in

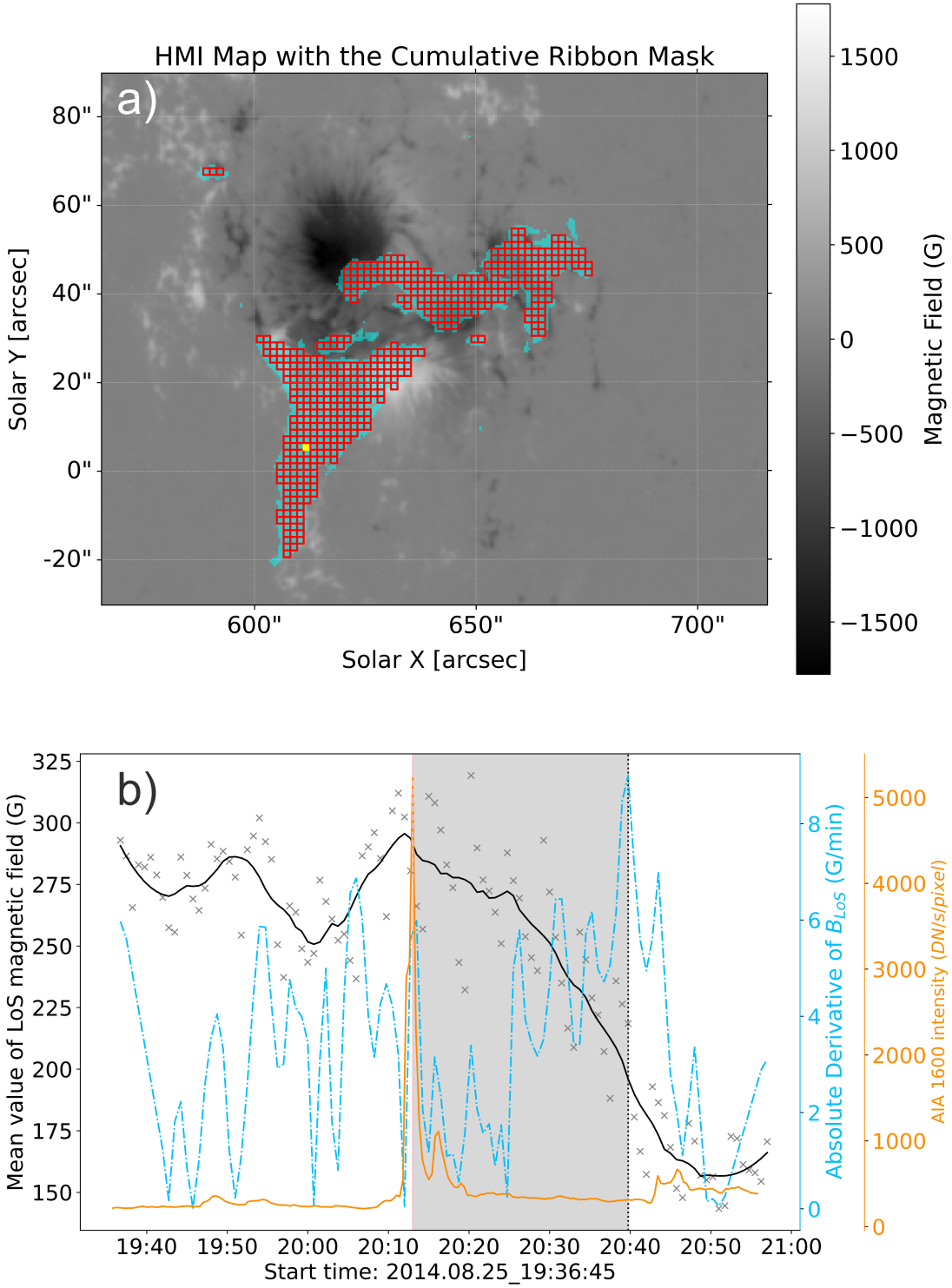

Figure 3.2: The upper panel presents red boxes with dimensions of 3×3 pixels inside the cumulative ribbon areas, while the yellow box is the case studied in detail on the lower panel. The background image is an HMI magnetogram map of the AR NOAA 12146 flare class M3.9. Lower panel: a case study of the yellow box: time series of AIA 1600 Å intensity (orange line) and the temporal variation of the mean LoS magnetic field (grey cross). The smoothed B_{LoS} using the Savitzky-Golay filter is shown in a solid black line, while the dashed blue line shows the absolute derivative of the $\overline{B}_{\mathrm{LoS}}$. The grey region shows the time lag τ which is the time between the AIA 1600 Å peak time (orange vertical line) and the time of the biggest peak time of the $|dB_{\mathrm{LoS}}/dt|$ (black vertical line).

which the field shows one or more oscillations with typical periods ranging from 20 to 40 minutes and amplitudes around 70 G. This variety highlights the complexity of the magnetic field evolution during solar flares. Building on this, we applied this clustering algorithm to data from six flares to explore the full range of LoS magnetic field variations across the flare ribbons, which will be explained in detail in Section 3.4.3.

3.3.4 UV Emission Peak

We identify the emission peak time of the AIA 1600Å lightcurve in each box inside the cumulative flare ribbons in order to examine the relationship between the LoS magnetic field changes and the UV emission. For each flare listed in Table 3.1, we have a datacube consisting of 201 maps that covered 90 minutes. Employing the methodology outlined in section 3.3.1, we mask the areas with cumulative flare ribbons. Next, we generated separate time series for each box inside the cumulative ribbons. We identified the time of peak intensity for each flare ribbon by utilising the SciPy `find_peaks` function. For illustration, Figure 3.2 lower panel displays the AIA 1600 Å intensity time series (orange line) for the yellow box, and the orange vertical dashed line represents the time of the intensity's maximum peak. The time of the peak of the AIA 1600 Å data will be compared to the time of maximum rate of change of the LoS magnetic field to establish their relationship.

3.4 Results

In this section, we examine the relationship between ultraviolet (UV) emissions originating from flare ribbons and variations in the photospheric magnetic field. We compare the time of the maximum rate-of-change in the photospheric magnetic field with the time of maximum UV ribbon emission, in each 3×3 sample box. Since the ribbon emission and

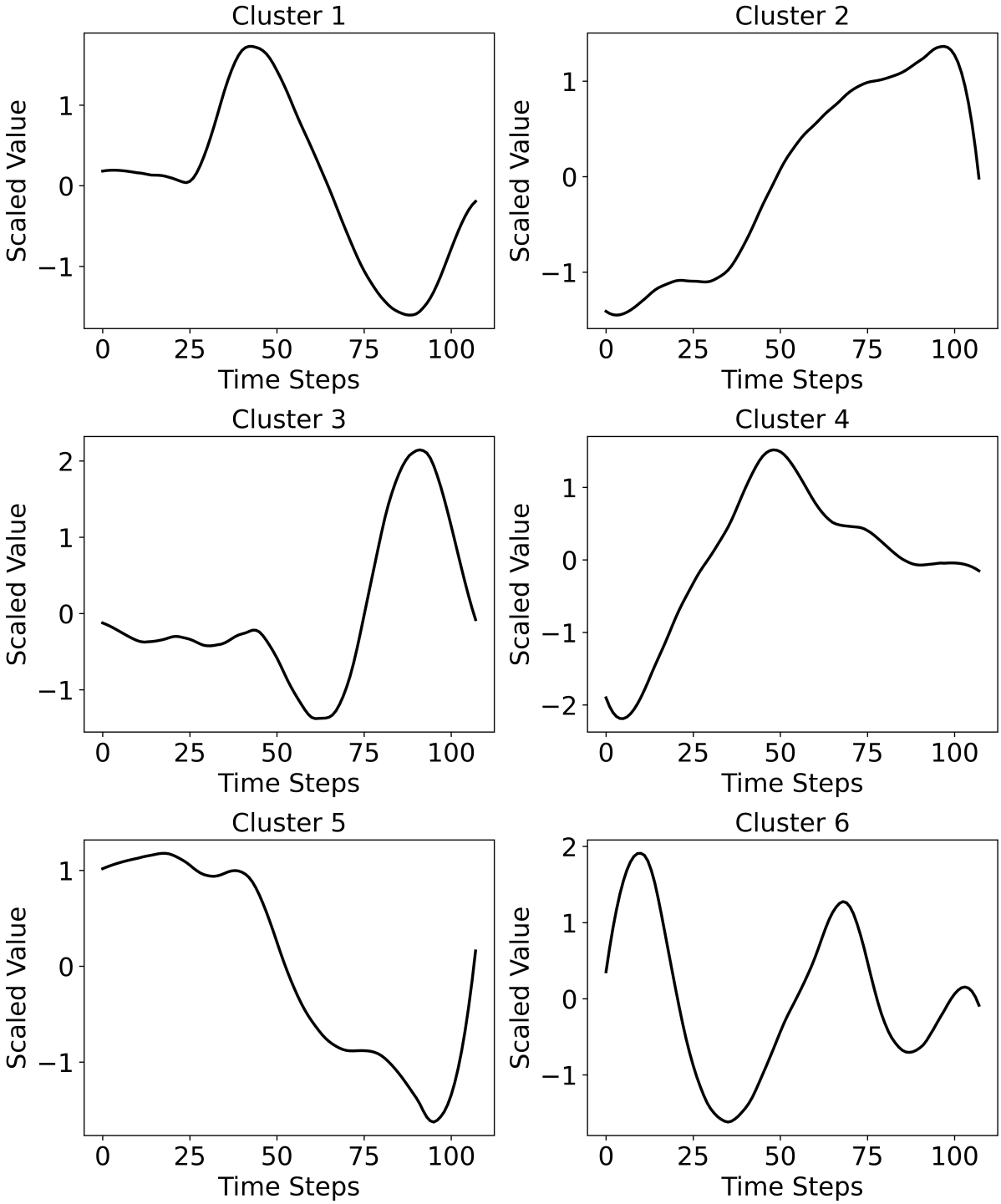

Figure 3.3: k-Shape Clustering of LoS Magnetic Field Variations for Flare 4: M3.9 AR NOAA 12146. It presents six clusters of LoS magnetic field time series, derived using the k-Shape clustering algorithm. Each cluster was smoothed using the Savitzky-Golay filter, representing a unique pattern of magnetic field behaviour across different regions within the cumulative flare ribbons.

the observed magnetic field changes occur at different heights in the solar atmosphere, the time lag between the two phenomena may help understand magnetic field reorganisation and energy transport. Finally, we explore the different types of LoS magnetic field changes identified by machine learning in the ribbons.

3.4.1 Temporal-spatial Correlation between UV Emission and field changes

We define the time delay, τ, as follows:

$$\tau = t_B - t_{UV}, \tag{3.2}$$

where t_B represents the time of highest rate of change in the LoS magnetic field within a 3×3 box, and t_{UV} is the peak time of the AIA 1600 Å intensity. A positive τ (blue in Figure 3.4 indicates that the AIA 1600 Å intensity peaked before the maximum of the magnetic field rate of change.

We calculated τ (in minutes) for each box across the cumulative flare ribbon, and created a colour-coded map (Figure 3.4) that displays the spatial and temporal relationships across the ribbon flare. These maps highlight how different regions of the ribbon correspond to specific time delays.

Table 3.2: Parameters for Selected Flares.

Flare No.	Total Number of boxes	mean $\tau(min)$	$\sigma_\tau(min)$	Number of boxes with +ve τ	Number of boxes with -ve τ
1	356	0.43	24.63	183 (51.40%)	173 (48.60%)
2	905	-2.84	28.21	431 (47.62%)	474 (52.38%)
3	1150	-10.82	29.15	437 (38.00%)	713 (62.00%)
4	504	-4.80	22.06	192 (38.10%)	312 (61.90%)
5	995	-3.57	25.22	409 (41.15%)	585 (58.85%)
6	981	0.37	24.66	520 (53.01%)	461 (46.99%)

We can observe from Table 3.2 that the number of boxes is distributed nearly evenly when divided into positive and negative τ. The colour-coded maps in Figure 3.4 strongly show that red and blue are blended across the cumulative ribbons, though there is also some systematic behavior. For example, there are specific red patches in darker shades, indicating a higher time lag τ in areas with a weak magnetic field in flares 2, 3, 5 and 6. The red color indicates a negative τ, meaning that the field change occurs before the AIA 1600 Å peak, typically by 10 to 20 minutes though longer lags are also present.

The positive lag locations are scattered across the flare ribbons and are generally associated with small magnetic fields. However, a small blue patch is observed in the high magnetic field region near the negative sunspot in Flare 1. Since the average time lag for each flare was calculated in earlier research (e.g. Sudol and Harvey (2005); Johnstone et al. (2012); Yadav and Kazachenko (2022)), we offer the average time lag for each flare in Table 3.2 for comparison purposes. We observed that in 4 out of the 6 flares, the average time lag (τ) was negative (UV peak lags field change). The maximum time lag recorded was 10.82 minutes. A positive time delay is observed in both Flare 1 and Flare 6, with a minimal time difference of $\tau = 0.43$ minutes in Flare 1 and $\tau = 0.37$ minutes in Flare 6. In all events, the standard deviation of the time lag (σ_τ) was 25-50 minutes, indicating substantial variability. Notably, Flare 3 exhibits the largest time lag of $\tau =$ 10.82 minutes. This flare also has the highest number of boxes within the cumulative flare ribbons, indicating the largest affected area, which may contribute to the extended delay.

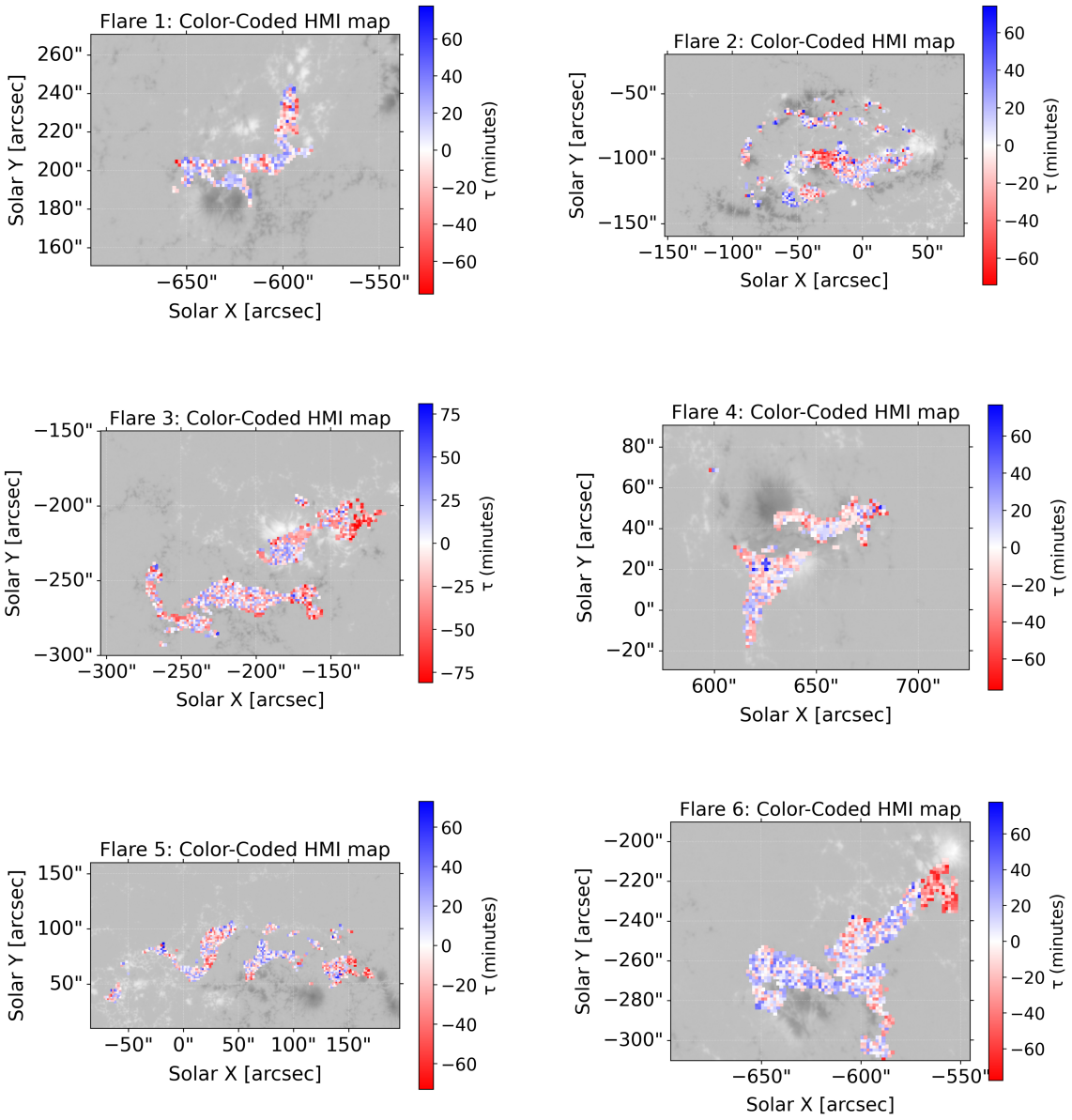

Figure 3.4: HMI maps of 6 selected flares with colour-coded boxes representing the time difference (τ) between the peak times of the AIA 1600 Å and the mid-time of change on the LoS magnetic field. Each box is coloured based on the time difference in minutes, with a colour gradient from blue (positive time differences) to red (negative time differences). The boxes are superimposed on the HMI map with the cumulative ribbons mask applied, highlighting regions of interest. The displayed field of view differs between panels because each flare was cropped to the relevant ribbon region.

3.4.2 Rate of Field Changes

We next examined the spatial distribution of the rate of change in the LoS magnetic field across the cumulative flare ribbon regions as shown in Figure 3.5 expressed in Gauss per minute.

Each box on the map delineates a specific region of interest, with colour intensity reflecting the magnitude of the rate of change. We observe that the rate of change varies between 2 and 25 G/min, which is reasonable for M-class flares, as previous studies have indicated that the rate of change in the longitudinal magnetic field in larger X-class flares can be on the order of tens of gauss per minute (Sudol and Harvey, 2005). There appears to be substantial groups of pixel locations with similar rates of change. By visual inspection of AIA 1600 Å movies, we identify a correlation between the duration of flare ribbon appearance and the rate of magnetic field change. Specifically, regions, where flare ribbons last longer, are characterised by higher rates of change in the LoS magnetic field. This observation suggests that longer-lasting ribbon activity is associated with more significant and rapid magnetic field variations. Supporting this, Yadav and Kazachenko (2022) found a strong correlation between the duration of permanent field changes and GOES flare durations, with field changes ranging from 5 to 17.5 minutes, further confirming the association between long periods of activity and higher rates of magnetic field change.

To investigate how the rates of change are related to the strength of the LoS magnetic field we produced the scatter plots in Figure 3.6. These show the modulus of the maximum rate of change in each 3×3 box, and the corresponding absolute LoS magnetic field. The maximum rate of change was selected to characterise the peak magnetic response within each region, whereas the mean rate of change would smooth the abrupt variations associated with the flare. Though there is a substantial scatter in the data, there is a broad trend of higher rates of change in regions of higher B_{LOS} up to some maximum value, after which there is a downward trend visible in some of the events. We fitted the

Table 3.3: The maximum absolute field rate of change and the corresponding $|B_{\mathrm{LoS}}|$, with associated uncertainties ($\pm\sigma$), from the fits shown in 3.6.

Flare No.	$\lvert dB_{\mathrm{LOS}}/dt\rvert_{\mathrm{max}}$ G min^{-1} (1 dp)	Corresponding $\lvert B_{\mathrm{max}}\rvert$ G (2 sf)
1	8.1 ± 4.4	480 ± 50
2	10.0 ± 4.1	670 ± 60
3	11.1 ± 3.8	760 ± 60
4	8.8 ± 2.8	600 ± 50
5	8.4 ± 2.8	700 ± 50
6	7.8 ± 2.7	550 ± 50

data with a quadratic function $ax^2+bx+c=0$ which effectively captures the non-linear trend in the data. We then used the fits to calculate the values of the maximum rate of change and the B_{LOS} value at which they occur. The fits are shown as the green curve in Figure 3.6 and the maximum value of the rate of change and the mean magnetic field at which this occurs is shown in Table 3.3.

The fitted maximum rate of change is around 7-10 G min^{-1} with an average for the six flares of approximately 8.6 G min^{-1}. Furthermore, it was observed that the highest rates of change occur in regions with magnetic fields ranging from around 480 to 760 G. The relationship between the magnetic field strength and the rate of change of the magnetic field suggests that regions with stronger magnetic fields are more likely to experience rapid and intense magnetic reconfiguration. Thereafter, the slight downward trend may indicate that it is increasingly difficult to perturb the strongest fields.

3.4.3 Types of LoS Magnetic Field Changes in Flare Ribbons

During our investigation, we observed that the LoS magnetic field behaviour takes on various forms within the flare ribbons. To our knowledge this has not been examined in previous literature, which is focused on permanent step-like change. Castellanos Durán et al. (2018) were the first to indicate that they observed a variety of field changes besides

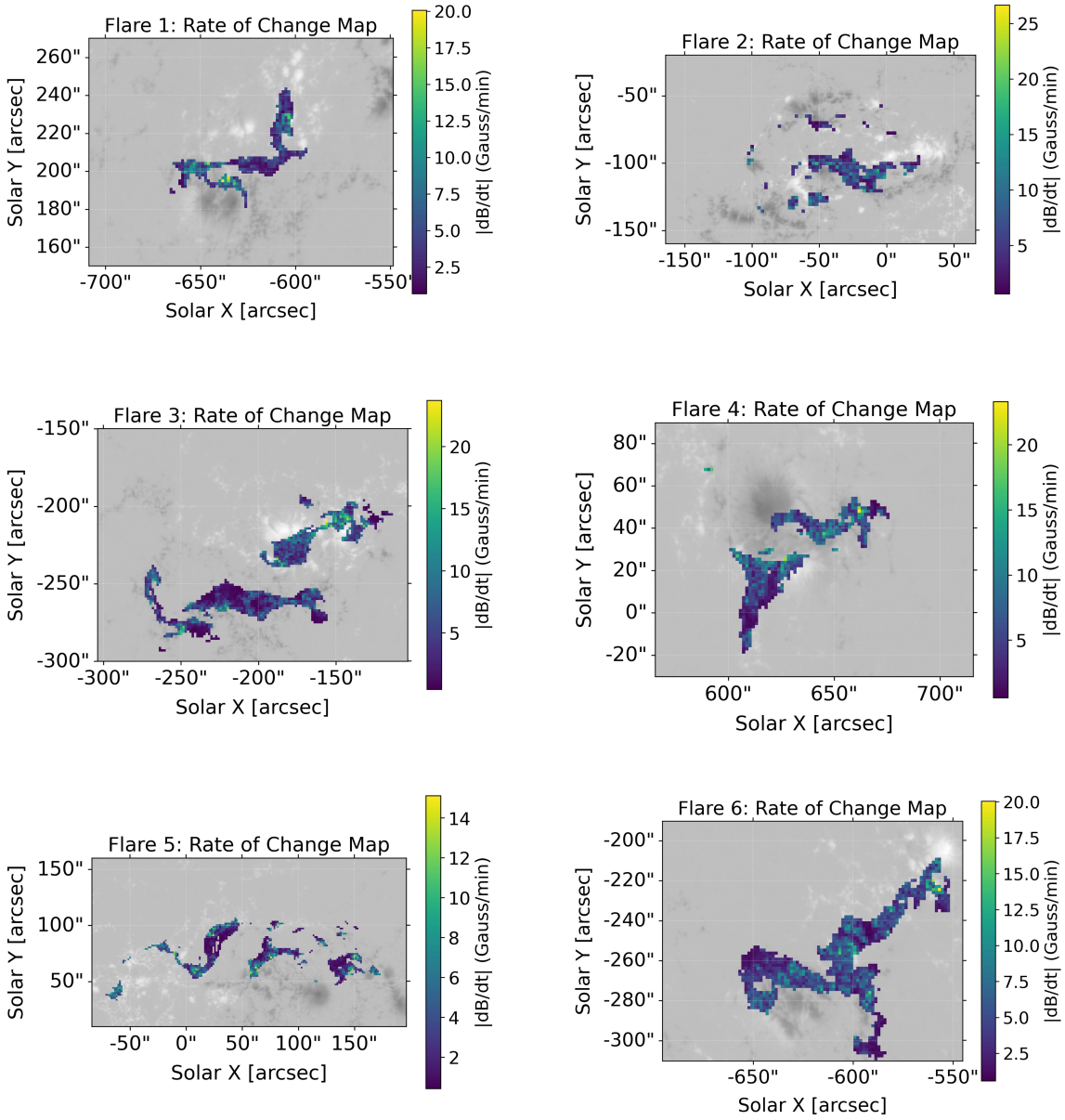

Figure 3.5: Spatial distribution of the rate of change of the LoS magnetic field (in Gauss per minute) across the cumulative ribbon area on the 6 selected flares. Each box represents a region of interest on the map, and the colour within the boxes indicates the magnitude of the rate of change. The colour map ranges from dark blue to yellow, with darker colours indicating lower amplitudes and brighter colours representing higher amplitudes. The colour bar provides a scale for interpreting the amplitude values.

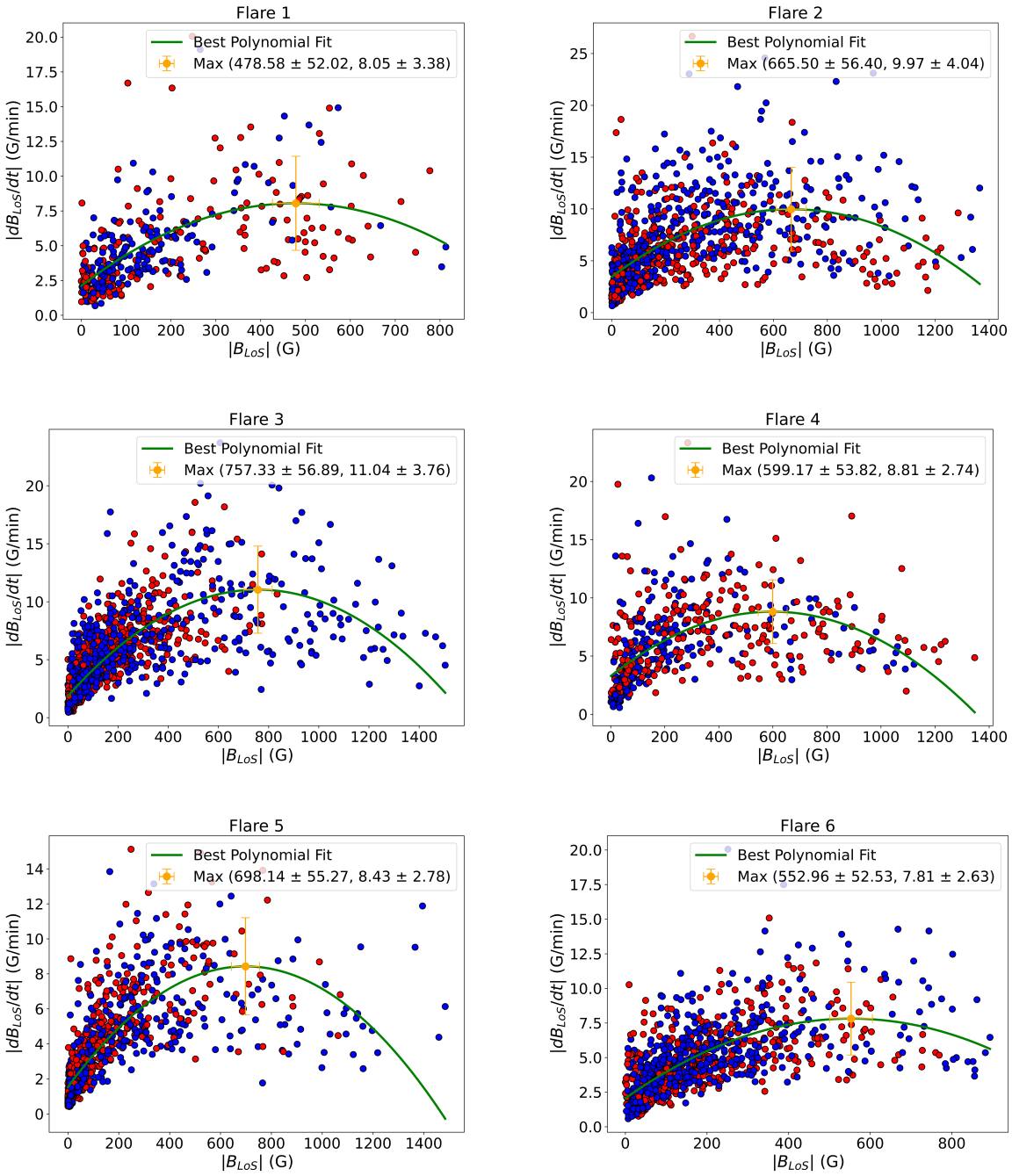

Figure 3.6: Scatter plots of the six selected flares showing the relationship between the absolute magnetic field ($|B_{\mathrm{LoS}}|$) and the rate of change of the magnetic field ($|dB/dt|$). The plotted values correspond to the time of the maximum magnetic field rate of change within each data box. Each point represents a data box within the flare ribbons, colour-coded based on the sign of the magnetic field: blue for positive and red for negative magnetic fields. The green line represents the quadratic fit applied to the data, which models the non-linear relationship between $|B_{\mathrm{LoS}}|$ and $|dB/dt|$. The orange marker highlights the maximum rate of change ($|dB/dt|$) determined from the fit, with associated error bars indicating the uncertainty in the measurement.

the step-like shape, but they did not include them in their analysis. Furthermore, in their conclusion, Yadav and Kazachenko (2022) emphasise the importance of considering all types of B_{LoS}. In consequence, the current study is the first to include all forms of changes in the LoS magnetic field on flare ribbons.

We applied the clustering algorithm described in Section 3.3.3.3 to explore the full range of LoS magnetic field variations across the flare ribbons. Figure 3.7 and 3.8 provide an analysis of the time series behaviour of the magnetic field across these regions. The left panel for each flare shows the HMI map, with each 3×3 pixels box colour-coded according to its cluster assignment. This highlights regions on the flare that exhibit similar magnetic field variations. The right panel displays the average time series for each cluster, smoothed using a Savitzky-Golay filter. From this analysis, we observed that the average number of different clusters characterizing the LoS magnetic field variations in the cumulative flare ribbon areas is 6 clusters.

The images reveal a consistent pattern in which regions with stronger magnetic fields exhibit similar changes, manifesting as patches of boxes in the same colour (note, due to the different clustering, the colours are not completely consistent across flares). Flares 3 and 4 provide a good example of this. This observation allows us to generalise that stronger magnetic fields tend to show more structured behaviour. However, overall the spatial distribution of clusters within the cumulative flare ribbon areas lacks a clear pattern. In particular, weaker magnetic fields are characterised by inhomogeneity in the types of field change found. This suggests that regions with similar LoS magnetic field variations do not conform to a predictable spatial arrangement. The absence of a discernible spatial pattern implies that the clustering of magnetic field behaviours is not significantly influenced by straightforward factors such as proximity to the polarity inversion line (PIL) or specific magnetic field strengths. This lack of a clear spatial pattern underscores the complex changes of magnetic fields in active regions, suggesting that they are not solely related

to spatial arrangements. These observations align with the findings of Jing et al. (2007), who noted inhomogeneity in magnetic field quantities along flare ribbons, indicating that coronal magnetic reconnection and energy release rates also display spatial variability rather than a uniform distribution.

3.4.3.1 Exploring Monotonic LoS Magnetic Field Changes

In Section 3.4.1, we presented maps of the time lags obtained from analyzing the field changes. However, the clustering results show some oscillations in the magnetic field behaviour (see Figure 3.6). In such cases, it remains unclear whether these changes are flare-related. Using the clustering technique, we manage to split the clusters into two categories: (a) monotonic magnetic change, which includes increases, decreases, and step-like variations and (b) oscillating magnetic changes. To address this, we examined boxes outside the ribbon regions, which revealed the same type of oscillatory behaviours observed within the cumulative flare ribbon regions, from which we conclude that this type of variation in many cases reflects ongoing photospheric processes, such as convective motions, flux emergence, or magnetic evolution unrelated to the flare itself. Additionally, Figure 3.4 shows that the time lags in some boxes are relatively long compared to previous studies, where time lags ranged from several minutes to 20 minutes (e.g Sudol and Harvey, 2005; Johnstone et al., 2012; Yadav and Kazachenko, 2022). This prompted us to establish a new criterion for selecting boxes within the cumulative flare ribbons. Specifically, the boxes should:

1. Belong to the monotonic clusters, and
2. Have time lags restricted to a range of ± 20 minutes.

This criterion was intended to provide a clearer representation of the spatial distribution of the time lag (τ) which may be more closely associated with flares, as shown in Figure 3.9. However, even after isolating these monotonic clusters, the spatial distribution of time lags did not exhibit a noticeable pattern. Nonetheless, we found a smaller mean time lag for

each flare compared to the results derived from all clusters, indicating a tighter temporal relationship between changes in the magnetic field and UV emission. For example, the mean time lags for flares 1 through 6 are -1.00, 2.68, 2.25, 0.89, -2.59, and 1.76 minutes, respectively, smaller than the values in Table 3.2 (which include all clusters). This is likely a result of imposing the ±20 minute time range, and reducing the effect of outliers.

Table 3.4 presents the fraction of boxes that exhibit monotonic changes in B_{LoS} for each flare, as well as the fraction of those with monotonic changes within a time lag of ±20 minutes. The data show that for some flares, a significant proportion of boxes exhibit monotonic changes in B_{LoS}, with flare 1 and flare 6 exhibiting the highest fractions at 0.45. However, when the time lag restriction of ±20 minutes is applied, the fraction of boxes with monotonic changes in B_{LoS} decreases, with Flares 2, 3, and 5 showing significantly smaller fractions (0.05, 0.05, and 0.03, respectively). This decrease underscores the rarity of monotonic changes in the magnetic field (e.g., stepwise) within the flare ribbon areas, as noted by Petrie and Sudol (2010). A key distinction is that stepwise changes, characterised by abrupt change that stand out from background variations, can be considered a specific type of monotonic change when the step and background trends align. However, not all monotonic changes are stepwise, and not all stepwise changes are monotonic.

Finally, to explore whether the maximum rate of change values are affected by applying these two conditions, Figure 3.10 presents a scatter plot of the absolute magnetic field ($|B_{\mathrm{LoS}}|$) and the rate of change of the magnetic field ($|dB_{\mathrm{LoS}}/dt|$) for the six selected flares. Each point in the scatter plot represents a data box that meets the conditions of monotonic changes and a time lag within ±20 minutes. The plot reveals similar values of the maximum rate of change, though with less structure and more scatter, compared to the values presented in Figure 3.6 (which includes all clusters).

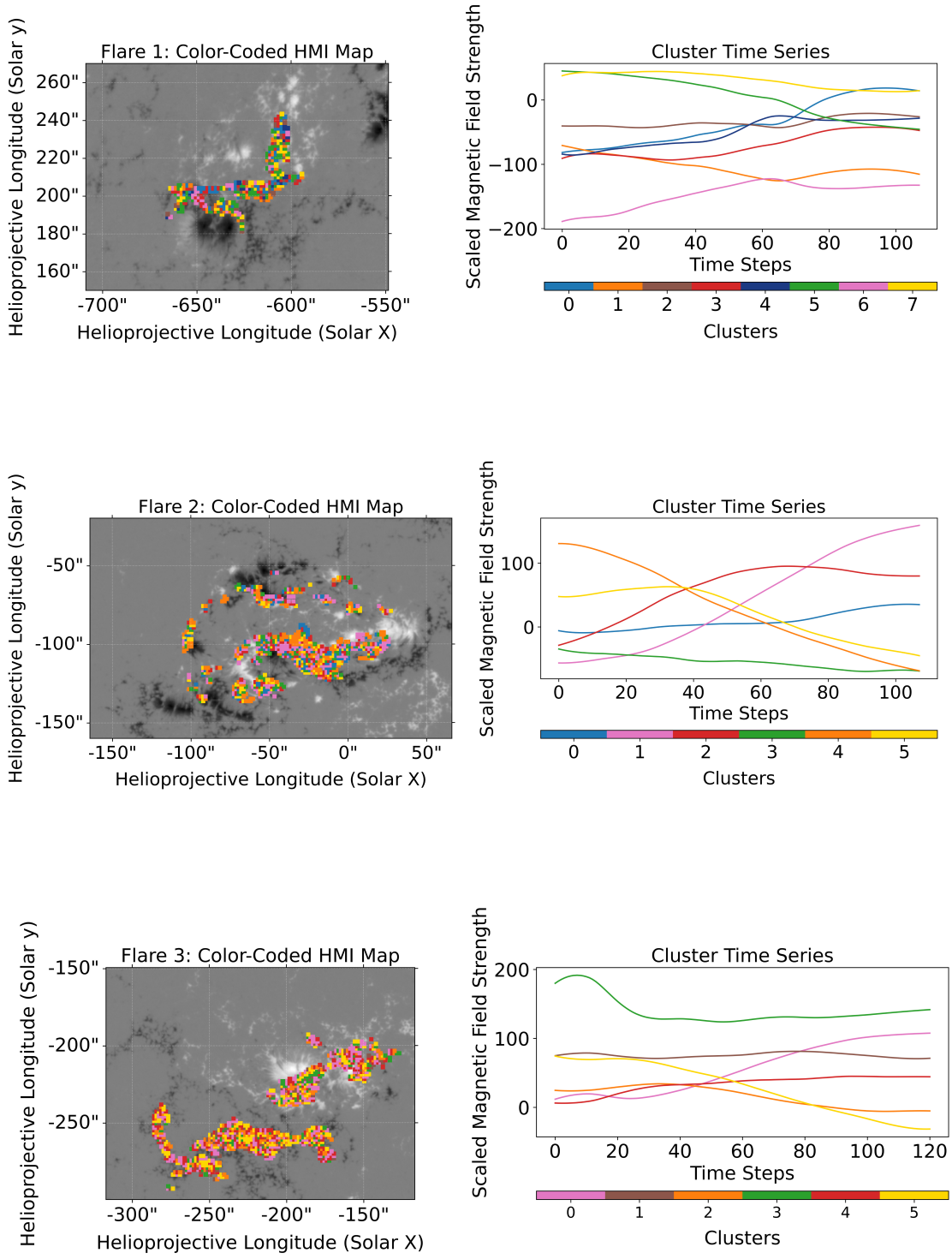

Figure 3.7: A comparison of the solar HMI map and the corresponding time-series behaviour of magnetic field regions, clustered using k-Shape clustering for flares 1–3. The left panel displays the HMI map, where each box (representing 3x3 pixels) is colour-coded according to its cluster assignment, highlighting regions of the Sun with similar temporal magnetic field variations. The right panel presents the average time series for each cluster, with the curves smoothed using a Savitzky-Golay filter. The legend identifies the clusters by colour.

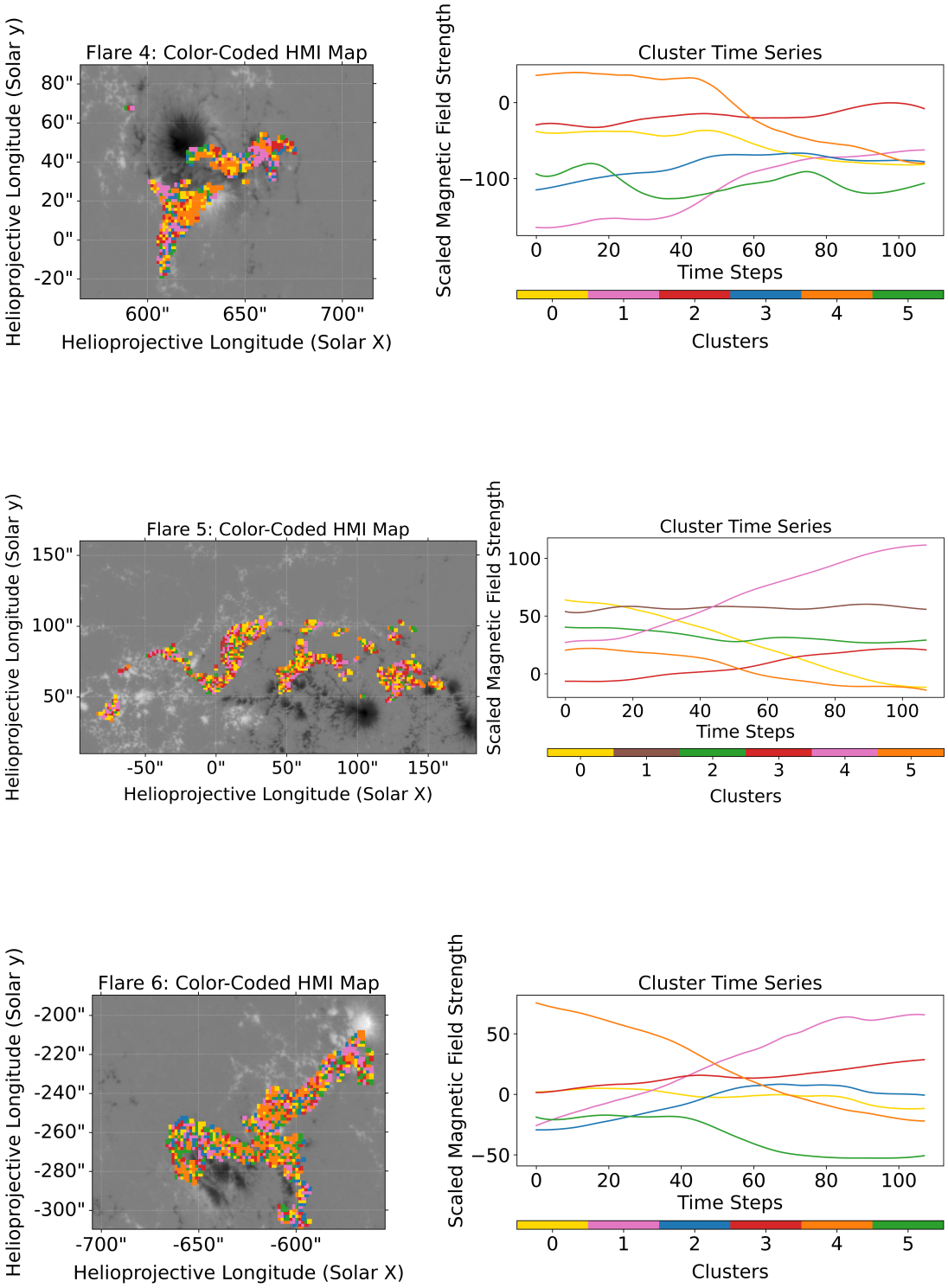

Figure 3.8: Same as Fig. 3.7, but for flares 4–6.

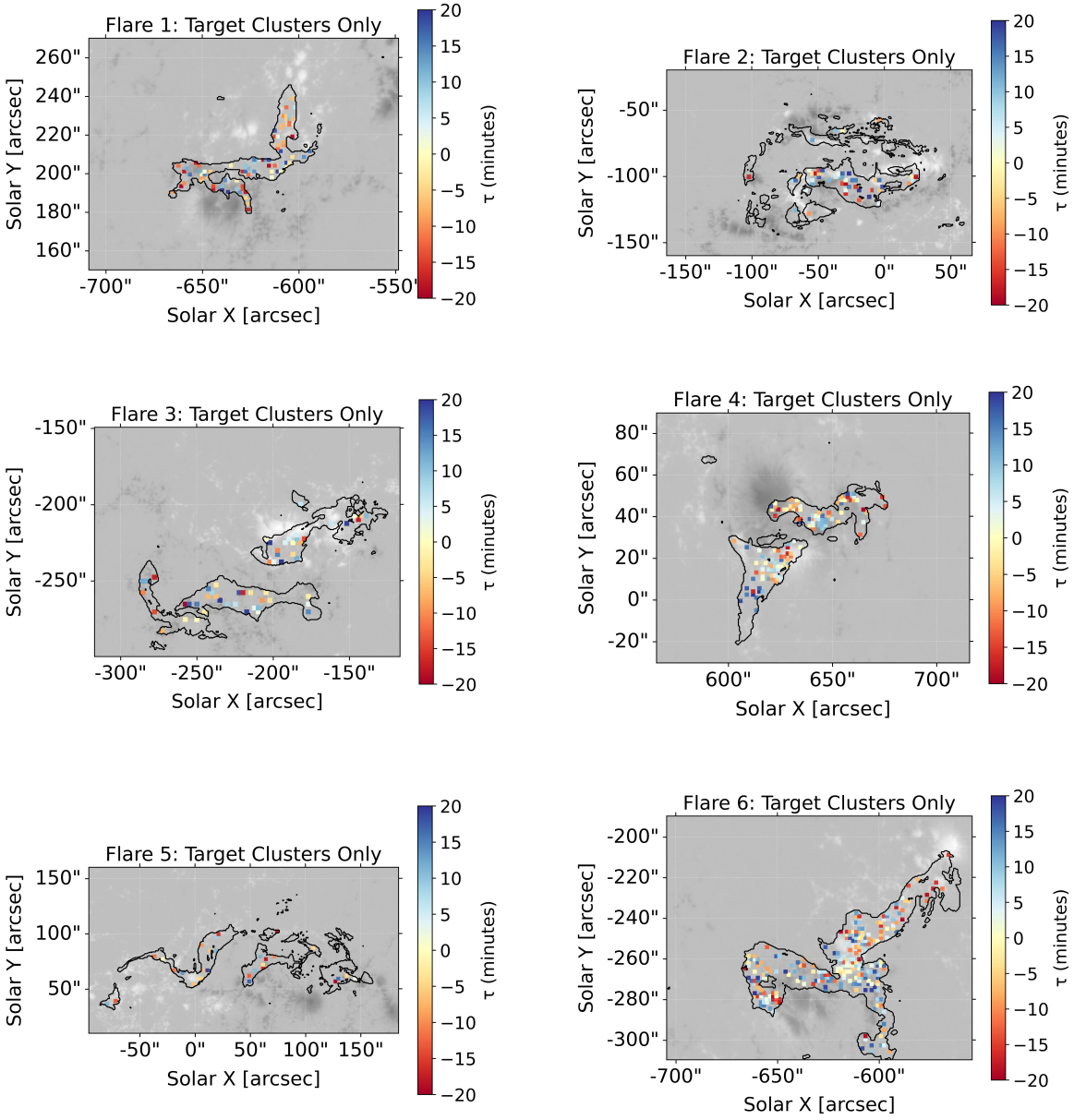

Figure 3.9: Colour-coded map of time lags (τ) for monotonic target cluster regions during the evolution of six solar flares. The map highlights regions within selected monotonic clusters, with colours representing the time lag (in minutes) between the peak times of AIA 1600 Å and the mid-change time of the B_{LoS} field. This time lag is limited to a range of ± 20 minutes. Positive time lags (blue) indicate that the AIA 1600 Å peaks precede the B_{LoS} mid-change, while negative time lags (red) indicate the opposite.

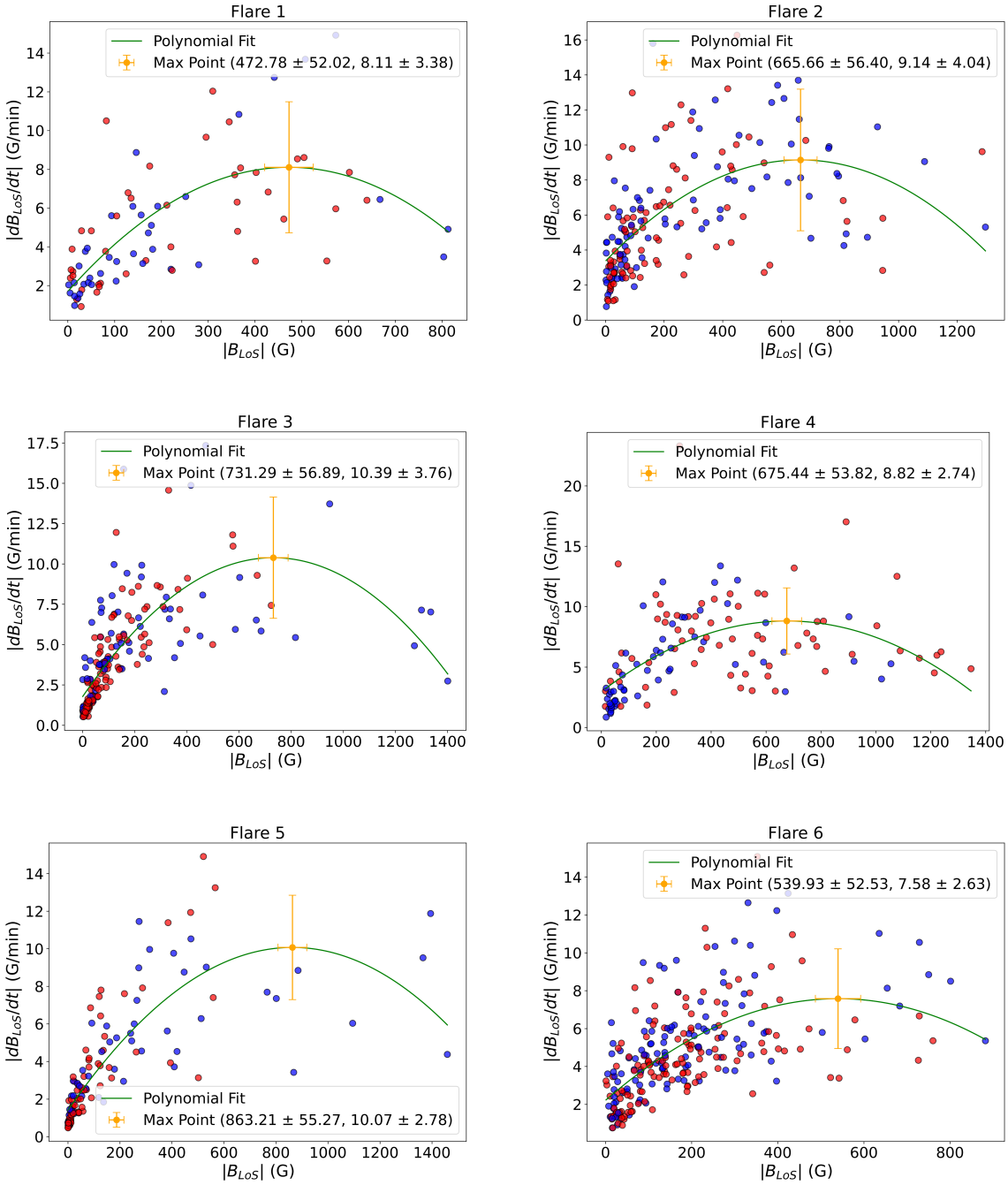

Figure 3.10: Scatter plots of absolute magnetic field ($|B_{\mathrm{LoS}}|$) and the rate of change of the magnetic field ($|dB_{\mathrm{LoS}}/dt|$) for the six selected flares. Each point represents a data box that meets the following conditions: (a) it belongs to the monotonic clusters, and (b) the time lag is restricted to a range of ±20 minutes. The points are colour-coded based on the sign of the magnetic field: blue for positive and red for negative. The green line represents the quadratic fit, which models the non-linear relationship between $|B_{\mathrm{LoS}}|$ and $|dB_{\mathrm{LoS}}/dt|$. The orange marker highlights the maximum rate of change ($|dB_{\mathrm{LoS}}/dt|$) determined from the fit, with error bars indicating the uncertainty of the measurement.

Table 3.4: The fraction of boxes with monotonic B_{LoS} changes and the fraction of those with monotonic B_{LoS} changes within a time lag range of ±20 minutes, based on the color-coded maps shown in Figure 3.9.

Flare No.	Fraction of Boxes with Monotonic B_{LoS} Change	Fraction of Boxes with Monotonic B_{LoS} Change within τ±20 Minutes
1	0.45	0.22
2	0.36	0.05
3	0.40	0.05
4	0.34	0.24
5	0.24	0.03
6	0.45	0.26

3.5 Discussion

Our study examines the spatial and temporal evolution of the line-of-sight (LoS) magnetic field in six M-class flares, with a focus on changes occurring within flare ribbon regions. It provides a comprehensive analysis of various types of magnetic field changes on the ribbons, explores the diverse behaviours of the LoS magnetic field during these flares, investigates the time lag between the most rapid field changes and UV emission, and maps the spatial distribution of the rate of change in B_{LoS}.

The main finding of our study is the establishment of a novel approach to capture the different variations in the LoS magnetic field using machine learning. By applying K-Shape clustering, we identified an average of six distinct types of LoS field variations. This finding is consistent with the results of Castellanos Durán et al. (2018), who reported several distinct types of magnetic field changes (12 in total, with 4 identified as magnetic transients). The spatial distribution of these variations, as shown in Figures 3.7 and 3.8, reveals regions of consistent behaviour, but also areas of mixed types. This irregular distribution likely reflects the complex nature of magnetic changes during solar flares, which are influenced by dynamic, localized coronal reconnection. Supporting this, Wang

et al. (2002) documented changes in the magnetic field that were sometimes concentrated near the core of the flaring neutral line, but other times more widely distributed across a sunspot. In addition, based on the analysis of the temporal evolution of the LoS magnetic field behaviour and the UV emission in flare ribbons, we identify three categories:

1. Monotonic magnetic change with maximum rate of change of B_{LoS} preceding UV emission peaks.
2. Monotonic magnetic change with maximum rate of change of B_{LoS} lagging UV emission peaks.
3. Oscillatory behaviour in the magnetic change.

Building on the clustering method used to identify the various LoS field changes, this section is divided into two key components: 1) a comprehensive evaluation of LoS field changes across all clusters, and 2) an analysis of LoS field changes specifically for boxes belonging to the monotonic clusters, and with a time lag restricted to a range of ±20 minutes.

3.5.1 Overall LoS Field Changes Evaluation

This section evaluates the LoS field changes across all clusters, without any restrictions, and analyzes the results from all boxes within the area of the cumulative ribbon. We found significant variability in the time lag (τ), demonstrated in the colour-coded map in Figure 3.4, with flares exhibiting both positive and negative lags. Within this varied behaviour, there is a systematic pattern of higher time lags, represented by darker-coloured patches on the map, appearing particularly associated with areas of weaker magnetic fields, seen in Flares 2, 3, 5, and 6.

In the analysis of Table 3.2, we found that 4 out of the 6 flares have, on average, a negative time lag τ, indicating that in general the most rapid changes in the photospheric LoS magnetic field occurred before the peak in UV emission. The longest average time lag observed was 10.82 min. The standard deviation of the time lag (σ_τ) obtained from all the sampled boxes within the flare ribbons, was relatively high, with a mean value of 25.65 minutes.

We found that the rate of change in the LoS magnetic field on the cumulative flare ribbons varies between 2 and 25 gauss per minute. Additionally, Figure 3.6 shows a relationship - albeit with high scatter, between the rate of change of the magnetic field $|dB/dt|$ and the absolute LoS magnetic field $|B_{\mathrm{LoS}}|$. A quadratic fit shows that the maximum rate of change, averaging 10.4 G/min, occurs in regions with magnetic fields of 480 to 760 G. This suggests that stronger magnetic fields are linked to faster and stronger magnetic changes in flare ribbons. However, as the LoS field continues to increase the rate of change starts to decrease, suggesting that it is harder to perturb the strongest field.

The possible physical interpretations of the variety of LoS magnetic field behaviours on the cumulative flare ribbons can be divided into two scenarios. Firstly, when we observe a stepwise change that aligns with the background trend, resulting in an overall monotonic variation under the monotonic category, particularly close to the polarity inversion line, it is consistent with the implosion mechanism (Hudson, 2000), where reconnection allows the field to contract to a lower-energy state. This interpretation has been discussed in this context by several authors (e.g. Johnstone et al., 2012; Sun et al., 2017). Secondly, gradual increases and decreases under the monotonic category, along with oscillatory behaviour, may be flare-related and warrant further investigation, particularly if it occurs in locations in or near the sunspot and PIL. But these behaviours may also result from local photospheric processes that are not related to actual variations of the field, such as small flux concentrations moving into and out of our 3×3 boxes, particularly when observed far from the strong-field regions or the polarity inversion line.

3.5.2 Monotonic LoS Field Changes Evaluation

We repeated the analysis on target boxes within the cumulative flare ribbons that met the two conditions of belonging to the monotonic clusters and having time lags restricted to a range of ±20 minutes. We assume that these are more likely to be flare-related. The results presented in Figure 3.9 generally do not reveal any clear spatial pattern. We still identify both positive and negative time lags. However, isolating monotonic clusters gives an average time-lag that is closer to zero. The scatter plots in Figure 3.10 show a similar behaviour to that found for all locations in the flare ribbon, with a peak rate of change of about 10 gauss per minute, consistent with the 10s of gauss per minute found previously by Sudol and Harvey (2005). The fraction of boxes exhibiting monotonic changes in B_{LoS} within the flare ribbons is low, underscoring the rarity of monotonic (e.g., stepwise) changes in the magnetic field in these regions, as reported by Petrie and Sudol (2010).

Assuming that this sub-set of changes in B_{LoS} are flare-related, it is useful to explore possible physical reasons for both positive and negative lags appearing. The relationship between the time of peak UV and maximum rate of change of photospheric B_{LoS} will be influenced by the rise time of the UV emission (in turn determined by the rate of heating and cooling of the chromosphere) versus the rate at which magnetic changes propagate through the chromosphere to where the magnetic signal is generated. If the rise time to peak UV emission is long compared to the time taken for a magnetic change to propagate to the photosphere then the strong changes in the LoS magnetic field could precede the UV, and vice versa if the rise time is short.

The time taken for UV emission to reach its peak has been studied at 1600 Å by Qiu et al. (2012), who found that this ranged from a few to 30-40 minutes. The time required for a flare-driven magnetic disturbance to propagate through the chromosphere and produce a detectable change in the photospheric magnetic field is likely somewhat shorter. We

can estimate this by noting that most of the contribution to the Fe I line used in the HMI magnetic field diagnostic originates below 300 km above the photosphere, peaking around the centre of this region (Figure 4 of Monson et al., 2021). Modeling by Russell and Fletcher (2013) shows that an Alfvénic perturbation propagating in a plage chromospheric model with a 500 G photospheric field strength, should reach 300 km in ∼50s. Propagation below 300 km will add significantly to this, since the density scale height at this altitude is small – around 120 km – reducing the Alfvén speed. The propagation time is also correspondingly longer in lower-field regions, so in a 50 G field one might expect timescales of ten minutes or more. So within this range of variability of both UV and magnetic field evolution, lags of minutes in either direction are possible.

We note that other studies present a mixed picture of time lags, depending on the flare class, the wavelengths analysed, and the definition of the timing measurements used. Johnstone et al. (2012) and Yadav and Kazachenko (2022) looked at the relationship between the start times of magnetic field changes and UV emission, finding that the start of observable field changes tend to lag the start of observable enhancements in UV emission by typically 4 minutes (and up to 19 minutes). In these studies, the start times for the field changes are defined by the step-like fitting function. However, the start time of a light curve can be hard to interpret, since it depends on choosing a threshold value, which typically also depends on the instrument noise level. So looking at peak times is less ambiguous. Burtseva et al. (2015) found that the time of the maximum rate-of-change for a step-like magnetic field change - i.e. the midpoint of the step-like function, tended to precede the peak of HXR ribbon emissions by a few minutes. HXR emission gives a clearer view of the time of the maximum energy input than UV. Sun et al. (2017) also found that the midpoint of step-like changes in the magnetic field in one flare tended to precede the peak of flare soft X-rays (which itself will lag the peak in the HXR emission). However, in 20% of locations examined there was a lag.

3.6 Conclusions

In this study, we investigated the evolution of the line-of-sight magnetic field during six M-class flares, focusing on the temporal and spatial relationship between magnetic field changes and UV emissions, the rate of change of the magnetic field on cumulative flare ribbons, and the types of magnetic field changes occurring within the ribbons. Our findings provide new insights into the dynamic processes that drive solar flares and contribute to the broader understanding of flare-triggered magnetic reconnection.

The key observational findings of this study are as follows:

1. There is substantial spatial variability and complex temporal relationships between magnetic field changes and UV emission peaks across flare ribbons. However, not all of these field changes are clearly flare-related.
2. The peak in UV emission can occur both before and after the time corresponding to the maximum rate-of-change of B_{LoS}.
3. In 4 out of 6 flares, on average the maximum rate of LoS magnetic field change precedes the peak UV emission, with the largest mean time lag of ~ 11 minutes. However, restricting to LoS field changes with a monotonic-behaviour and close temporal association with the UV peak, the largest mean lag is $\sim 2-3$ minutes with equal numbers of positive and negative lags.
4. The rate of change of the magnetic field on the cumulative flare ribbons ranged from 2 to 25 G/min, which aligns with previous findings.
5. The rate of change of B_{LoS} across flare ribbons correlates with the absolute value of B_{LoS}, with stronger fields associated with a high rate of changes, up to some maximum. A quadratic model effectively captures the relationship, with an average peak rate of change of 8.6 $\mathrm{G\,min^{-1}}$.

6. We identified an average of six types of magnetic field change per flare. These include clear oscillatory signals with typical periods ranging from 20 to 40 minutes and amplitudes around 70 G, estimated visually from the clustered time series behaviour during the analysis, as well as monotonic field changes as previously reported.
7. The proportion of boxes showing monotonic changes within the flare ribbons was relatively small, suggesting that monotonic magnetic field changes, especially step-like variations, are rare in these regions.
8. The complicated spatial distribution of magnetic field changes highlights the localised and dynamic nature of magnetic activity during flares.

We have proposed a possible explanation for both positive and negative time lags in flare-associated changes in terms of the variable UV rise times, and propagation times of a magnetic change to the photosphere, which suggests that the variation with position of magnetic field strength, mass density, and chromospheric heating and cooling rates in a flare could at least partially explain the observed variability. This could be further examined in future work. Despite the valuable insights gained from this investigation, the study is restricted to a small dataset. To achieve a more comprehensive understanding of magnetic field changes across different flare classes and to generalise our findings, it is essential to expand this analysis to include a larger number of flares, particularly across a wider range of flare classes. In addition, exploring the vector magnetic field may reveal further information about the restructuring of the magnetic field during flares, especially changes in the horizontal component that are expected from flare-related magnetic reconfiguration.

Chapter 4

Systematic Time Evolution of the Horizontal Magnetic Field Around the Polarity Inversion Line

The work presented in this chapter was published in Alanazi and Fletcher (2026). The analysis, data processing, and interpretation were carried out by the author, with guidance and discussion of the results and manuscript revision provided by the co-author.

4.1 Introduction

The evolution of the horizontal magnetic field ($\boldsymbol{B}_{\mathrm{h}}$) at the photosphere during solar flares provides important insight into how the photospheric field responds to coronal energy release. In this chapter, we investigate the spatial and temporal changes in $\boldsymbol{B}_{\mathrm{h}}$ by applying unsupervised machine learning, namely k-shape clustering, to identify regions exhibiting step-like changes in $\boldsymbol{B}_{\mathrm{h}}$. Johnstone et al. (2012) showed that the start of the photospheric line-of-sight field changes tended to lag that of the ribbons' UV emission by 4-9 minutes and were spatially coincident. Using high-cadence vector data, Yadav and Kazachenko

(2022) confirmed that increases in B_h near PILs typically lag the onset of UV emission, and the strength of the changes is correlated with ribbon properties like their area and the magnetic flux swept out. In addition, Cliver et al. (2012) found that in most events in their sample the beginning of the rapid change in photospheric unsigned magnetic flux coincides with the onset of the flare 'impulsive' phase which they defined as some threshold on the time derivative of the logarithm of the soft X-ray flux and ends at the soft X-ray peak. They interpreted this as evidence that restructuring in the corona is quickly communicated down to the photosphere. Furthermore, Burtseva et al. (2015) showed that photospheric field changes are closely associated with early hard X-ray sources, but in that study the magnetic field changes preceded or coincided with the onset of HXR emission, suggesting that magnetic reconfiguration begins before the main particle acceleration phase. Although these studies examined different flare samples, no clear dependence of these timing relationships on flare class has yet been established.

Recent statistical analyses have made significant progress in characterising both the temporal and spatial behaviour of changes in B_h. For example, Liu et al. (2022) examined 35 major flares ($\geq$M6.0) and showed that increases in B_h near PILs are a common flare property, with their magnitude and timescale scaling with initial ribbon separation, in line with reconnection-driven loop contraction. Similarly, Yadav and Kazachenko (2022) analysed 37 flares with high-cadence vector data and demonstrated that horizontal field changes are concentrated near PILs, step-like in nature, and strongly correlated with ribbon flux and area. Despite these advances, most previous studies have focused primarily on increases in B_h near PILs or have relied on event-averaged measurements, leaving the detailed spatial distribution and timing of both increases and decreases across active regions less explored. In addition, identifying step-like changes has often relied on predefined fitting models, which can limit the ability to analyse large datasets systematically.

In this work, we build on these recent statistical studies by taking advantage of the fine spatio-temporal evolution of variations in B_{h}, to consider both increases and decreases across entire active regions, comparing their timing more directly with the ribbon brightening. By applying a machine learning-based method, we automate the identification of regions of step-like changes B_{h} in a survey of 35 flares. We construct spatially and temporally resolved maps of B_{h} changes, both increasing and decreasing, relative to the onset of the flare defined by the first appearance of UV ribbons. This approach provides a new perspective on the timing and spatial distribution of photospheric magnetic restructuring near PILs and allows the results to be compared with expectations of the 'implosion' model, where the coronal magnetic field contracts around the PIL via reconnection.

This chapter is organised as follows: Section 4.2 presents the observations, Section 4.3 presents methodology, Section 4.4 the results, section 4.5 the discussion, and Section 4.6 summarises our conclusions.

4.2 Observations

4.2.1 Event Selection and Instruments

Our flare sample is drawn from the FlareMagDB database (Kazachenko et al., 2022b), a set of 35 well-observed flares: 8 X-class, 26 M-class, and 2 C-class selected for their high-quality, multi-wavelength coverage. These events span 2010–2015 and are located within 45° of disk centre to minimise projection effects, ensuring reliable measurements of both chromospheric emission and photospheric magnetic fields. We also use observations from two instruments aboard the *Solar Dynamics Observatory* (SDO; Pesnell et al., 2012a). First, the *Atmospheric Imaging Assembly* (AIA; Lemen et al., 2012) provides full-disk ultraviolet images at 1600 Å with $0.6''$ pixels and a 12 s cadence. The 1600 Å

channel samples the low chromosphere and transition region, enabling identification and tracking of flare ribbon brightening. Second, the *Helioseismic and Magnetic Imager* (HMI; Scherrer et al., 2012) delivers full-disk vector magnetograms at $0.5''$ pixels and 135 s cadence, derived via Milne–Eddington inversion of the Fe I 6173 Å Stokes profiles. These high-cadence vector data are ideal for quantifying rapid changes in the horizontal magnetic field during flare evolution.

4.2.2 Data Preprocessing

For this study, we use full-disk vector magnetogram data from the 135-second cadence HMI series (`hmi.B_135s`; (Sun et al., 2017)) to analyse the temporal evolution of the horizontal magnetic field in flare-active regions. To resolve the 180 ° ambiguity in the transverse field direction, we apply the radial-acute disambiguation method (Hoeksema et al., 2014) using our custom Python routine (`hmi_disambig.py`), which reproduces the SolarSoft `hmi_disambig.pro` logic. Following disambiguation, we transform the field strength, inclination, and azimuth into heliocentric spherical components—B_r (radial), B_ϕ (westward), and B_θ (southward)—via our `hmi_b2ptr.py` module, which parallels the SolarSoft `hmi_b2ptr.pro` routine. We then compute the horizontal field as:

$$B_h = \sqrt{B_\phi^2 + B_\theta^2} \tag{4.1}$$

To ensure we were consistently tracking active regions, we applied solar rotation correction using SunPy's `propagate_with_solar_surface()` tool. This approach enabled us to update the position of the region of interest (ROI) across time steps, taking into account the solar differential rotation. At each time stamp, we extracted a fixed-size cutout

Table 4.1: Summary of HMI data processing steps.

Step	Tool/Function	Description
1	`hmi.B_135s`	Download vector magnetic field data from the HMI 135-second cadence series.
2	`astropy.io.fits`	Load HMI vector magnetic field data (field strength, inclination, azimuth) and disambiguation maps.
3	`hmi_disambig`	Resolve the 180° ambiguity in azimuth angle.
4	`hmi_b2ptr`	Convert magnetic field vectors to heliographic components (B_r, B_ϕ, B_θ).
5	NumPy	Compute horizontal field: $B_h = \sqrt{B_\phi^2 + B_\theta^2}$.
6	`sunpy.map.Map`, `rotate()`	Create SunPy map and apply rotation for standard orientation.
7	`SkyCoord`	Define the initial centre of the region of interest (ROI) in arcseconds.
8	`propagate_with_solar_surface()`	Apply solar differential rotation to track the ROI centre over time.
9	`submap()`	Extract a fixed-size rectangular cutout around the updated ROI centre.

centred on the rotated coordinate using the `submap` function in SunPy. A summary of detailed HMI data processing steps is listed in Table 4.1. Finally, to ensure that weak, noisy signals were eliminated we used the same field strength threshold as Kazachenko et al. (2022b), including only pixels with a mean B_h greater than 100 G.

4.3 Methodology: X2.1 Flare on September 6, 2011, as an Example

4.3.1 Identification of Flare Ribbons

As a fixed base of time comparison, we will take the time of first appearance of flare ribbons at 1600Å. The logic for this choice is threefold: the appearance of UV ribbons indicates that energy has arrived in the chromosphere (unlike soft X-rays which could have a coronal component); because it does not require strong energy input to produce this emission they should occur promptly after the start of energy release in the corona; they should be detectable in all flares. Flare ribbons were identified using the method described in Chapter 3.3.1, following Toriumi et al. (2017). Pixels in AIA 1600 Å images exceeding 40 times the standard deviation above the quiet-Sun mean intensity were classified as ribbon pixels, where the quiet-Sun intensity was estimated from a selected quiet region on the solar disk. A cumulative ribbon mask was then constructed from the binary ribbon maps over the duration of the event.

During an intense flare, CCD saturation and bleed can cause the ribbon detection to fail. To address this, we applied the empirical correction method of Kazachenko et al. (2017), where pixels exceeding a saturation threshold of 5000 DN/s were identified, along with their surrounding pixels within a 2–10 pixel radius in both x and y directions. In our implementation, we adopted a fixed ± 10 pixel window which ensures that all nearby affected pixels are consistently corrected. For each affected pixel, we interpolated its intensity in time using its nearest unsaturated values before and after the saturation period. This allowed us to constrain the interpolation to only the saturated frames. We used linear interpolation, consistent with the original method, and corrected only when valid bracketing values existed. Frames without reliable bracketing were excluded from correction. This approach does not aim to recover accurate photometric values but provides sufficient

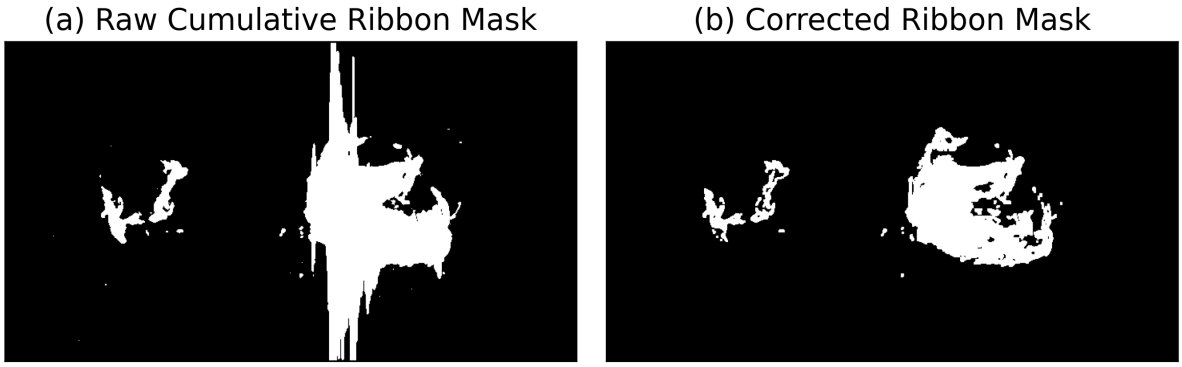

Figure 4.1: (a) Raw cumulative flare ribbon mask derived from the original AIA 1600 Å image sequence of an X2.1 flare on September 06 2011, showing all pixels that exceeded the intensity threshold during the flare. (b) Cumulative ribbon mask after applying the saturation correction procedure of Kazachenko et al. (2017).

morphological clarity to identify flare ribbon structure. Figure 4.1 shows an example of the saturation correction applied to Flare 4 on the data set listed in Table 4.2: the X2.1 flare on September 6, 2011, where panel 4.1(a) displays the raw cumulative flare ribbon mask and panel 4.1(b) shows the cumulative ribbon mask after applying the saturation correction. This shows that the resulting binary map more accurately represents the true flare ribbons.

4.3.2 Determination of the Region of Polarity Inversion (RoPI)

The reconnection-driven implosion scenario predicts that B_{h} increases around the polarity inversion line - or more generally and in the case of complex distributions of field - the *region of polarity inversion* (RoPI). So we need an automated means to identify this. We followed the method described by Ji et al. (2023), using the radial component of the magnetic field, B_r, derived from SDO/HMI vector magnetograms. Firstly, two binary masks were constructed: one for positive polarity, where pixels with $B_r > 100\,\mathrm{G}$ were set to 1, and one for negative polarity, where pixels with $B_r < -100\,\mathrm{G}$ were set to -1. All other pixels were set to 0. Then, small isolated polarity regions were removed by applying a size filter that excluded regions smaller than 14 pixels (approximately 1.86 Mm^2), to reduce

noise and retain only meaningful magnetic structures. Next, the edges of the positive and negative polarity regions were extracted using the Canny edge detection algorithm, which employs a Gaussian filter to smooth the magnetogram images and extract the large-scale contours of the polarity regions.

After that, the extracted edges were spatially expanded using a 4-pixel morphological dilation. The RoPI was then defined as the overlapping area between the buffered positive and negative edge maps. Then, the unsigned magnetic field strength was computed within each RoPI area. Only the RoPI regions that collectively contributed at least 95% of the total unsigned flux across all RoPIs were retained, effectively removing the weakest ∼5% of low flux RoPIs. This step ensured that only the most magnetically significant inversion regions were included. Following that, a morphological thinning operation was applied to the selected RoPIs. This reduced them to narrow, 1-pixel-wide lines while preserving their general shape, effectively extracting the PIL skeleton. Finally, a second size filter was applied to remove very small inversion lines (less than 14 pixels in length), retaining only the larger PIL segments. An example of this method is presented in Figure 4.2 of Flare 4, which displays the B_r map on the background with the extracted RoPI overlaid in pink.

After identifying the flare ribbon and determining the RoPI in each flare in the data set, we defined a box that includes the cumulative ribbons as the region of interest (ROI). Each pixel within this box was then analysed to investigate the evolution of the horizontal magnetic field. An example is shown for Flare 4 in Figure 4.4, where the white box denotes the ROI, which also contains the RoPI.

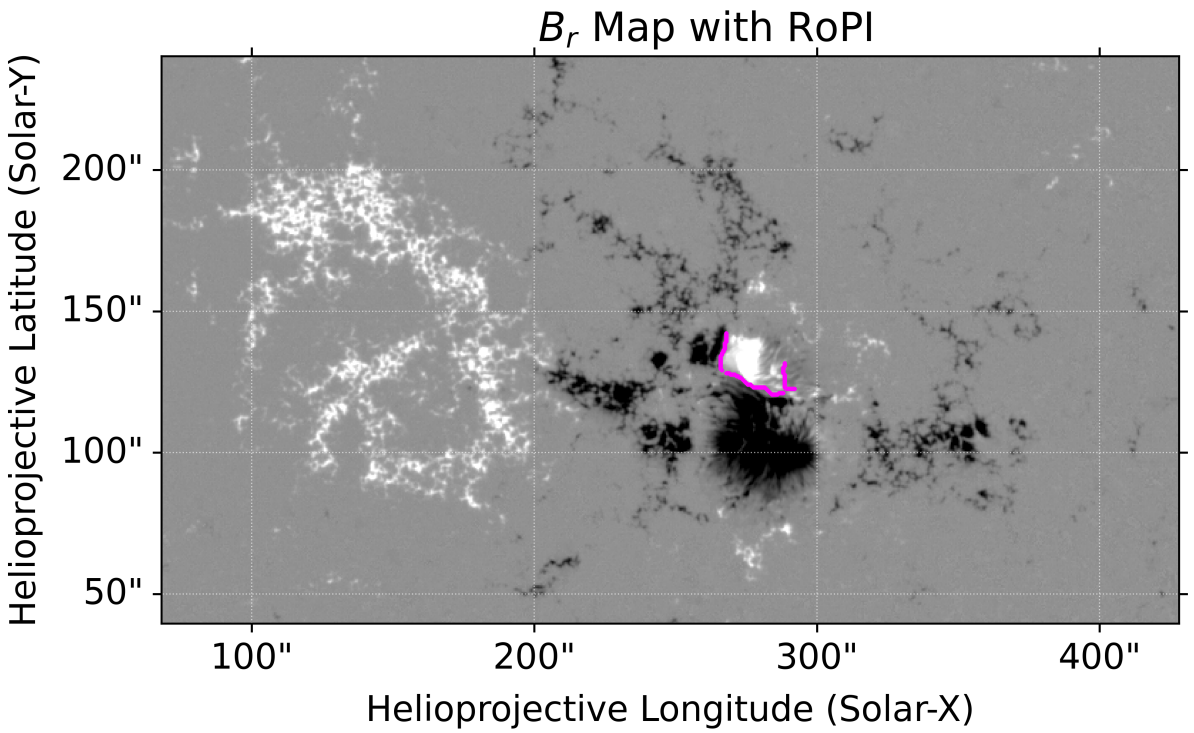

Figure 4.2: Radial magnetic field map (B_r) from SDO/HMI at time t_0 of an X2.1 flare on September 06 2011, showing the photospheric magnetic field structure of the active region with the extracted Region of Polarity Inversion (RoPI) in pink. The RoPI is identified using the method of Ji et al. (2023). See text for details.

4.3.3 Identifying Step-like Magnetic Field Changes Using Machine Learning (K-Shape Clustering Method)

In most previous studies, step-like changes have been characterised by fitting a function (introduced by Sudol and Harvey, 2005) to time series extracted from magnetogram data, and retaining acceptable fits. We take a different tack, first of all identifying regions of step-like changes in $B_{\rm h}$ using a clustering algorithm, and then characterising their properties. We use the K-Shape clustering algorithm from the tslearn Python package. The k-Shape method was introduced in Chapter 3 (Section 3.3.3.3) where it was used to classify different types of temporal behaviour in the line-of-sight magnetic field ($B_{\rm LoS}$) within flare ribbons. In contrast, in this chapter, we use the same technique to identify and isolate pixels showing step-like changes in the horizontal magnetic field ($B_{\rm h}$) across the active region. As discussed previously (Section 2.4), K-Shape clustering, like K-Means,

groups data according to its shape, but it is better for time series analysis than K-Means because it is not sensitive to the amplitude and phase (i.e. the start time or time-scale) of the signal and is thus suited for identifying similar-shaped changes that occur with different amplitudes, onsets and durations in different locations.

To reduce noise while maintaining the overall trend, we used Savitzky-Golay filtering (Savitzky and Golay, 1964), which convolves the signal with a low-degree polynomial fitted to successive groups of points using linear least squares. Then, for each pixel (x,y), we constructed a time series vector:

$$\mathbf{B}_{x,y} = \left[B_{\mathrm{h}}^{(1)}(x,y), B_{\mathrm{h}}^{(2)}(x,y), \ldots, B_{\mathrm{h}}^{(41)}(x,y)\right],$$

where $B_{\mathrm{h}}^{(t)}(x,y)$ is the horizontal magnetic field magnitude at time index t. These vectors are the input to the K-Shape algorithm, allowing us to cluster pixels based on the similarity of their magnetic field evolution profiles over time. The method identified approximately 6-10 different shape-based clusters.

We then visually identified the clusters that exhibit step-like behaviour. Figure 4.3 illustrates this for Flare 4: Cluster 0 shows a step-like increase in B_{h} while Cluster 2 shows a decrease which is less clearly step-like, but is characterised by a relatively rapid transition between two quasi-stable levels, rather than a continuous linear decline. (We note that the distortions at the final time steps are due to edge effects in the centroid computation in K-Shape, but do not impact the identification of the main step-like patterns.) A spatially colour-coded map of the corresponding pixels, where blue denotes an increase in B_{h} and red denotes a decrease, is shown in Figure 4.4. In this event, the step-like increases are concentrated around the RoPI, whereas step-like decreases are located farther away. Clusters where B_{h} is only increasing or only decreasing, but which are outside the

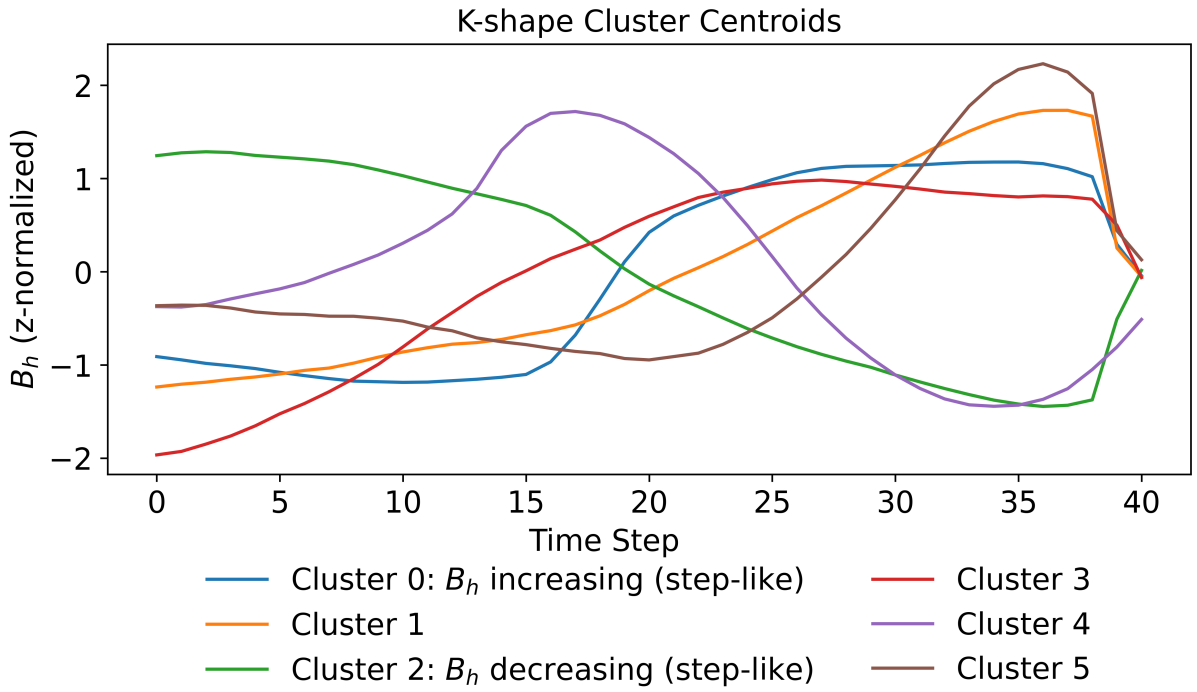

Figure 4.3: Example of K-Shape clusters for Flare 4, an X2.1 flare on September 06 2011, where Cluster 0 exhibits a step-like increase and Cluster 2 shows a step-like decrease in B_h. The distortions at the final time steps are due to edge effects in the centroid computation in K-Shape, but do not impact the identification of the main step-like patterns. The x-axis represents the sequential HMI data points (135 s cadence). For context, the time between GOES onset and end times was 12 minutes, and the onset-to-peak duration - roughly the impulsive phase - was 4 minutes.

cumulative ribbon mask, could be systematic changes in the larger-scale field in response to the change in the core flare field. However, regions where increasing and decreasing changes are mixed are most likely just showing normal small-scale changes in network field unrelated to the flare.

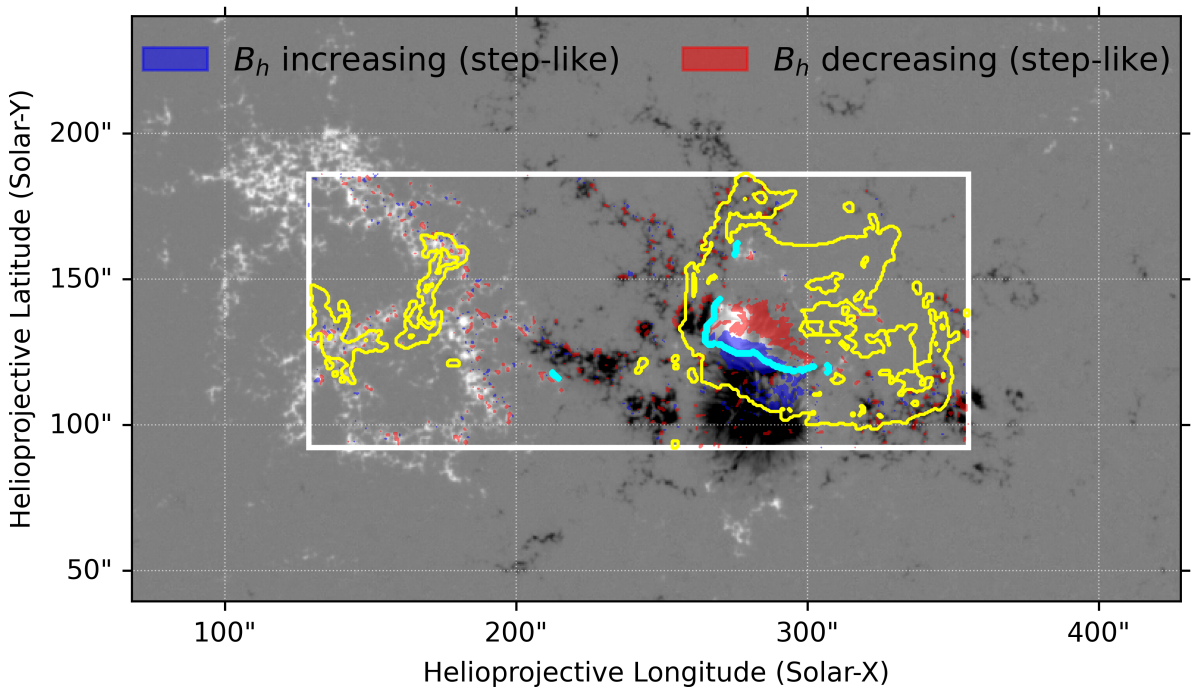

Figure 4.4: Spatial distribution of pixels exhibiting step-like changes in the horizontal magnetic field (B_h) during Flare 4. Blue regions correspond to step-like increases in B_h, while red regions indicate step-like decreases. The background shows a radial magnetic field map, with yellow contours outlining the AIA 1600 Å flare ribbons, cyan contours outlining the Region of Polarity Inversion, and a white box marking the region of interest (ROI).

4.3.4 Temporal Relationship Between $B_{\rm h}$ Evolution and Flare Ribbon Emission

To identify the timing of the most significant changes in the horizontal magnetic field, we follow the approach described by Alanazi and Fletcher (2025). For each pixel belonging to the step-like $B_{\rm h}$ clusters, we constructed a time series of the smoothed $B_{\rm h}$. Then, rather than fit a function to the step-like change to identify its midpoint, we calculate the absolute value of its temporal derivative, $|dB_h/dt|$, defined as

$$\left|\frac{\mathrm{d}B_{\mathrm{h},i}}{\mathrm{d}t}\right| = \left|\frac{B_{\mathrm{sm},i+1} - B_{\mathrm{sm},i}}{\Delta t}\right|, \tag{4.2}$$

where $B_{\mathrm{sm},i}$ is the smoothed value of $B_{\rm h}$ at time index i, and Δt is the cadence between observations, which is 135 sec. We define the time corresponding to the peak value of $|\frac{\mathrm{d}B_{\rm h}}{\mathrm{d}t}|$ as the time at which the most rapid change in the horizontal field occurred, denoted t_B. We intentionally adopt this time, rather than attempting to identify an initial onset of the field change as other authors have done, because it is clearly identified and because identification of the onset time depends on the noise level. We take this as representative of the time of the maximum photospheric magnetic response to flare-related energy release. To investigate how $B_{\rm h}$ evolves in relation to the timing of early flare ribbons, we examine the spatial and temporal relationship between the onset of the initial ribbon brightening and the magnetic field change. We define the corresponding time lag, τ, as:

$$\tau = t_B - t_{UV}, \tag{4.3}$$

where t_B is the time of the maximum rate of change in the horizontal field and t_{UV} is the onset time of the first flare ribbons observed in the AIA 1600 Å channel. So a positive τ means that the rate of change of $B_{\rm h}$ peaks after the UV ribbons first appear.

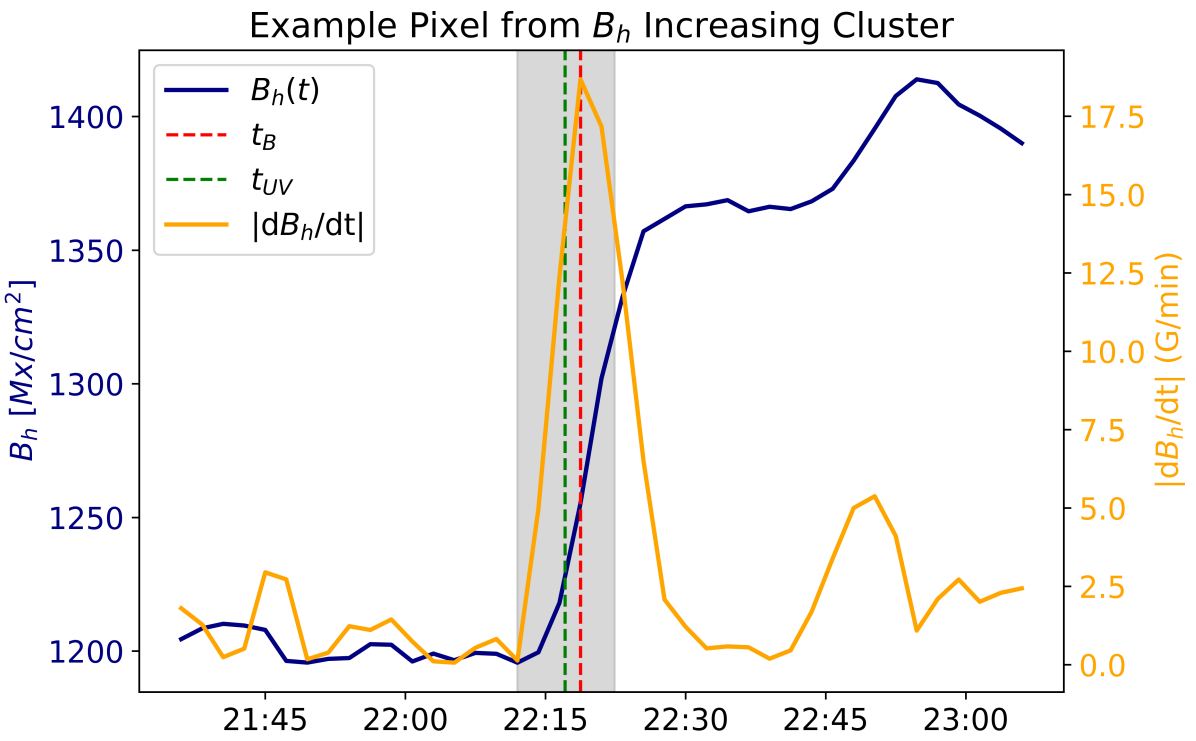

Figure 4.5: Example pixel from the B_h-increasing cluster in Figure 4.3. The blue curve shows the smoothed temporal evolution of the horizontal magnetic field $B_h(t)$, and the orange curve shows its absolute time derivative $|dB_h/dt|$. The vertical dashed lines indicate the fitted time of the magnetic field change (t_B, red) and the time of first appearance of UV emission (t_{UV}, green). The grey shaded region marks the flare GOES period.

Applying Equation 4.3 gives a time lag τ for each pixel; in the case shown here a total of 4409 pixels were analysed. Figure 4.5 shows an example of the data from a pixel from the B_h-increasing cluster (Cluster 0 in Figure 4.3), where the step-like change in B_h is clear. The red and green dashed lines indicate t_B and t_{UV}, respectively and illustrate a delay of roughly one minute between them.

The illustration of the spatial distribution of the time lags for Flare 4 is shown in the top panels of Figure 4.6. In the B_h increasing cluster (Cluster 0; top left), the mainly positive τ values indicate that the horizontal field changes follow the onset of UV ribbon brightening. In contrast, the B_h decreasing cluster (Cluster 2; top right) shows a less coherent pattern with some negative lags. These patterns highlight a complex magnetic response. Details are examined further in the Results section.

4.4 Results

We first present four events to illustrate the temporal–spatial characteristics of step-like changes in B_{h}. These are all examples of cases where there is a concentration of step-like changes around the PIL. We then extend the analysis to the full set of 35 flares, summarising the statistical distributions of these changes and their relation to flare class and time of ribbon appearance.

4.4.1 Example Events

4.4.1.1 X2.1 Flare on September 6, 2011

We first examine the X2.1 flare in NOAA AR 11283 (N14W18) on 2011 September 6. Panels (a–b) of Figure 4.6 show the colour-coded time lag (τ) maps for the increasing and decreasing clusters and some interesting patterns emerge (note, the lags are cropped at ± 10 minutes). The full range of measured time lags extends from approximately -40 to $+40$ minutes, in some cases exceeding the total flare duration. Such long lags in either direction may include contributions from background magnetic fluctuations exhibiting step-like behaviour. The ± 10 minute clipping is for visualisation only, to focus on flare-related changes around the main energy release and does not affect the statistical calculations in the next section, which use the full distribution:

1. The horizontal field tends to increase near the RoPI, consistent with earlier studies (e.g. Liu et al., 2022), while part of the decreasing field is located within the sunspot penumbra.

2. The time lag τ shows a coherent behaviour in space, with patches of longer and shorter lags at different locations along the PIL in the $B_{\rm h}$-increasing cluster. This suggests that the field restructuring occurs earlier in the north-east part of the region, with τ values around 1 minute. In this north-east region, the longer time-lags occur farther from the PIL.
3. In the $B_{\rm h}$-decreasing cluster the shortest time lag also occurs in the north-east suggesting that the field is opening up here as it closes down around the PIL. Longer time lags, up to at least 10 minutes, occur throughout the rest of the $B_{\rm h}$-decreasing cluster possibly corresponding to a delayed expansion or opening of the larger-scale field.

   Panels (c–d) display the maximum rate of change, $|{\rm dB_h/dt}|_{\rm max}$, for the same clusters, and we find:

4. the highest rates of change reach up to $\sim$20 G min^{-1}, comparable to the values reported for longitudinal field changes in major flares (Sudol and Harvey, 2005).
5. These strong and rapid changes are concentrated in the sunspots suggesting that the umbral and penumbral field is significantly disturbed in this event.
6. The regions of highest rate of change correlate roughly with the shortest time lags, indicating that the most rapid field evolution occurs early in the event.

4.4.1.2 X5.4 Flare on March 7, 2012

The second example is the X5.4 flare in NOAA AR 11429 on 2012 March 7. This event, one of the most energetic in our sample, provides a good case of widespread step-like changes in the horizontal magnetic field across both polarities. Panels (a–b) of Figure 4.7 show the colour-coded time-lag maps. In this event we find the following:

1. Again the horizontal field tends to increase around the RoPI and to decrease just beyond this, on the eastern side.

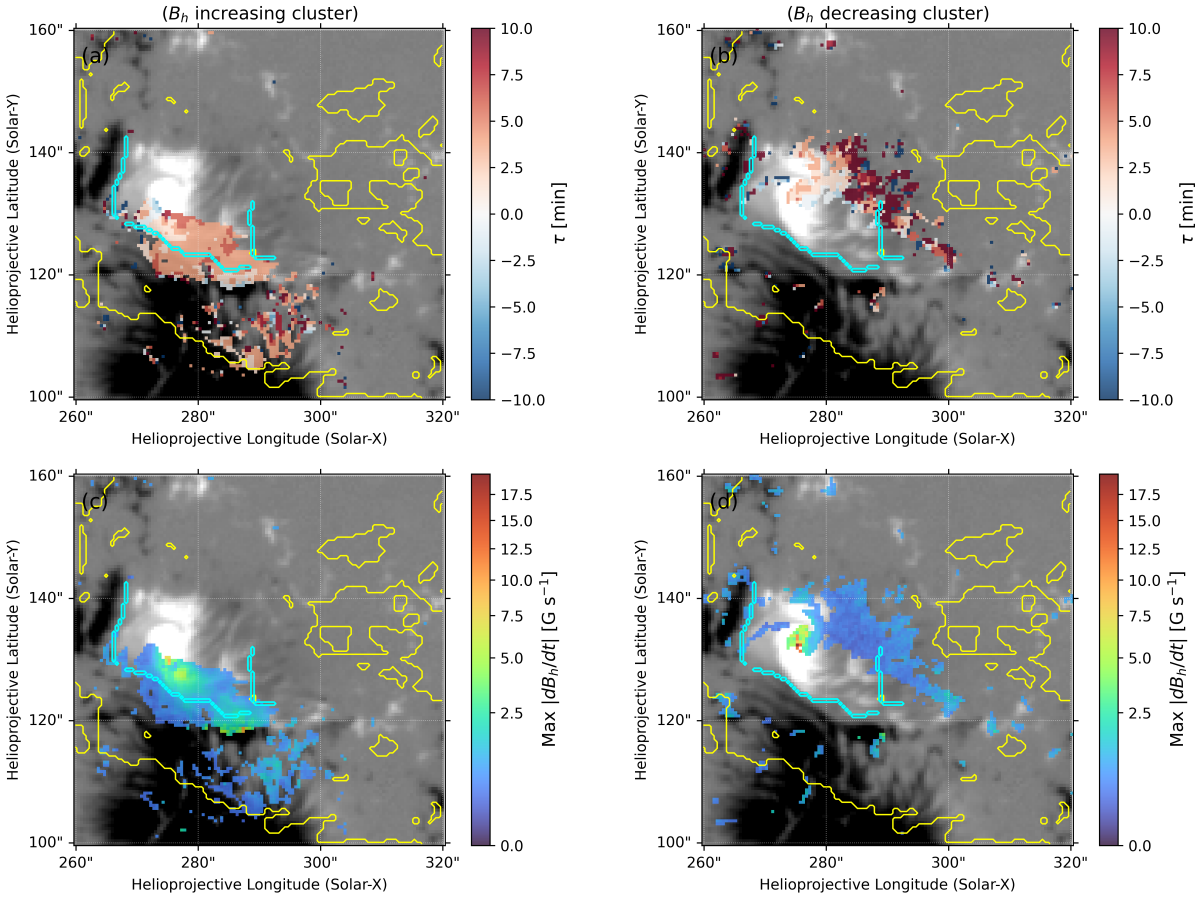

Figure 4.6: Temporal–spatial analysis of magnetic field evolution for the X2.1 flare on 2011 September 6. Panels (a–b): colour-coded maps of the time lag τ for pixels in the B_{h}-increasing (a) and decreasing (b) clusters. Yellow contours mark the cumulative flare ribbons; the cyan outline marks the RoPI. Panels (c–d): corresponding maps of the maximum rate of change $|dB_h/dt|_{\max}$

.

2. The time lag τ of the B_h-increasing cluster (panel a) increases fairly systematically with distance from RoPI. It is distributed along more of the PIL with lags from $\sim$ 1-5 minutes close to the PIL, and 10 minutes farther away. The evolution of B_h in this event looks fairly consistent with what would be expected from sequential reconnection, starting first close to the PIL and then progressing to field rooted farther away from it. Within this overall pattern, there are small patches of similar time-lags.
3. The B_h-decreasing clusters (panel b) are mostly concentrated in the negative polarity regions and display longer delays of $\sim$5–10 minutes relative to the early UV ribbons brightening, again with changes occurring earlier closer to the PIL.

   The maximum rate of change, $|dB_h/dt|_{max}$, is shown in Panels (c–d) for the same clusters, and we find:

4. In this event too, a small patch of large values occurs within the positive polarity sunspot, while more moderate rates of change are concentrated along the RoPI and then gradually decline with distance away from it
5. Again we noticed that the higher rates of change tend to coincide with the shortest time lags, indicating that the fastest evolution occurs early in the event.

4.4.1.3 M3.9 Flare on August 25, 2014

As a third example, we examine the M3.9 flare in NOAA AR 12146 on 2014 August 25. Panels (a–b) of Figure 4.8 show the time-lag maps for the B_h-increasing and decreasing clusters. The B_h-increasing cluster (panel a) occurs mainly along the RoPI, with a pattern of shorter time lags closer to the PIL. The size of this cluster is small compared the X-class flares already shown. The decreases (panel b) are concentrated near the positive-polarity penumbra and have predominantly positive values of τ of a few to 10 minutes. This could be consistent with penumbral field becoming less horizontal. A significant part of the B_h-decreasing patch is outside the flare ribbon meaning that it cannot be due to changes

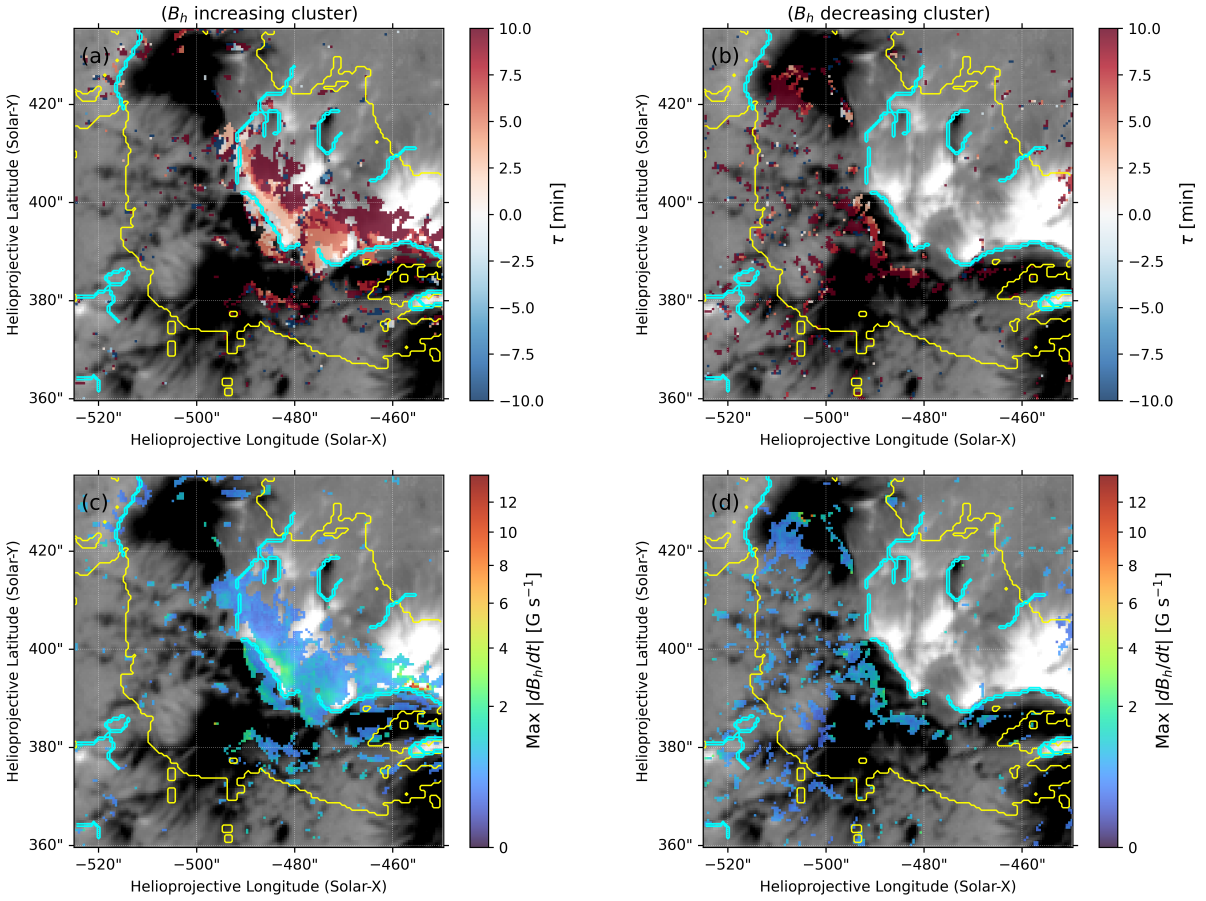

Figure 4.7: Same as Figure 4.6, but for the X5.4 flare on 2012 March 7 in NOAA AR 11429.

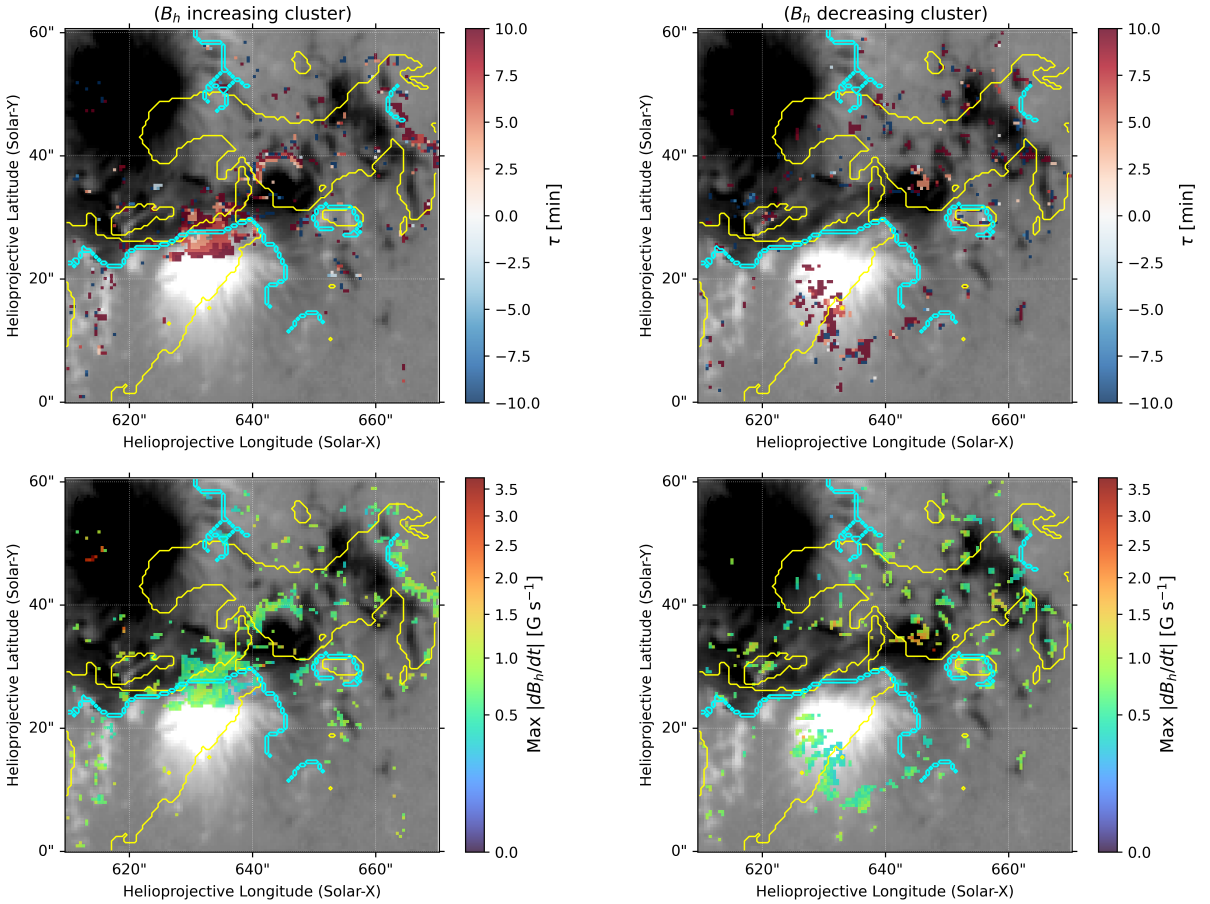

Figure 4.8: Same as Figure 4.6, but for the M3.9 flare on 2014 August 25 in NOAA AR 12146.

caused directly by reconnection, but could indicate a more large-scale re-organisation of surrounding field. However it should be noted that in and near the sunspot penumbra the horizontal field might be expected to vary due to penumbral flows/sunspot moat flows so this could also play a role particularly in patches with mixed-sign time lags. For the maximum rate of change, $|dB_{\rm h}/dt|_{\rm max}$, shown in Figure 4.8 panels (c–d), the values range from ∼0.5 to 1.5 G min^{-1}, with the highest rates concentrated within the negative polarity sunspot.

4.4.1.4 X2.2 Flare on February 15, 2011

As the final example, we show the X2.2 flare of February 15, 2011. Panels (a–b) of Figure 4.9 display the time-lag maps for the B_h increasing and B_h decreasing clusters. The key patterns are:

1. The horizontal magnetic field mainly increases around the RoPI. The B_h-decreasing locations are more scattered, though there is small patch of B_h-decreasing field in the northern section of the negative polarity sunspot.
2. The time lag τ of the B_h increasing cluster (panel a) exhibits coherent patches, and near the RoPI the lags are short (up to $\sim$2 minutes), whereas farther from the PIL they are as long as $\sim$10 minutes.
3. The time lag τ of the B_h decreasing cluster (panel b) shows no clear spatial coherence. Apart from the small region in the negative sunspot, the lags appear as a scattered mix of positive and negative delays throughout the active region, and are likely due to random changes in weaker field.
4. For the maximum rate of change, $|dB_\mathrm{h}/dt|_\mathrm{max}$ there are concentrations of the strongest rates in both the negative and positive polarity sunspots.

This event was also analysed by Petrie (2013) who found strong increases in the tilt angle of the magnetic field (with respect to local vertical) around the RoPI, compared at two times separated by 24 minutes. This is consistent with the increase in horizontal field that we find. Petrie (2013) also found a more widespread and apparently weaker decrease in the tilt angle (decrease in horizontal field) in the sunspots. It is possible that our algorithm has not detected this if it was too weak, or too slow to have been included in the step-like cluster.

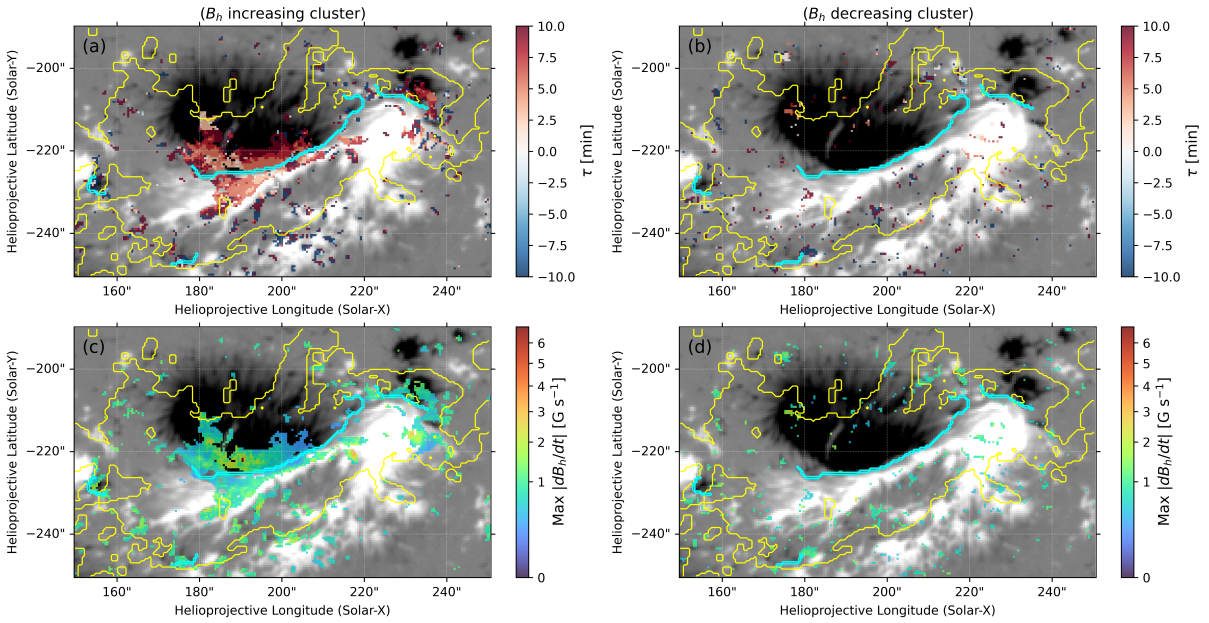

Figure 4.9: Same as Figure 4.6, but for the X2.2 Flare on February 15, 2011 in NOAA AR 11158.

These four case studies demonstrate some consistent patterns across different flare classes. In all cases, step-like changes in B_h are closely linked to the early flare ribbons near the RoPI, with detected time lags starting from $\sim$ 1 minute (measured with respect to the time of first UV ribbon appearance) and increasing systematically with distance from this region. Within this there are small but coherent patches of similar time lag, which might suggest patchy coronal reconnection. In addition, we found that the regions exhibiting the highest rates of change correlate roughly with the shortest time lags, implying that the strongest magnetic evolution happens early in the flare. These examples highlight that the underlying B_h behaviour around the RoPI can be systematic across different flare classes.

4.4.2 Statistical Trends Across 35 Flares

While the four example events illustrate good examples of magnetic field responses during individual flares, a broader perspective is needed to assess whether these behaviours are systematic. We therefore extend the analysis to the full sample of 35 flares, quantifying the properties of the step-like $B_{\rm h}$ changes. Figure 4.10 summarises the colour-coded time-lag maps for all events.

After examining all events in the colour-coded maps as shown in Figure 4.10, we visually identified 14 flares that exhibit a clear and strong concentration of increasing B_h along the RoPI. These are marked in Table 4.2 with "Y", with others marked "N". We note that some X-class flares – those with very complex and fragmentary RoPIs – do not show strong concentrations of increasing B_h, whereas many weaker flares do. Overall, events exhibiting coherent and systematic changes around the RoPI are in the minority. There are a further 6 events (nos. 1, 3, 5, 14, 29, 35) with small patches of $B_{\rm h}$-increasing only or $B_{\rm h}$-decreasing only located within the sunspot umbra or penumbra and also within the cumulative ribbon mask. As the strong, coherent field in these regions is not likely to be affected by random variations as much as in the network, these changes might also be related to the flare. An inspection of coronal imaging data to look for movement in the loops might help decide whether this is the case. In the remaining 15 events, regions of step-like $B_{\rm h}$ changes identified by the algorithm are distributed around the active region with mixed increasing and decreasing $B_{\rm h}$.

For each event, we calculated the average time lag $\bar{\tau}$ between the magnetic field change and the earliest UV ribbon brightening, and the maximum rate of change ($|dB_{\rm h}/dt|_{\rm max}$) for the $B_{\rm h}$-increasing and $B_{\rm h}$-decreasing separately. These are shown in Table 4.2, where the uncertainties represent the standard deviation of the measurements across all pixels belonging to each cluster

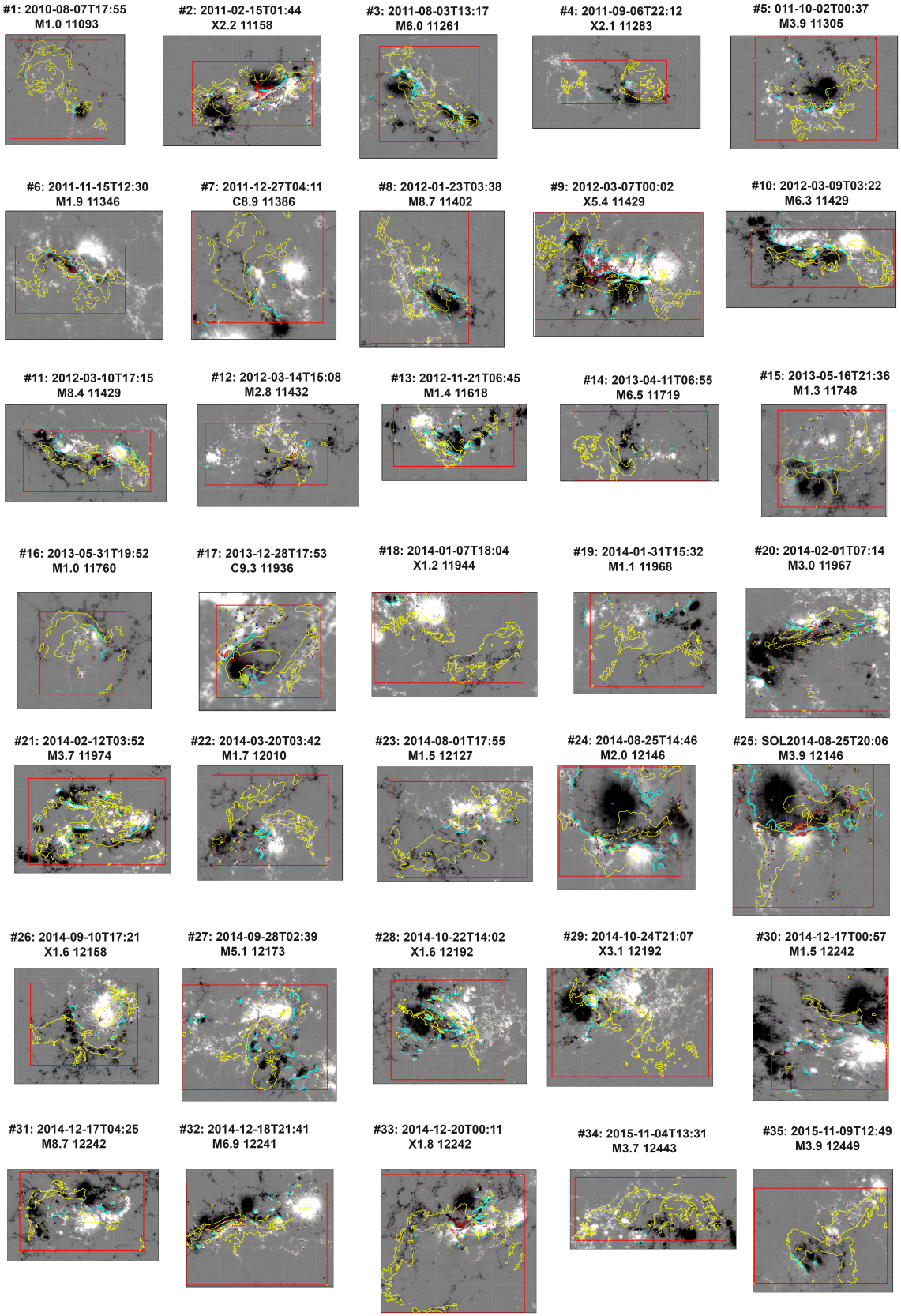

Figure 4.10: Colour-coded maps of the time lag τ for all 35 analysed flares. The time lag spans from –10 to +10 minutes. Pixels belonging to increasing clusters are shown using a red–blue colour scale, while decreasing clusters use a purple–green–yellow scale. Yellow contours mark the cumulative flare ribbons. The cyan outline indicates the RoPI, and the red box marks the selected region of interest. Each map is displayed over the corresponding B_r, where black and white represent negative and positive polarities, respectively.

Table 4.2: List of solar flares and key analysis parameters related to horizontal magnetic field evolution.

Flare No.	Start Time (UT)	Flare Class	AR	B_h @ PIL[a]	B_h-increasing cluster		B_h-decreasing cluster	
					$\bar{\tau}$ (min)	$\lvert dB_h/dt\rvert_{\max}$ ($\mathrm{G\,s^{-1}}$)	$\bar{\tau}$ (min)	$\lvert dB_h/dt\rvert_{\max}$ ($\mathrm{G\,s^{-1}}$)
1	SOL2010-08-07T17:55	M1.0	11093	N	$+6.54 \pm 21.45$	3.00 ± 0.27	$+4.15 \pm 20.37$	3.30 ± 0.29
2	**SOL2011-02-15T01:44**	**X2.2**	**11158**	Y	$+1.23 \pm 18.89$	6.85 ± 0.41	$+0.10 \pm 20.01$	2.95 ± 0.30
3	SOL2011-08-03T13:17	M6.0	11261	N	$+7.37 \pm 20.42$	18.43 ± 0.70	$+7.37 \pm 16.48$	10.00 ± 0.40
4	**SOL2011-09-06T22:12**	**X2.1**	**11283**	Y	$+3.95 \pm 10.27$	9.62 ± 0.79	$+3.30 \pm 18.59$	19.59 ± 0.81
5	SOL2011-10-02T00:37	M3.9	11305	N	-10.85 ± 20.65	3.83 ± 0.44	-2.15 ± 23.54	2.07 ± 0.32
6	SOL2011-11-15T12:30	M1.9	11346	Y	$+4.46 \pm 17.53$	1.85 ± 0.27	$+5.56 \pm 21.09$	1.49 ± 0.24
7	SOL2011-12-27T04:11	C8.9	11386	N	$+6.29 \pm 24.08$	2.83 ± 0.26	$+3.81 \pm 25.05$	1.70 ± 0.24
8	SOL2012-01-23T03:38	M8.7	11402	N	$+7.81 \pm 21.81$	1.98 ± 0.24	$+8.68 \pm 19.64$	2.33 ± 0.25
9	**SOL2012-03-07T00:02**	**X5.4**	**11429**	Y	$+4.94 \pm 15.50$	13.94 ± 0.61	$+8.90 \pm 17.38$	7.99 ± 0.31
10	SOL2012-03-09T03:22	M6.3	11429	Y	$+6.20 \pm 15.15$	5.83 ± 0.66	$+10.20 \pm 19.20$	6.30 ± 0.56
11	SOL2012-03-10T17:15	M8.4	11429	Y	$+7.24 \pm 18.00$	4.23 ± 0.30	$+4.59 \pm 18.59$	4.21 ± 0.30
12	SOL2012-03-14T15:08	M2.8	11432	Y	-5.80 ± 20.42	2.52 ± 0.26	-3.42 ± 21.64	4.48 ± 0.31
13	SOL2012-11-21T06:45	M1.4	11618	N	$+5.61 \pm 26.40$	5.70 ± 0.35	$+1.08 \pm 23.38$	1.93 ± 0.26
14	SOL2013-04-11T06:55	M6.5	11719	N	$+7.28 \pm 19.99$	2.56 ± 0.29	$+2.94 \pm 20.69$	3.24 ± 0.29
15	SOL2013-05-16T21:36	M1.3	11748	N	-6.80 ± 15.86	2.46 ± 0.27	-0.31 ± 18.08	2.24 ± 0.25
16	SOL2013-05-31T19:52	M1.0	11760	N	-7.05 ± 23.44	3.06 ± 0.39	-1.58 ± 25.71	3.29 ± 0.39
17	SOL2013-12-28T17:53	C9.3	11936	Y	$+2.05 \pm 20.49$	1.93 ± 0.27	-5.13 ± 20.92	1.86 ± 0.29
18	SOL2014-01-07T18:04	X1.2	11944	N	$+14.08 \pm 19.01$	13.57 ± 0.87	$+6.06 \pm 18.70$	12.59 ± 0.57
19	SOL2014-01-31T15:32	M1.1	11968	N	-5.51 ± 26.82	1.82 ± 0.23	$+2.94 \pm 25.92$	1.95 ± 0.24
20	SOL2014-02-01T07:14	M3.0	11967	Y	-3.05 ± 20.72	3.25 ± 0.39	-0.50 ± 24.16	7.36 ± 0.54
21	SOL2014-02-12T03:52	M3.7	11974	N	$+15.15 \pm 17.27$	3.36 ± 0.38	$+11.50 \pm 18.63$	5.00 ± 0.41
22	SOL2014-03-20T03:42	M1.7	12010	Y	$+4.61 \pm 19.78$	2.00 ± 0.26	$+9.61 \pm 25.11$	1.97 ± 0.28
23	SOL2014-08-01T17:55	M1.5	12127	N	$+7.18 \pm 24.28$	2.01 ± 0.26	$+1.59 \pm 22.48$	2.31 ± 0.28
24	SOL2014-08-25T14:46	M2.0	12146	N	$+8.84 \pm 21.31$	2.88 ± 0.30	$+8.80 \pm 22.34$	2.76 ± 0.29
25	**SOL2014-08-25T20:06**	**M3.9**	**12146**	Y	$+4.49 \pm 19.13$	3.72 ± 0.30	$+6.39 \pm 22.70$	2.96 ± 0.31
26	SOL2014-09-10T17:21	X1.6	12158	Y	$+8.61 \pm 17.58$	13.69 ± 0.54	$+2.39 \pm 16.83$	4.60 ± 0.32
27	SOL2014-09-28T02:39	M5.1	12173	N	-2.72 ± 19.79	3.90 ± 0.32	$+8.97 \pm 24.11$	11.34 ± 0.72
28	SOL2014-10-22T14:02	X1.6	12192	N	$+1.54 \pm 17.89$	16.9 ± 0.49	$+7.54 \pm 20.19$	13.19 ± 0.53
29	SOL2014-10-24T21:07	X3.1	12192	N	$+7.22 \pm 13.99$	14.77 ± 1.50	$+11.06 \pm 18.50$	10.22 ± 0.53
30	SOL2014-12-17T00:57	M1.5	12242	N	$+5.35 \pm 24.54$	3.55 ± 0.30	-5.58 ± 20.81	1.86 ± 0.24
31	SOL2014-12-17T04:25	M8.7	12242	N	$+10.34 \pm 22.30$	2.69 ± 0.26	$+7.84 \pm 18.64$	3.15 ± 0.27
32	SOL2014-12-18T21:41	M6.9	12241	Y	$+0.39 \pm 20.26$	6.37 ± 0.31	$+3.19 \pm 21.45$	2.62 ± 0.29
33	SOL2014-12-20T00:11	X1.8	12242	Y	$+3.24 \pm 16.19$	5.36 ± 0.33	$+4.29 \pm 22.42$	4.57 ± 0.30
34	SOL2015-11-04T13:31	M3.7	12443	N	$+2.10 \pm 20.66$	3.33 ± 0.34	-0.64 ± 22.81	3.99 ± 0.36
35	SOL2015-11-09T12:49	M3.9	12449	N	$+10.72 \pm 17.46$	3.99 ± 0.28	$+10.22 \pm 19.88$	1.86 ± 0.27

Note. [a] Indicates whether a clear pattern of increase of B_h around the polarity inversion line (PIL) is observed. "Y" ("N") denotes yes (no). The flares shown in **bold** correspond to the example events discussed in Section 4.4.1.

4.4.2.1 Distribution of Average Time Lags Across Flare Classes

Figure 4.11 summarises the statistical distribution of average time lags $\bar{\tau}$ between the horizontal field changes and the first flare ribbon brightening, separated by flare class. Panels (a–c) show the results for X-, M-, and C-class flares, respectively, with distributions split according to increasing or decreasing B_h behaviour. For the X-class events (panel a), we found primarily positive average delays (time of maximum field change lags the first ribbon appearance) of $\bar{\tau} \sim 0$–10 min in both increasing and decreasing clusters. The M-class flares (panel b) show a broader distribution of delays, including cases where the time of maximum field change precedes the first ribbon appearance by a few minutes. We return to this below. There are insufficient C-class events to draw any conclusion about their behaviour. The behaviour of the X and M-class flares is broadly consistent with earlier timing studies: Johnstone et al. (2012) found that in four X-class flares the onset

of UV emission typically preceded the photospheric field change by 4–9 minutes. However, Johnstone et al. (2012) used the estimated onset time of the field change, which will be typically a few minutes earlier than the time of maximum $|\frac{\mathrm{d}B_\mathrm{h}}{\mathrm{d}t}|$ that we use. Thus, the delay magnitudes are comparable, but the timing definitions differ. Allowing for the delay between the onset time of the field change and the time of maximum field change, we find some lags which are consistent with those found by Johnstone et al. (2012), but in locations very close to the RoPI lags are considerably shorter. It is possible that pixels sampled by Johnstone et al. (2012) tended to be farther from the RoPI.

To test whether the $\bar{\tau}$ distributions differ between flare classes, we applied a two-sample Kolmogorov–Smirnov (K–S) test to all combinations of X-, M- and C-class flares (Kolmogorov, 1933; Smirnov, 1948). For the increasing B_h behaviour, the K–S test returned p-values of 0.45 (X vs M), 0.98 (X vs C), and 0.86 (M vs C). For the decreasing B_h behaviour, p-values were 0.61, 0.44, and 0.52 for the same class comparisons. A p-value of < 0.05 is required to demonstrate a statistically significant difference, therefore, within our sample of 35 events, the $\bar{\tau}$ distributions do not show a dependence on flare class.

We recalculated the distributions of average time lags, restricting the analysis to the subset of the 14 clear B_h-pattern flares only (Figure 4.12). The resulting distributions show that the M-class flares with well-defined increases in B_h near the PIL tend to exhibit shorter time lags compared to all M-class flares, and most of the negative values of $\bar{\tau}$ disappear. Negative $\bar{\tau}$ values are therefore likely due to normal active region behaviour and not related to the flare. This is also suggested by the widespread spatial distribution of the step-like changes identified in such flares.

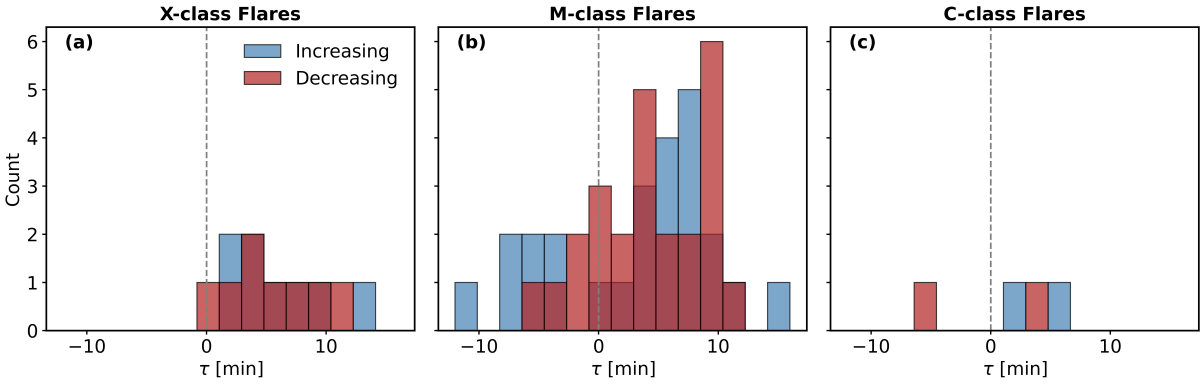

Figure 4.11: Distributions of average time lags ($\bar{\tau}$) between the peak of the horizontal field change rate and the corresponding early UV ribbon brightening for flares data set where: (a) X-class, (b) M-class, and (c) C-class. Blue and red bars represent the clusters associated with increasing and decreasing horizontal magnetic field ($B_{\rm h}$), respectively.

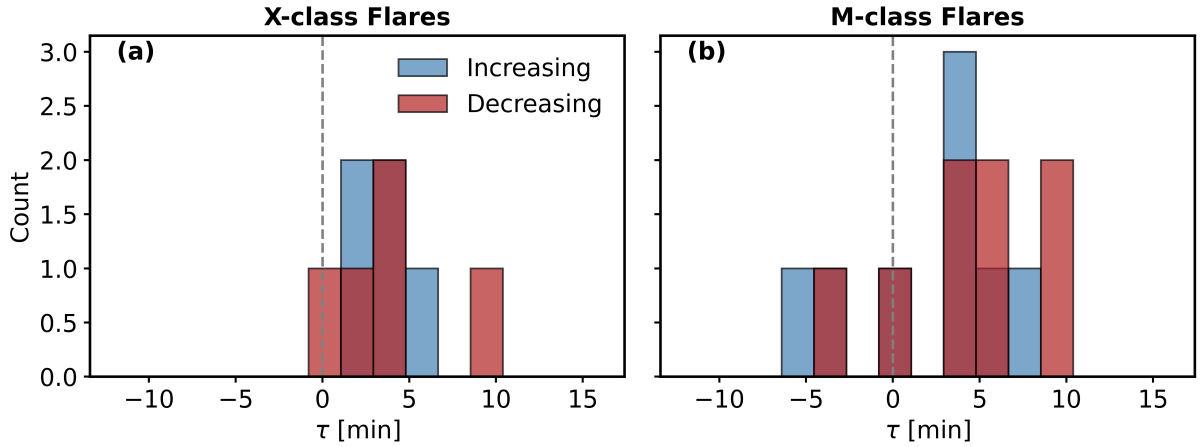

Figure 4.12: Distributions of time lags ($\bar{\tau}$) between the peak of the horizontal field change rate and the corresponding early UV ribbon brightening for flares that exhibit a clear increase in B_h along the PIL. Blue and red bars represent the clusters associated with increasing and decreasing horizontal magnetic field ($B_{\rm h}$), respectively.

4.4.2.2 Correlation Between the Number of Pixels exhibiting step-like changes and the Maximum Rate of Change

Investigating whether regions with larger spatial flare restructuring exhibit stronger magnetic field changes, we examined the relationship between the number of pixels that have step-like horizontal field changes and the mean of the maximum rate of change ($|dB_\mathrm{h}/dt|_\mathrm{max}$). Figure 4.13 shows the scatter plots for the increasing and decreasing clusters, together with their best-fit trend lines. Additionally, the scatter plots separate the flares based on whether a clear B_h increase is observed in the area of the polarity inversion line, with squares indicating events for which such an increase is observed and circles indicating those for which it is not. Separate linear fits are performed for the two groups in each panel. For the increasing B_h clusters, both $B_\mathrm{h}@\mathrm{PIL} = Y$ and N events show a moderate positive correlation between the number of pixels and $|dB_\mathrm{h}/dt|_\mathrm{max}$, with a weaker correlation for events with a clear B_h increase around PIL (cc = 0.35) compared to the $B_\mathrm{h}@\mathrm{PIL} = N$ cases (cc = 0.65). A similar behaviour is found for the decreasing clusters, where the correlations remain positive for both groups, with correlation coefficients of cc = 0.40 for $B_\mathrm{h}@\mathrm{PIL} = Y$ and cc = 0.65 for $B_\mathrm{h}@\mathrm{PIL} = N$. The scatter plots indicate that events with higher maximum rates of B_h increase are preferentially associated with X-flares, and have larger regions of step-like changes overall, regardless of whether the flare exhibits a clear increase in B_h along the PIL. This tendency for an association of high rates of increase with flare size is not so clear in the B_h-decreasing regions.

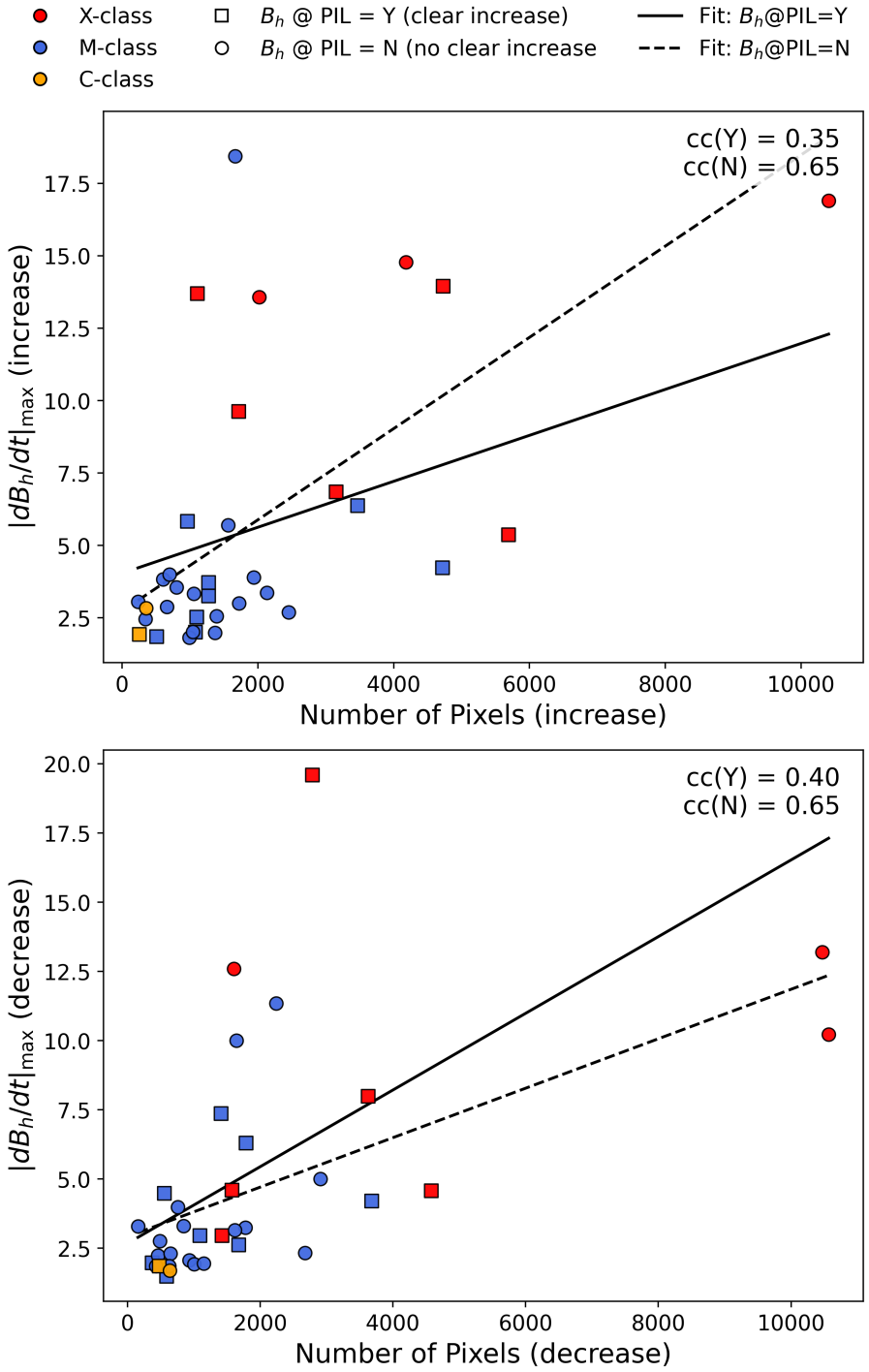

Figure 4.13: Scatter plots of cluster size (number of pixels showing a step-like change) and the maximum rate of change of the horizontal magnetic field ($|dB_h/dt|_{\max}$) for increasing (top) and decreasing (bottom) clusters. Colours denote the GOES class, while marker shapes indicate the presence (squares) or absence (circles) of a clear B_h increase around the PIL. Solid and dashed lines represent linear fits for B_h@PIL $= Y$ and N, respectively, with corresponding Pearson correlation coefficients (cc) shown in each panel.

4.5 Discussion

Our study investigates the spatial and temporal evolution of the horizontal magnetic field during 35 solar flares, emphasising its relationship to the initial flare ribbon brightening in regions surrounding the polarity inversion line. The primary finding is the spatial and temporal relationships in some flares between the changes of the horizontal field and the time of first ribbon appearance. In 14 out of 35 flares examined, there are concentrations of regions of stepwise increase in B_{h} near the region of polarity inversion. Examples of these are shown in Figures 4.6–4.9. In these events, the peaks in the rate of change of the horizontal magnetic field generally lag the onset of UV ribbon brightening by up to a few minutes, showing an increasing time lag with increasing distance from the PIL. The horizontal field increases near the RoPI are consistent with previous observations that found rapid, permanent changes in B_{h} near the PIL during major flares (e.g. Wang and Liu, 2010; Wang et al., 2012; Sun et al., 2017; Petrie and Sudol, 2010; Liu et al., 2018; Yadav and Kazachenko, 2022). However, in the other 21 events the stepwise increases in B_{h} are scattered through the region and are not clearly related to the flare. There is no evidence for dependence of the $\bar{\tau}$ distributions on flare class within our sample.

In the four cases examined in detail, increases in B_{h} near the RoPI are accompanied by decreases in B_{h} more distant from the RoPI, including located within nearby penumbra. These changes imply that the field becomes more locally horizontal in some locations and more vertical in others. An additional point of interest from the case studies shown is that pixels with the largest $|dB_h/dt|_{\mathrm{max}}$ values are typically concentrated in the regions exhibiting the shortest time lags. We found a moderate positive correlation between the number of pixels exhibiting step-like horizontal field changes and the mean of the maximum rate of change $|dB_h/dt|_{\mathrm{max}}$ (Figure 4.13). This trend suggests that a larger flare-driven reconfigur-

ation may be associated with a stronger average photospheric response. Similar behaviour has been reported in a previous study of 6 large flares by Petrie (2012), who found that the more energetic flares tended to have somewhat more extensive and stronger horizontal field enhancements near the polarity inversion line.

In the subset of 14 events, the spatial progression of time lag between $\boldsymbol{B}_{\mathrm{h}}$ increase and the early UV emission, which increases systematically with distance from the RoPI, provides strong evidence that the increase of $\boldsymbol{B}_{\mathrm{h}}$ is linked to coronal implosion, in the sense of magnetic field contracting downward as stored magnetic energy is released. The disturbance to the field due to reconnection propagates outward, with the field rooted closest to the RoPI responding first, and more distant footpoints adjusting later. This was also found in a theoretical study by Barczynski et al. (2019) who used a 3D magnetohydrodynamic simulation to show increases in $\boldsymbol{B}_{\mathrm{h}}$ that progress away from the PIL, mainly as the result of the reconnection-driven contraction of sheared flare loops. As is observed in two of the case studies we show, in the Barczynski et al. (2019) simulation the region of $\boldsymbol{B}_{\mathrm{h}}$ increase is not symmetric around the PIL. We also note that within the systematic pattern of increasing timelags around the RoPI there are also small patches with similar timelags, which might point to patchy reconnection in the corona. Yadav and Kazachenko (2022) proposed that the inner, newly reconnected loops contract because of a magnetic implosion or a velocity disturbance (as modelled by Sarkar et al., 2017), whereas the vertical component of outer loops rooted within the flare ribbons may increase due to the overall rearrangement of post-reconnection fields. We also see some evidence of this in the (more widespread and typically less coherent) $\boldsymbol{B}_{\mathrm{h}}$-decreasing clusters.

We interpret the observed time lags as the combination of two physically distinct timescales, as illustrated in Figure 4.14. The first corresponds to the time, compared to the earliest reconnection, at which reconnection occurs on a given coronal field line (t_r). We do not know when reconnection starts, but the appearance time of the first UV ribbons,

which is the baseline against which we measure the timelag, can be taken as a proxy. The second corresponds to a propagation timescale ($\tau_{\rm prop}$), required for the resulting coronal field line 'bending' to transfer downward to the photosphere, where the step-like change in $B_{\rm h}$ is observed.

In Figure 4.14, panel a) reconnection starts at $t_{r,0}$, and for the locations exhibiting the earliest increases in $B_{\rm h}$ (mostly close to the RoPI) the timescale τ_0 on which the $B_{\rm h}$ increase is observed will be dominated by the propagation of the signal from the coronal reconnection site to the photosphere. In panel b) for pixels located farther from the RoPI, reconnection occurs later, and on longer and higher coronal loops. The measured time lag therefore reflects both the later reconnection time and an increased propagation time, $\tau_1 = t_{r,1} - t_{r,0} + \tau_{\rm prop,1} \sim t_{r,1} + \tau_{\rm prop,1}$ if we set $t_{r,0} = 0$ defining the start of reconnection. So the colour-coded time lag maps act as a combined diagnostic of the progress of reconnection and the subsequent downward magnetic stresses.

If we assume that signal propagates, as a 'bend' in the field, at the Alfvén speed, then it is likely that the coronal propagation timescale will be relatively short compared to the timescale of propagation through the chromosphere to the photosphere: although the distance that the signal must propagate through the chromosphere is smaller, and the chromospheric field higher than the coronal values, the density increases in the chromosphere by orders of magnitude, lowering the Alfvén speed. Modeling by Russell and Fletcher (2013) with a realistic chromosphere found a propagation timescale of around 1 minute. This timescale is similar to the 1-2 minutes time lags that we measure between the first appearance of the ribbons - which we might take as indicating the start of coronal reconnection - and the first measured increases in $|dB_h/dt|_{\rm max}$.

Later on, the propagation time through the corona and chromosphere would increase as the reconnection site rises, particularly if the magnetic field strength decreases with distance from the PIL. This would contribute to the increasing time lags, and would have to be corrected for (e.g. with loop length and coronal field-strength estimates, from modeling and observation) before the time evolution of the reconnection could be separated. This is beyond the scope of the current work, but may be a useful avenue for future study.

While most pixels exhibit positive time lags, a fraction of locations show negative lags, where the maximum rate of change in $\boldsymbol{B}_{\mathrm{h}}$ precedes the detected onset of ribbon brightening. Within the framework described above, this may occur if early coronal restructuring begins before chromospheric heating becomes sufficiently strong to produce detectable 1600 Å emission. These negative time lags are more common in the $\boldsymbol{B}_{\mathrm{h}}$ decreasing cluster (see Figure 4.11) and in such cases could be associated with coronal field expanding outwards as part of a magnetic flux rope starts to rise before the flare onset. But as seen in the maps our algorithm also detects step-like changes in very scattered pixels, including in weak-field regions, which are not necessarily all flare related. Instead these are likely to be small-scale fluctuations of the background field. Particularly in weaker M-flares with less well-ordered magnetic field changes near the RoPI, these small-scale changes could be dominating the calculation of the average time lags, which is sometimes negative and sometimes positive.

4.6 Conclusions

We have investigated the evolution of the horizontal magnetic field ($\boldsymbol{B}_{\mathrm{h}}$) during 35 solar flares of X-, M-, and C-classes, using a machine-learning approach to identify regions of step-like changes, and focusing on their spatial and temporal relationship with the onset of UV ribbon brightening. The main conclusions of this work are as follows:

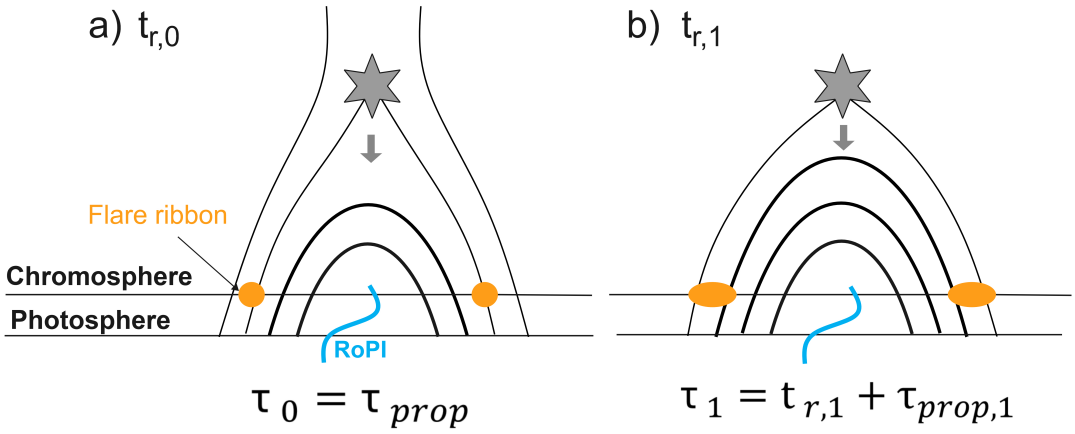

Figure 4.14: Schematic illustration of the proposed interpretation of the time lag between horizontal magnetic field changes and early flare ribbon brightening. (a) For field lines reconnecting early and close to the RoPI, the measured time lag is dominated by the downward propagation time of the coronal magnetic restructuring. (b) For field lines reconnecting later and farther from the RoPI, the measured time lag includes both the reconnection time and the propagation time. Orange bands denote flare ribbons and the blue curve marks the RoPI.

1. In 14 of the 35 flares analysed, we identify spatially localised concentrations of stepwise increases in B_h in regions surrounding the polarity inversion line. Decreases in the B_h appear more spatially scattered across the active region, extending into the penumbral areas.
2. The peaks in the rate of change of the horizontal magnetic field ($|dB_\mathrm{h}/dt|$), identifying the times at which the field is changing most rapidly, generally lag the earliest appearance of UV ribbon brightening by several minutes.
3. A systematic spatial progression was identified in these 14 flares, where the time lag τ increases with distance from the RoPI. This suggests that the magnetic restructuring propagates outward from the initial reconnection site, consistent with progressive coronal reconnection leads to a sequence of retracting coronal loops ("core implosion") driving a downward magnetic response in the photosphere.

4. In these events, we interpret the observed time lags as the combined effect of two timescales: the timing of reconnection on progressively higher and longer coronal loops and the subsequent downward propagation of magnetic stresses to the photosphere. The shortest time lags identified in the data are comparable to modelled Alfvén wave propagation times through the chromosphere.
5. In the majority of events, clearly flare-related step-like changes in B_{h} are not detected by our method, or are very subtle (small clusters in umbra or penumbra.)
6. A moderate positive correlation is identified between the number of pixels showing step-like horizontal magnetic field changes and the mean value of the maximum rate of change $|dB_h/dt|_{\max}$.
7. a two-sample Kolmogorov–Smirnov test applied to the average time lag ($\bar{\tau}$) distributions across different flare classes reveals no statistically significant dependence of the lag on flare class.
8. The number of pixels showing step-like B_{h} changes correlates positively with the mean maximum rate of change ($|dB_h/dt|_{\max}$). This demonstrates that larger areas of photospheric restructuring tend to have stronger magnetic evolution.

In summary, our analysis shows that, for a substantial minority of flares, the time lag between the horizontal magnetic field changes and the onset of UV emission increases systematically with distance from the polarity inversion line. The measured time lags likely reflect a combination of reconnection timing and the downward propagation of magnetic stresses through the solar atmosphere. Future studies employing higher cadence vector magnetic field observations and multi-wavelength diagnostics will help understand the timing of magnetic field changes and their relationship to flare energy release.

Chapter 5

Temporal Relationship Between Photospheric Magnetic Field Changes and Coronal Energy Release

5.1 Introduction

In chapter 4, we investigated the systematic evolution of the horizontal magnetic field, B_h, around the magnetic polarity inversion line (PIL) during solar flares by analysing its temporal and spatial correspondence with chromospheric flare ribbons observed in ultraviolet emission. That analysis established a clear link between photospheric magnetic changes and the chromosphere. However, the fundamental driver of the flare process exists in the corona, where magnetic free energy is rapidly released through magnetic reconnection (Carmichael, 1964; Sturrock, 1966; Hirayama, 1974; Kopp and Pneuman, 1976). This motivates investigating the temporal-spatial relationship between coronal energy release and the evolution of the horizontal magnetic field in the photosphere.

Several observational studies have examined the relationship between coronal energy release and changes in the photosphere. For example, Burtseva et al., 2015 reported that rapid magnetic flux changes in the photosphere occur nearly simultaneously with hard X-ray (HXR) bursts, which are widely interpreted as signatures of coronal magnetic reconnection, suggesting that the photospheric field responds dynamically to reconnection-driven energy release. Similarly, Castellanos Durán et al., 2018 found that the peak GOES soft X-ray flux is well correlated with the total signed and unsigned photospheric magnetic flux changes, indicating that stronger flares tend to produce larger magnetic changes. However, these studies established temporal associations or flare-integrated scaling and did not determine how this relationship evolves spatially.

The primary objective of this chapter is to examine the temporal-spatial relationship between coronal energy release and the evolution of the horizontal magnetic field in the photosphere. The time derivative of the GOES 1–8 Å soft X-ray flux is used as a proxy for the coronal energy-release, enabling the identification of impulsive episodes during flare evolution. We investigate whether these episodes correspond to the occurrence of step-like changes in B_h. This analysis provides an observational test of the coronal implosion scenario (Hudson, 2000), which predicts that magnetic energy release in the corona leads to a contraction of the coronal field and a corresponding change of the photospheric field.

This chapter is organised as follows. Section 5.2 describes the event selection criteria and outlines the methodology, including the use of the GOES soft X-ray derivative as a proxy for coronal energy release and the identification of individual energy release episodes. Section 5.3 presents the results, beginning with a detailed case study of the 2012 March 7 X5.4 flare and followed by a multi-event comparison of the temporal and spatial association between coronal energy release and photospheric magnetic field changes. The implications of these findings are discussed in Section 5.4, and the main conclusions are summarised in Section 5.5.

5.2 Methodology

5.2.1 Event Selection

A subset of six solar flares from the events studied in Chapter 4 was selected for this study based on the statistical properties of the photospheric magnetic field response. Specifically, X-class and M-class events exhibit well-defined and coherent histograms of the magnetic field change times, t_B, defined as the times of peak $|dB_h/dt|$, with clear and identifiable peaks. These pronounced peaks enable a clear determination of the characteristic timing of step-like changes in the horizontal magnetic field. In contrast, when applying the same analysis to M-class flares, the resulting t_B histograms were found to be significantly noisier, lacking a clear dominant peak, which restrict reliable temporal comparisons and introduces ambiguity in identifying a representative magnetic field response time. To ensure consistency and statistical accuracy in the temporal analysis, we restricted the sample to six flares. Table 5.1 lists the flare events analysed in this chapter, together with their start times, associated NOAA active regions, and GOES classifications.

Table 5.1: List of analysed solar flares used in this chapter.

Flare Date	Start Time (UT)	NOAA AR	GOES Class
2011-02-15	01:44	11158	X2.2
2011-09-06	22:12	11283	X2.1
2012-03-07	00:02	11429	X5.4
2014-08-25	20:06	12146	M3.9
2014-12-18	21:41	12241	M6.9
2014-12-20	00:11	12242	X1.8

5.2.2 GOES Soft X-ray Derivative as a Proxy for Coronal Energy Release

To identify the coronal energy release times we employed the derivative of the GOES 1–8 Å soft X-ray flux, dF_{1-8}/dt, as a proxy for the coronal energy release during each flare (e.g., Neupert, 1968;Dennis and Zarro, 1993;Veronig et al., 2002a). This approach is motivated by the Neupert effect, which establishes that the time integral of the hard X-ray (HXR) emission closely reproduces the soft X-ray (SXR) light curve multiplied by a constant factor. Thus, the time derivative of the SXR flux approximates the shape of HXR temporal profile. Since HXR emission directly traces the precipitation of nonthermal electrons accelerated during magnetic reconnection and since those electrons embody a large fraction of the flare energy released (e.g. Emslie et al., 2012), it provides a measure of the coronal energy release. Ideally, the impulsive-phase energy release would be directly quantified using HXR observations; however, such data are not available for all events in our sample (e.g., incomplete coverage in the RHESSI database). Therefore, the SXR derivative is adopted as a consistent proxy across all flares analysed here. Consequently, the SXR derivative serves as an observationally supported proxy for the coronal energy release.

5.2.3 Identification of Coronal Energy-Release Episodes from the GOES Soft X-ray Derivative

To determine individual impulsive episodes in the coronal energy release, we analysed fluctuations in the GOES 1–8 Å soft X-ray derivative. Throughout this chapter, we refer to distinct peaks in the GOES derivative as *coronal energy release episodes*. To begin with, the GOES flux was smoothed using a 24 s running mean in order to remove high-frequency instrumental noise while preserving short-timescale impulsive variability. This choice is motivated by the results of Simões et al., 2015, who demonstrated that soft X-ray

pulsations typically have characteristic timescales in the range of approximately 8–112 s. Therefore, the smoothing suppresses episodes shorter than physically relevant timescales while retaining the impulsive-phase variability associated with energy release. Next, the time derivative of the smoothed flux was computed to identify impulsive signatures. Finally, coronal energy release episodes, denoted as t_{GOES}, were identified as local maxima in the derivative time series using the SciPy `find_peaks` algorithm under the following criteria:

- The background noise level was estimated from a pre-flare quiet interval preceding the impulsive phase, and the threshold was equal to two standard deviation of this noise level.
- A minimum temporal separation of 60 s between successive peaks was applied to avoid over-segmentation and to ensure that each detected fluctuation represents a different impulsive energy release episode.
- To ensure association with flare processes, the GOES soft X-ray derivative period was restricted to the flaring GOES period.

These steps provide a definable set of physically meaningful coronal energy release episodes suitable for comparison with the timing of photospheric magnetic field changes.

5.2.3.1 Temporal–Spatial Association Map Construction

The primary goal of this chapter is to link high-resolution spatial information on photospheric horizontal magnetic field changes with temporally resolved signatures of coronal energy release that lack spatial information. To achieve this, we introduce a novel temporal association approach that combines horizontal magnetic field measurements from *SDO*/HMI with the high-cadence (~ 2 s) *GOES* soft X-ray observations. For each flare in the analysed sample, every pixel exhibiting a significant step-like change in the horizontal magnetic field is identified, and its mid-step time t_B (the steps for calculating t_B are explained in detail in the previous chapter in Section 4.3.4) is associated with the

nearest coronal fluctuation time $t_{\mathrm{GOES},i}$ derived from the *GOES* soft X-ray derivative time series. This association assigns a discrete fluctuation index i to each pixel, indicating which impulsive coronal energy-release episode is most closely related in time to the observed photospheric magnetic field change.

The following section presents the results obtained by applying the temporal association method to the six flares analysed in this chapter. The results are organised into two parts, addressing the temporal behaviour of magnetic field change times relative to the GOES soft X-ray derivative and the corresponding spatial patterns revealed by fluctuation-index maps.

5.3 Results

In this section, we present the results obtained by applying the temporal association framework described above. First, we examine a representative event in detail to illustrate the temporal and spatial relationship between the horizontal magnetic field change and the coronal energy release. Then, we compare these findings with the remaining events to assess the consistency of the observed behaviour across the sample.

5.3.1 Case Study: 2012 March 7 X5.4 Flare (NOAA AR 11429)

This flare is the most energetic event in the analysed sample (Table 5.1). This event exhibits a well-defined impulsive phase in the GOES soft X-ray derivative, characterised by clear coronal energy release episodes. Furthermore, as demonstrated in the previous chapter (Figure 4.7), the horizontal magnetic field evolution displays a coherent spatial organisation. Due to these characteristics, this flare provides an ideal example for illustrating the temporal-spatial association between coronal energy release and photospheric magnetic field changes.

5.3.1.1 Temporal Behaviour of the Coronal Energy Release Relative to Photospheric Magnetic Field

We begin by examining the time derivative of the GOES 1–8 Å soft X-ray flux, dF_{1-8}/dt. Figure 5.1 (a) illustrates the temporal structure of the GOES derivative for the X5.4 flare. Two notable peaks are identified within the impulsive phase. The first peak continues for approximately 7 minutes and reaches an amplitude of $dF_{1-8}/dt \sim 0.8 \times 10^{-6}$ $\mathrm{W\,m^{-2}\,s^{-1}}$. This is followed by a second, stronger peak lasting roughly 16 minutes, with a maximum amplitude of $dF_{1-8}/dt \sim 1.75 \times 10^{-6}$ $\mathrm{W\,m^{-2}\,s^{-1}}$, marking the dominant phase of energy release.

Figure 5.1 (b) presents the histogram of the magnetic field change times, t_B. The distribution exhibits clear peaks that coincide temporally with the major peaks in the GOES derivative. Both increasing and decreasing step-like changes in the horizontal magnetic field show peaks at the first and second GOES maxima; however, the slightly higher peak for the increasing changes occurs at the first GOES peak. In both clusters, the number of pixels increases sharply during the flare's impulsive phase. The gaps in the distributions

correspond to intervals in which no pixels reached their maximum rate of change. Overall, the temporal comparison indicates that the photospheric magnetic field response is closely associated with the coronal energy release, with the majority of magnetic field changes occurring during the flare's GOES window.

5.3.1.2 Temporal–Spatial Association Map

In this section, we examine the corresponding spatial organisation of these temporally associated magnetic field changes. For this case of X5.4 flare, a total of 22 significant coronal energy release episodes were detected during the flaring interval using the criteria described in Section 5.2.3. The detailed structure of the derivative is shown in Figure 5.2a. Figure 5.2b presents the temporal–spatial association map, which displays the spatial distribution of pixels whose magnetic field changes are assigned to specific coronal energy release episodes. Each coloured pixel is linked to the nearest fluctuation index i in time. Then, the temporal association is encoded within a two-dimensional spatial representation.

The map reveals a clear coherent pattern. The earliest episodes during the first peak in the derivative are concentrated along the magnetic polarity inversion line (PIL). As the flare progresses, later episodes extend progressively away from the PIL, forming expanding and coherent structures across the active region. In addition to this overall progression, several localised coherent patches are present in regions of strong magnetic field, which may indicate structure in the coronal reconnection region. In contrast, when the derivative becomes negative, the spatial distribution of detected changes becomes more widespread and less organised, with many pixels appearing randomly distributed, likely reflecting noise or weaker, less coherent magnetic responses.

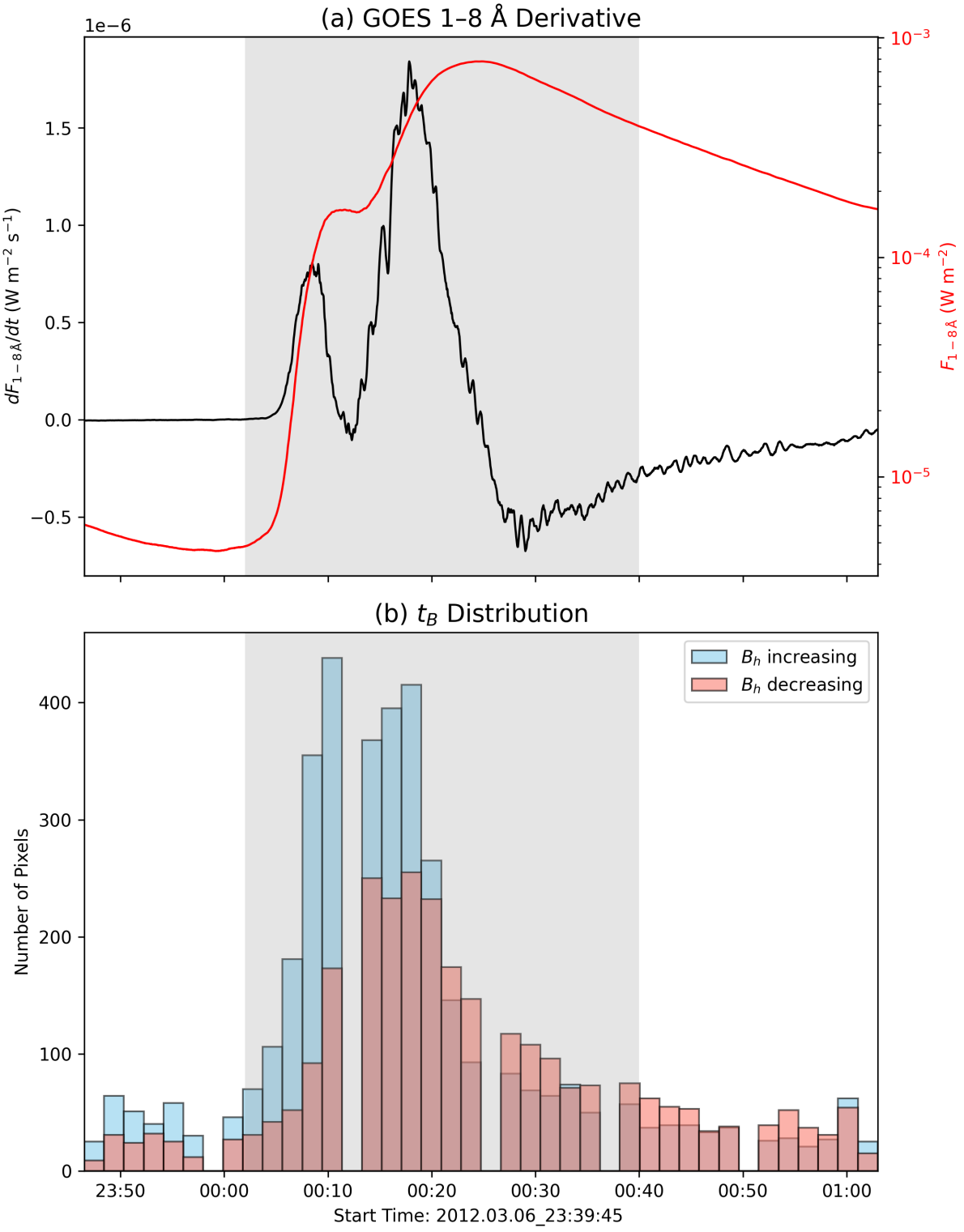

Figure 5.1: (a) Time derivative of the GOES 1–8 Å soft X-ray flux of X5.4 flare on 2012 March 7. The black curve shows dF_{1-8}/dt, while the red curve is the GOES 1–8 Å soft X-ray flux. The shaded region marks the flare GOES window interval between 00:02 UT and 00:40 UT. (b) Distribution of t_B, defined as the time of peak $|dB_h/dt|$, for pixels exhibiting step-like changes in the horizontal magnetic field. Blue and red histograms correspond to pixels with increasing and decreasing B_h, respectively.

In summary, the temporal and spatial analyses of the 2012 March 7 X5.4 flare reveal a highly organised photospheric response to impulsive coronal energy release. The concentration of t_B within the dominant impulsive phase, combined with the coherent spatial progression of the fluctuation from the polarity inversion line outward, indicates that the magnetic field changing is systematically linked to coronal energy-release episodes. After illustrating this behaviour in a representative and energetically extreme event, we now examine whether a similar temporal-spatial organisation is observed across the remaining flares in the sample.

5.3.2 Multi-Event Comparison of Temporal–Spatial Coronal Association

Now we extend the same analysis to the full flares list (Table 5.1) to assess the consistency of the observed behaviour. This multi-event comparison examines whether the temporal alignment between t_B and the GOES soft X-ray derivative, as well as the systematic spatial structure associated with the coronal energy release, represents systematic features across different flares rather than properties of a single case.

5.3.2.1 Temporal Behaviour During Coronal Energy Release

As defined earlier, the time derivative of the GOES soft X-ray flux is used as a proxy for discrete episodes of coronal energy release. Here, we apply the same fluctuation-identification procedure (Section 5.2.3) to all flares in the sample and examine the temporal relationship between the coronal energy-release episodes and the photospheric mag-

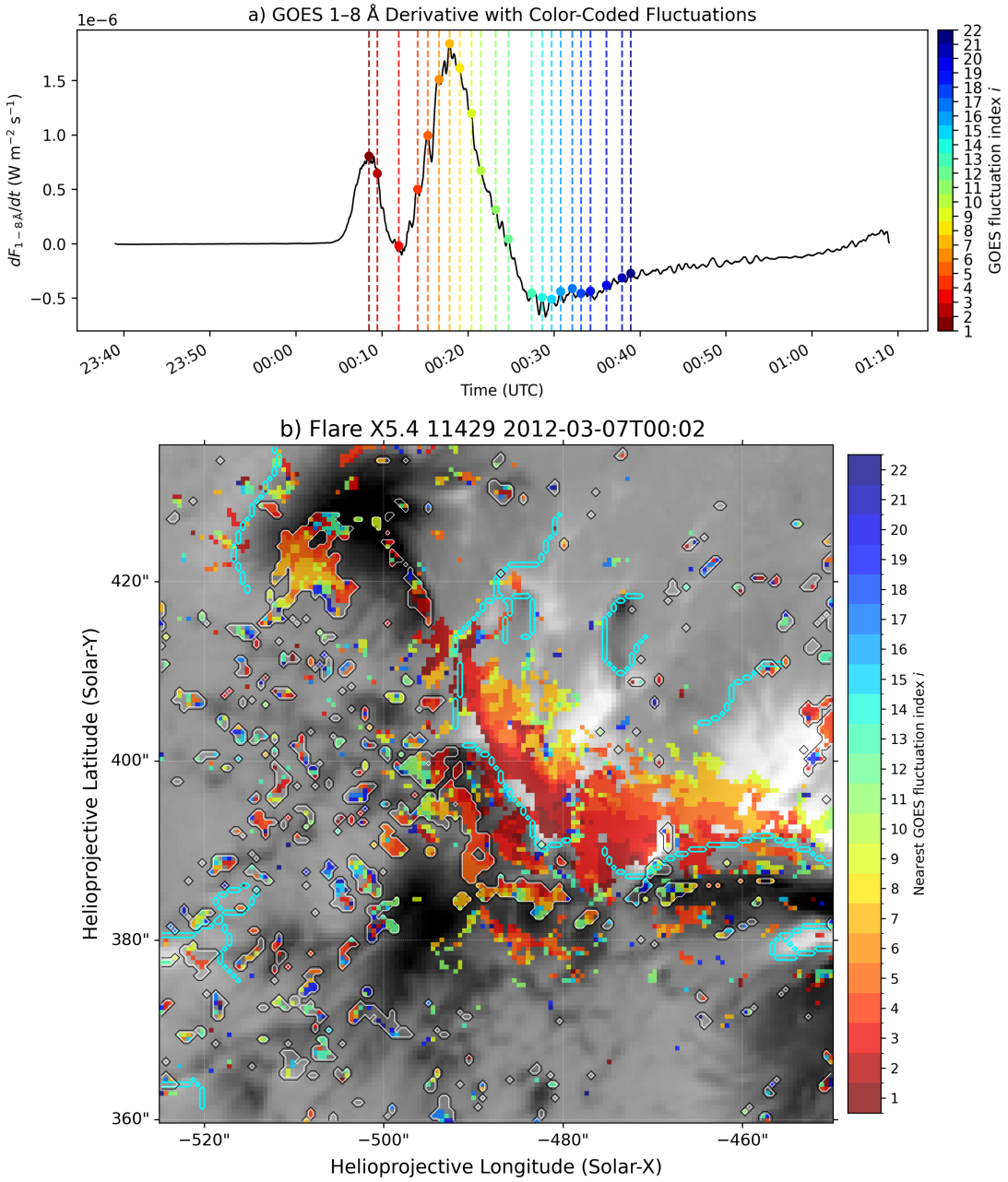

Figure 5.2: (a) Time derivative of the GOES 1–8 Å soft X-ray flux, $dF_{1\text{–}8}/dt$, of X5.4 flare on 2012 March 7. Coloured dashed vertical lines mark the local maxima identified by the peak-detection algorithm described in Section 5.2.3. (b) Fluctuation association map showing the spatial distribution of pixels whose magnetic-field changes are temporally associated with specific GOES derivative episodes. Each coloured pixel is assigned to the nearest fluctuation index i in time. Pixels with a decreasing magnetic field are contoured in black and white. The cyan contours indicate the locations of RoPI. The background image shows the B_r.

netic field response. Figures 5.3 and 5.4 display, for each flare, GOES 1–8 Å flux (F_{1-8}) and the GOES 1–8 Å derivative restricted to the GOES-defined flaring interval, overplotted with the histograms of t_B, the times of maximum $|dB_h/dt|$ for pixels exhibiting step-like changes in the horizontal magnetic field.

Across all six events, the dominant peaks in the t_B histograms are concentrated within the impulsive phase and coincide temporally or are close to the strongest peaks in the GOES derivative. This indicates that intervals of enhanced coronal energy release are systematically accompanied by an increased number of pixels undergoing rapid horizontal magnetic field changes. Although the amplitude and number of episodes differ between flares, this temporal correspondence is consistently observed.

No clear systematic difference is observed between the increasing and decreasing B_h clusters across the sample, although individual events (e.g. the X5.4 flare) reach their maximum response slightly earlier within the impulsive interval, whereas pixels belonging to the decreasing cluster tend to align more closely with the strongest GOES derivative peak. Despite variations in complexity, where the number of detected GOES episodes ranges from 5 to 31 (Table 5.2), all flares exhibit clustered, high-amplitude derivative peaks during the impulsive phase. The presence of this pattern across events of different classes indicates that the temporal confinement of photospheric magnetic field changes to coronal energy-release intervals is a systematic property.

Additional temporal properties of the coronal energy-release episodes are summarised in Table 5.2. For each flare, we compute the characteristic time lag between t_B defined as the time of maximum $|dB_h/dt|$ for pixels exhibiting step-like changes in the horizontal magnetic field and the dominant peak of the GOES 1–8 Å derivative. The measured lags

Table 5.2: Summary of temporal and response properties of the analysed flares. Listed are the number of detected GOES derivative episodes, the characteristic time lag between the peak of the magnetic field change time distribution (t_B) and the dominant GOES derivative fluctuation, and the fraction of step-like B_h pixels occurring during the impulsive phase for increasing (inc) and decreasing (dec) clusters.

Flare	GOES Fluct.	$t_B - t_{\mathrm{GOES}}$ (s)	Step-like B_h Pixels During Impulsive Phase (%)
20110215_0144_11158_X2.2	13	11.9	60.75% (inc), 37.85% (dec)
20110906_2212_11283_X2.1	5	126.4	19.70% (inc), 29.10% (dec)
20120307_0002_11429_X5.4	22	20.8	79.37% (inc), 65.78% (dec)
20140825_2006_12146_M3.9	14	90.1	67.45% (inc), 52.22% (dec)
20141218_2141_12241_M6.9	25	173.5	38.39% (inc), 29.48% (dec)
20141220_0011_12242_X1.8	31	−33.9	66.29% (inc), 32.52% (dec)

range from −33.9 s to 173.5 s, with most events exhibiting positive delays on the order of tens to a few hundred seconds. These values remain small compared to the duration of the impulsive phase, indicating near-simultaneous temporal evolution of the coronal energy release episodes and the photospheric magnetic response.

To further quantify this relationship, the impulsive phase is defined as the interval during which the GOES 1–8 Å derivative remains positive. Within this interval, we calculate the fraction of pixels exhibiting step-like B_h changes. The results show that a substantial proportion of increasing cluster pixels occur during the impulsive phase, ranging from 38% (2014-12-18, M6.9) to 79% (2012-03-07, X5.4). In several events, this fraction exceeds 60%, indicating that the majority of increasing B_h changes are temporally confined to periods of enhanced coronal energy release. In contrast, the fraction of decreasing-cluster pixels occurring during the impulsive phase is generally lower, spanning from 29% to 66%. In multiple events, decreasing B_h changes appear more broadly distributed in time and are less strongly concentrated within the impulsive interval. This behaviour may indicate that a larger fraction of pixels in the decreasing cluster are not directly associated with the flare-related changes, but instead reflect noise-like fluctuations or unrelated step-like changes in the magnetic field.

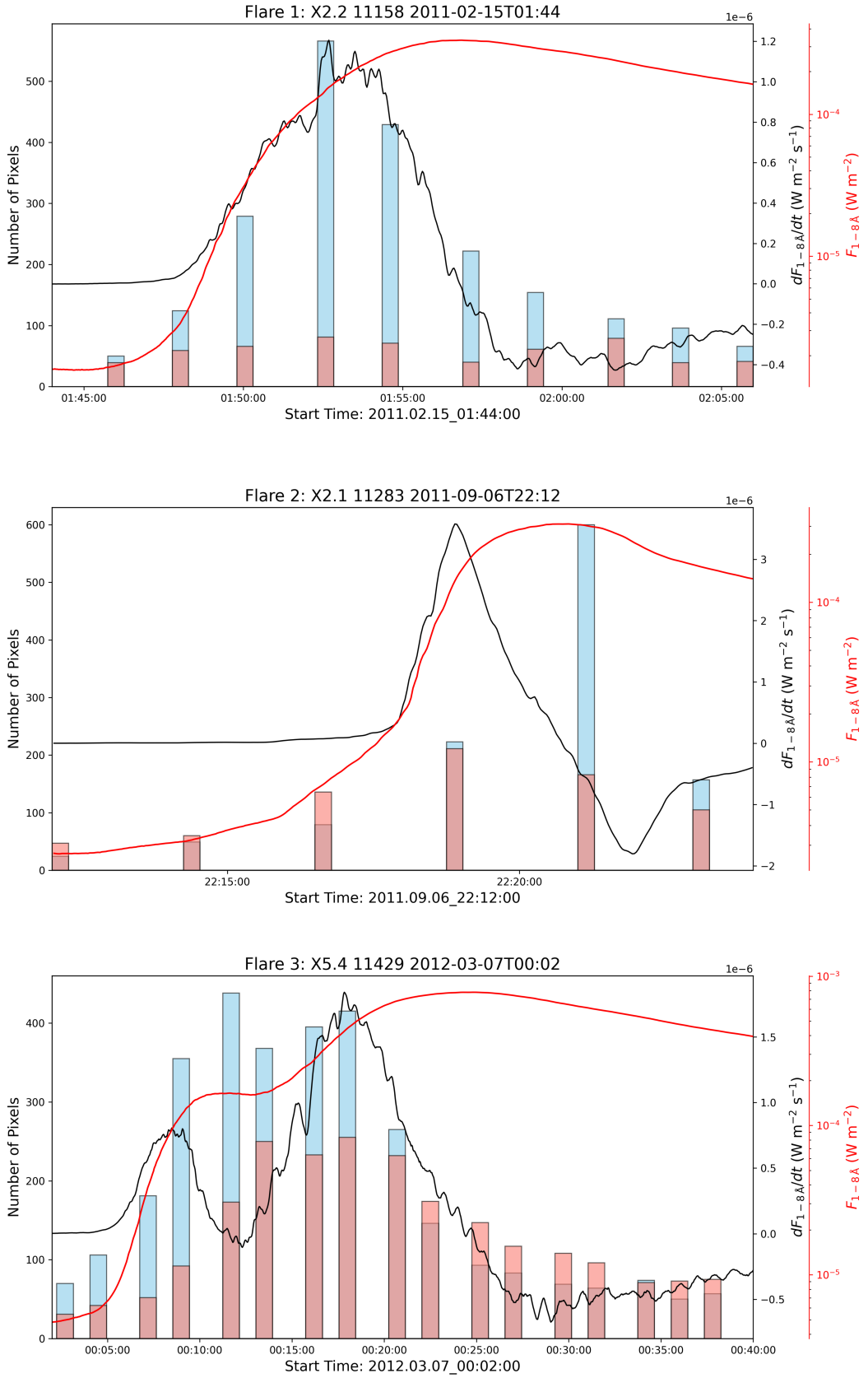

Figure 5.3: Temporal distribution of step-like changes in the horizontal magnetic field (B_h) for three X-class flares. Blue bars denote pixels exhibiting step-like increases in B_h, while red bars denote pixels showing decreases. The black curve represents the time derivative of the GOES 1–8 Å soft X-ray flux ($dF_{1–8}/dt$), and the red curve shows the GOES 1–8 Å flux ($F_{1–8}$).

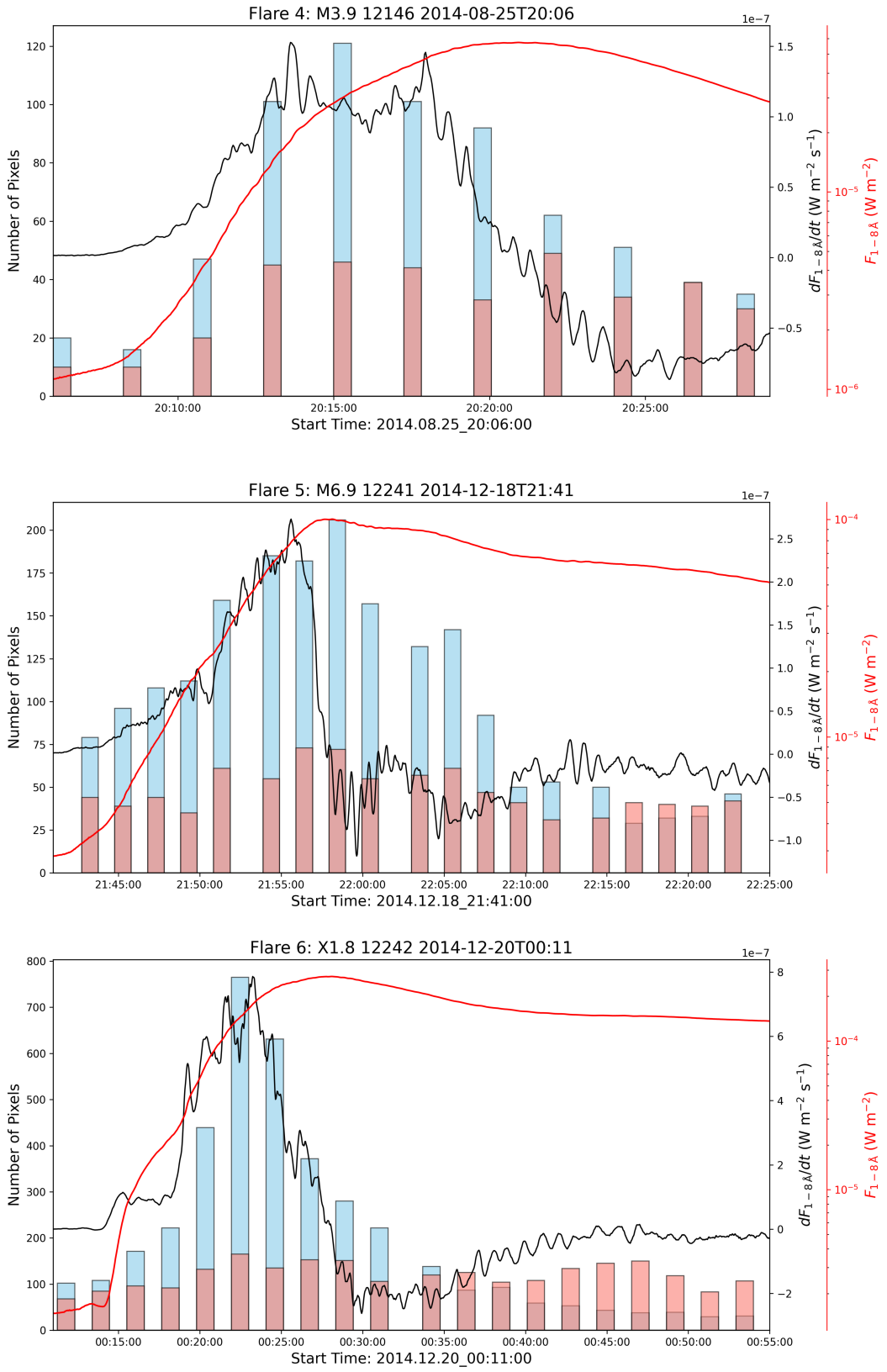

Figure 5.4: Same as Figure 5.3, but for Flares 4–6

5.3.2.2 Spatial Behaviour During Coronal Energy Release

Using the temporal–spatial association method described in Section 5.2.3.1, each pixel exhibiting a step-like change in B_h is assigned the index of the nearest GOES 1–8 Å derivative fluctuation. Therefore, the resulting fluctuation-index maps encode the temporal ordering of coronal energy-release episodes in spatial form. In Figures 5.5–5.9, the upper panels show the colour-coded GOES derivative, while the lower panels present the corresponding spatial association maps for each flare.

Flare 1: X2.2 (2011-02-15, NOAA 11158): The GOES derivative shows multiple closely spaced episodes (indices 1–13). Early indices (1–4; red–orange) form a compact, elongated structure co-spatial with the main polarity inversion line (PIL). Intermediate indices (5–9; yellow–green) extend along the PIL and into adjacent penumbrae, broadening primarily in the east–west direction while remaining aligned with the main PIL. Late indices (10–13; cyan–blue) occupy a wider surrounding area, appearing in fragmented patches along extended PIL segments and nearby plage. Pixels in the decreasing-B_h cluster are more spatially dispersed and are predominantly associated with intermediate-to-late indices.

Flare 2: X2.1 (2011-09-06, NOAA 11283): Five episodes (indices 1–5) are identified. Early indices (1–2; red–orange) appear in small, localised patches near the central sunspot complex and along short segments of the PIL. The dominant spatial structure is associated with the later episodes (indices 4–5; cyan–blue), which form the largest elongated region along the central PIL. Index 3 occupies intermediate portions of this band but covers a smaller area. The overall spatial evolution remains compact, with decreasing-B_h pixels appearing mainly at later indices in small, isolated patches.

Flare 4: M3.9 (2014-08-25, NOAA 12146): Fourteen episodes are detected. Early indices (1–3) are localised near the central PIL between the dominant sunspots. Intermediate indices (4–8; yellow–green) extend along the PIL and into the penumbrae, maintaining a clear elongation along the PIL direction. Late indices (9–13; cyan–blue) are more dispersed across extended inversion-line segments and peripheral sunspots. Decreasing-B_h pixels are associated with later indices.

Flare 5: M6.9 (2014-12-18, NOAA 12241): The flaring phase contains 25 episodes. Early indices (1–5) are concentrated along a sharply defined, curved PIL segment, forming a narrow ribbon-like structure. Intermediate indices (6–15; orange–green) expand both along and transverse to the PIL, producing multiple contiguous patches in penumbral. Late indices (16–25; cyan–dark blue) extend across a broad area, including plage, with increasing spatial fragmentation. Decreasing-B_h pixels are primarily linked to intermediate and late indices.

Flare 6: X1.8 (2014-12-20, NOAA 12242): Thirty-one episodes are identified. Early indices (1–6; red–orange) define a compact structure along the central PIL. Intermediate indices (7–18; yellow–green) expand along the full PIL length and into the penumbrae. Late indices (19–31; cyan–dark blue) are widely distributed across peripheral plage and isolated magnetic regions, resulting in a fragmented spatial pattern. Decreasing-B_h pixels are predominantly associated with intermediate-to-late indices and appear spatially dispersed.

Across all six flares, a systematic spatial progression appears clearly. Early fluctuation indices are predominantly concentrated along the main polarity inversion line, intermediate indices extend along and around this structure, and later indices are distributed more broadly across the active region. Pixels belonging to the decreasing-B_h cluster are generally associated with intermediate-to-late fluctuation indices and exhibit a comparatively more dispersed spatial distribution.

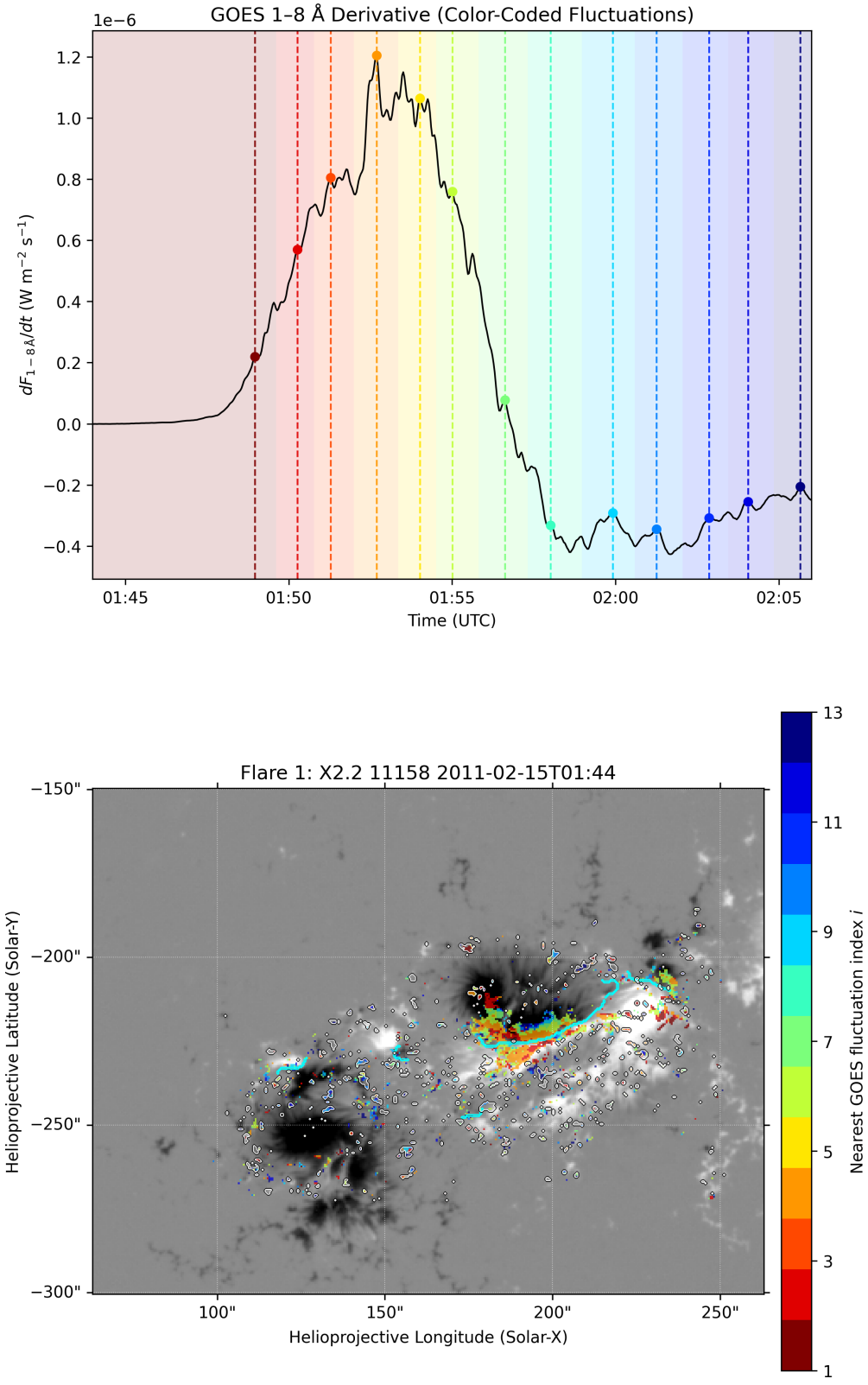

Figure 5.5: Top: Time series of the GOES 1–8 Å soft X-ray flux derivative for the X2.2 flare on 2011 February 15 2011 in NOAA AR 11158, with coronal energy release episodes identified after smoothing. Each shaded interval and marker is colour-coded according to the temporal index of the detected fluctuation.Bottom: Fluctuation association map showing the spatial distribution of photospheric pixels exhibiting step-like changes in the horizontal magnetic field (B_h), overlaid on the pre-flare B_r background. Pixels are coloured by the nearest GOES fluctuation in time, using the same colour scheme as in the top panel. Cyan contours mark the polarity inversion line. Pixels with a decreasing magnetic field are contoured in black and white.

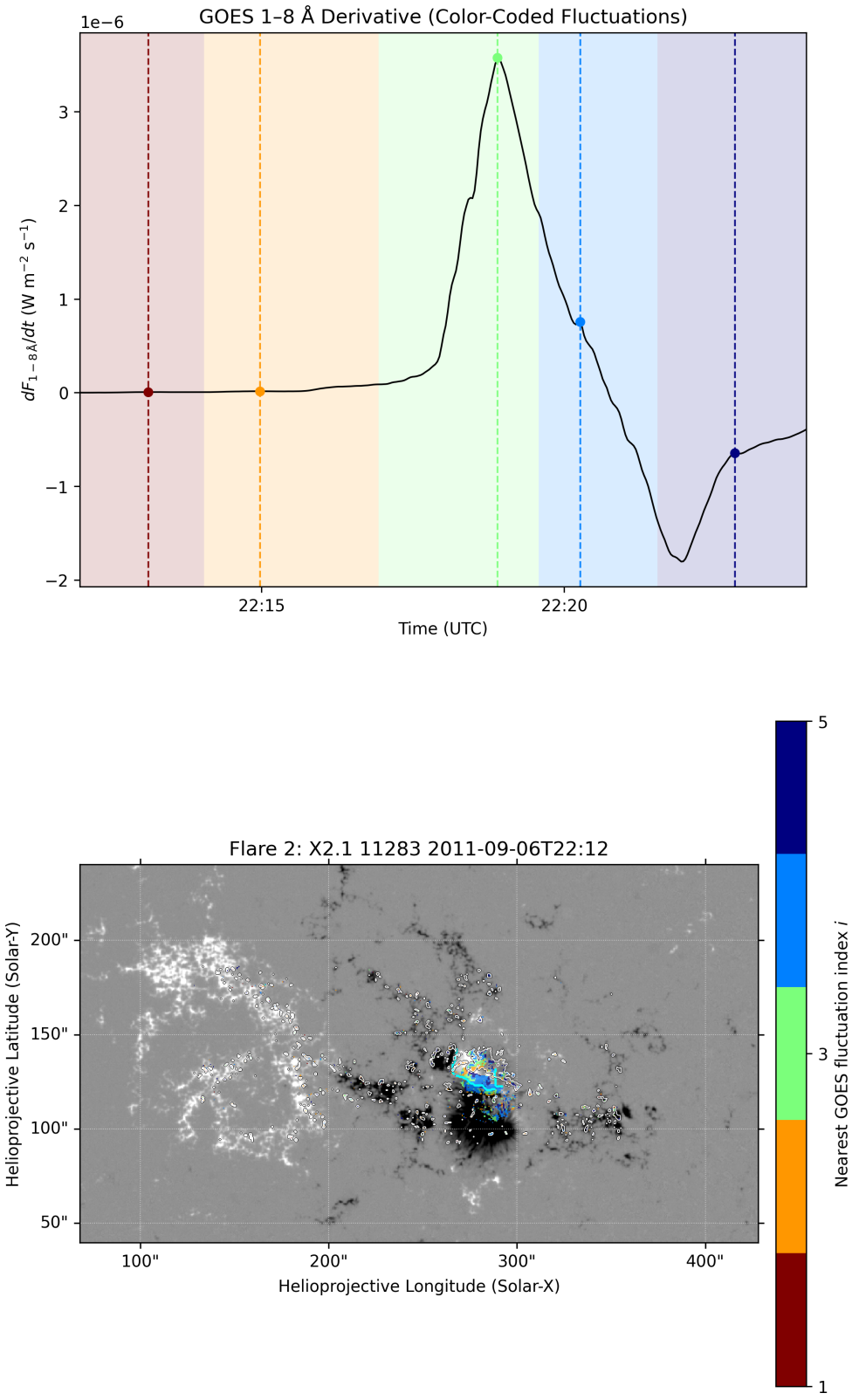

Figure 5.6: Same as Figure 5.5, but for X 2.1 flare on 2011 Septemper 6 in AR NOAA 11158.

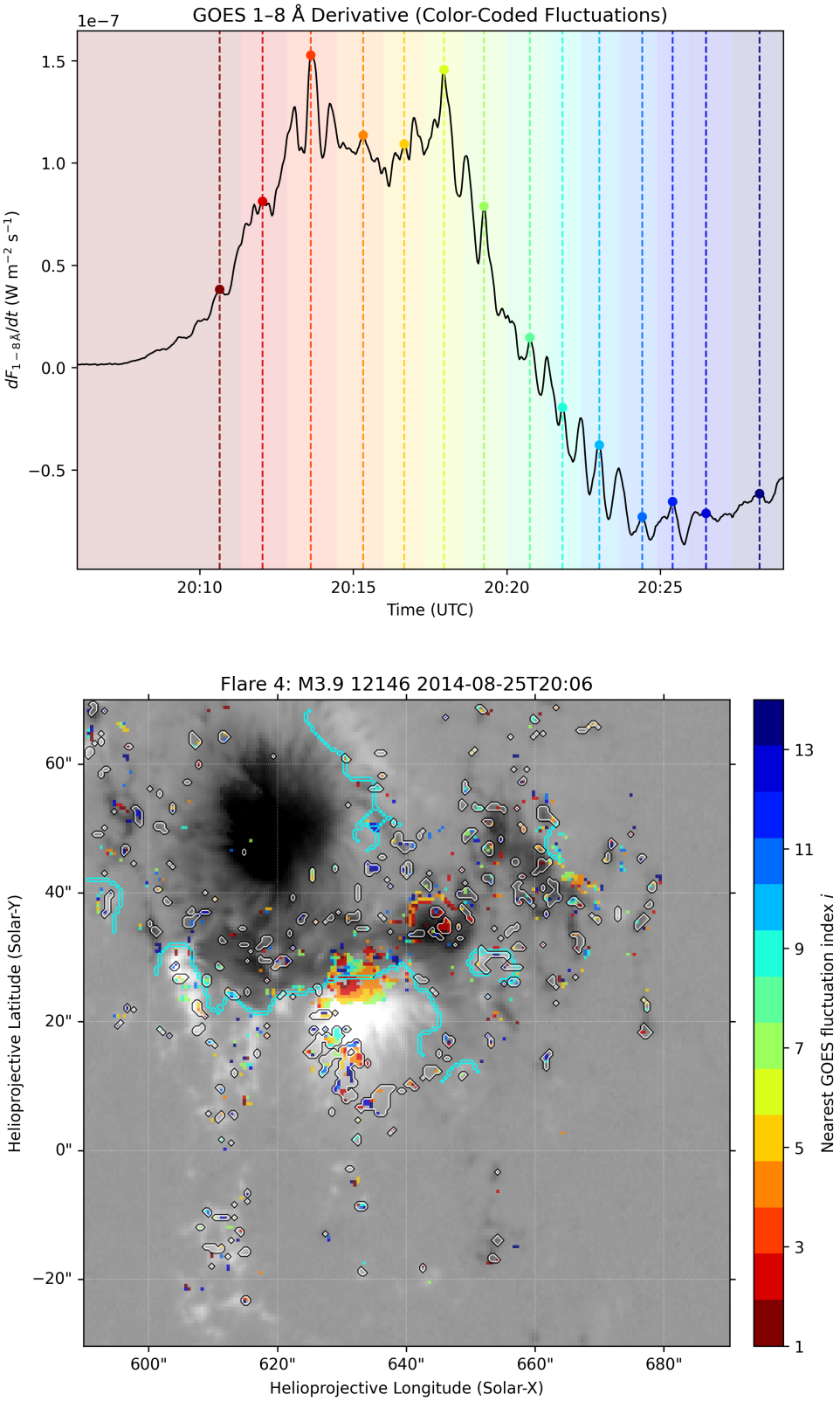

Figure 5.7: Same as Figure 5.5, but for M3.9 flare on 2014 August 25 in NOAA AR 12146.

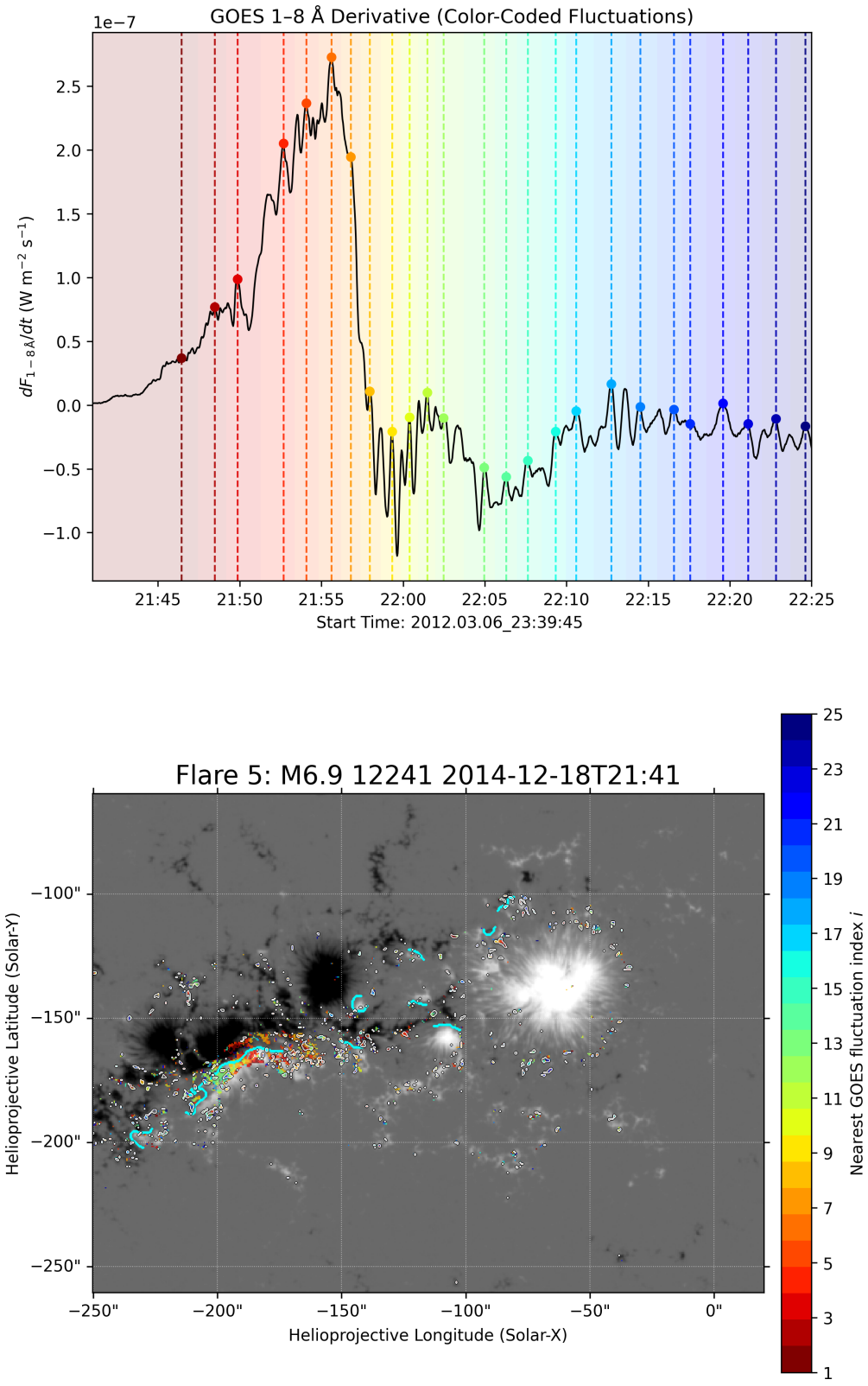

Figure 5.8: Same as Figure 5.5, but for M6.9 flare on 2014 December 18 in NOAA AR 12241.

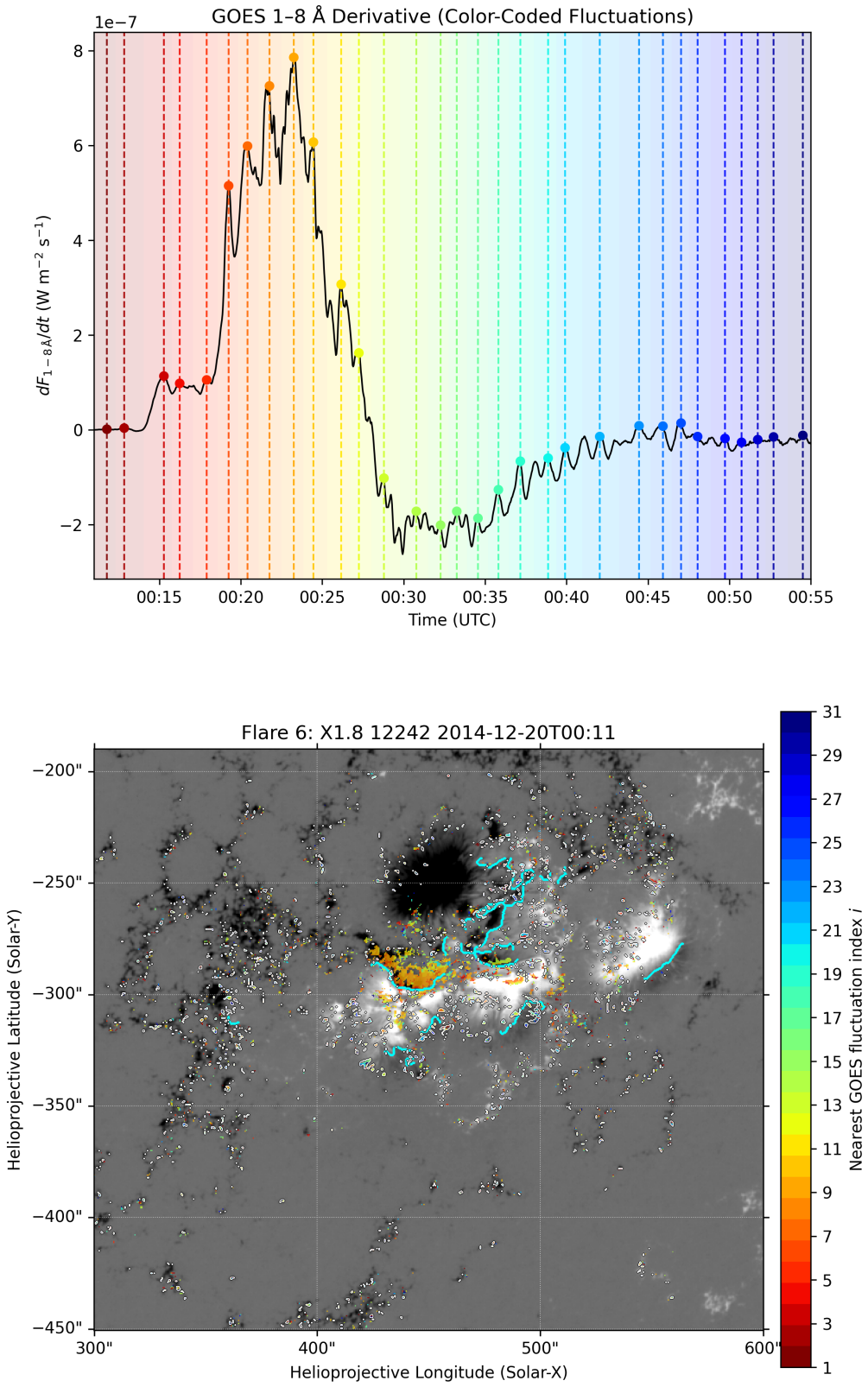

Figure 5.9: Same as Figure 5.5, but for X1.8 flare on 2015 November 7 in NOAA AR 12242.

5.3.2.3 Statistical Correlation Between the Number of Magnetic Response Pixels and Coronal Energy Release

To quantify how the spatial extent of the photospheric magnetic response scales with coronal energy release, we construct scatter plots between the number of pixels undergoing step-like B_h changes within each temporal bin and the corresponding value of the GOES 1–8 Å derivative. The GOES derivative serves as a proxy for the instantaneous coronal energy-release rate, while the pixel count represents the spatial extent of the photospheric magnetic field changes. To isolate the physically meaningful photospheric response to coronal energy release, only time intervals corresponding to positive values of the GOES soft X-ray derivative were considered. Negative derivative intervals, associated with the decay phase of the flare, were excluded as they are dominated by noise-like fluctuations and do not represent active energy release. A linear regression of the form $y = mx + b$ is applied to evaluate whether stronger coronal energy-release episodes systematically involve a larger area of magnetic-field reconfiguration.

Figures 5.10 and 5.11 present the linear regression analysis between the number of responding pixels and the derivative of GOES 1–8 Å for all six flares, considering only time intervals with positive derivative values of the GOES. Across the full sample, strong and consistently positive correlations are observed for pixels exhibiting increasing B_h, with Pearson correlation coefficient values of 0.98, 0.97, and 0.74 for the X-class flares (Flares 1–3), and 0.92, 0.99, and 0.89 for Flares 4–6, respectively. For pixels exhibiting decreasing B_h, the correlations remain positive but are generally lower, with CC values of 0.92, 0.87, and 0.67 for Flares 1–3, and 0.96, 0.79, and 0.69 for Flares 4–6. The linear fits in all panels show an overall increasing trend between the number of pixels per bin and the GOES derivative.

Taken together, these results indicate that increasing B_h pixels demonstrates a systematically stronger correlation with the GOES derivative than decreasing pixels. This trend becomes particularly stronger in the more energetic X-class flares, where the number of pixels undergoing horizontal field enhancement increases proportionally with the coronal energy-release rate. In contrast, decreasing B_h changes appear less tightly coupled to instantaneous coronal energy release.

5.4 Discussion

In this chapter, we investigate the temporal relationship between coronal energy release and photospheric magnetic field evolution during solar flares. The time derivative of the soft X-ray flux of GOES 1–8 Å $dF_{1-8,}/dt$, is used as a proxy for the release of coronal energy. In parallel, we employed the high-cadence (135 s) vector magnetic field measurements from HMI to quantify time of the changes in the horizontal magnetic field (t_B). This investigation was applied to a sample of six flares.

The primary result of this chapter is that the dominant peaks in the t_B histograms which correspond to the maximum $|dB_h/dt|$ at individual pixels, are concentrated within the impulsive phase of each flare and coincide with the strongest peaks in the GOES derivative, as shown in Figures 5.3 and 5.4. This temporal alignment indicates that enhanced coronal energy release is systematically accompanied by an increase in the number of pixels undergoing rapid horizontal magnetic field changes, demonstrating a clear temporal coupling between coronal energy release and photospheric magnetic changes. Previous studies reported significant correlations between longitudinal magnetic field and flux changes and the GOES peak X-ray flux, suggesting that photospheric magnetic change is correlated with flare energy release (Petrie and Sudol, 2010). Similarly, Castellanos Durán et al., 2018

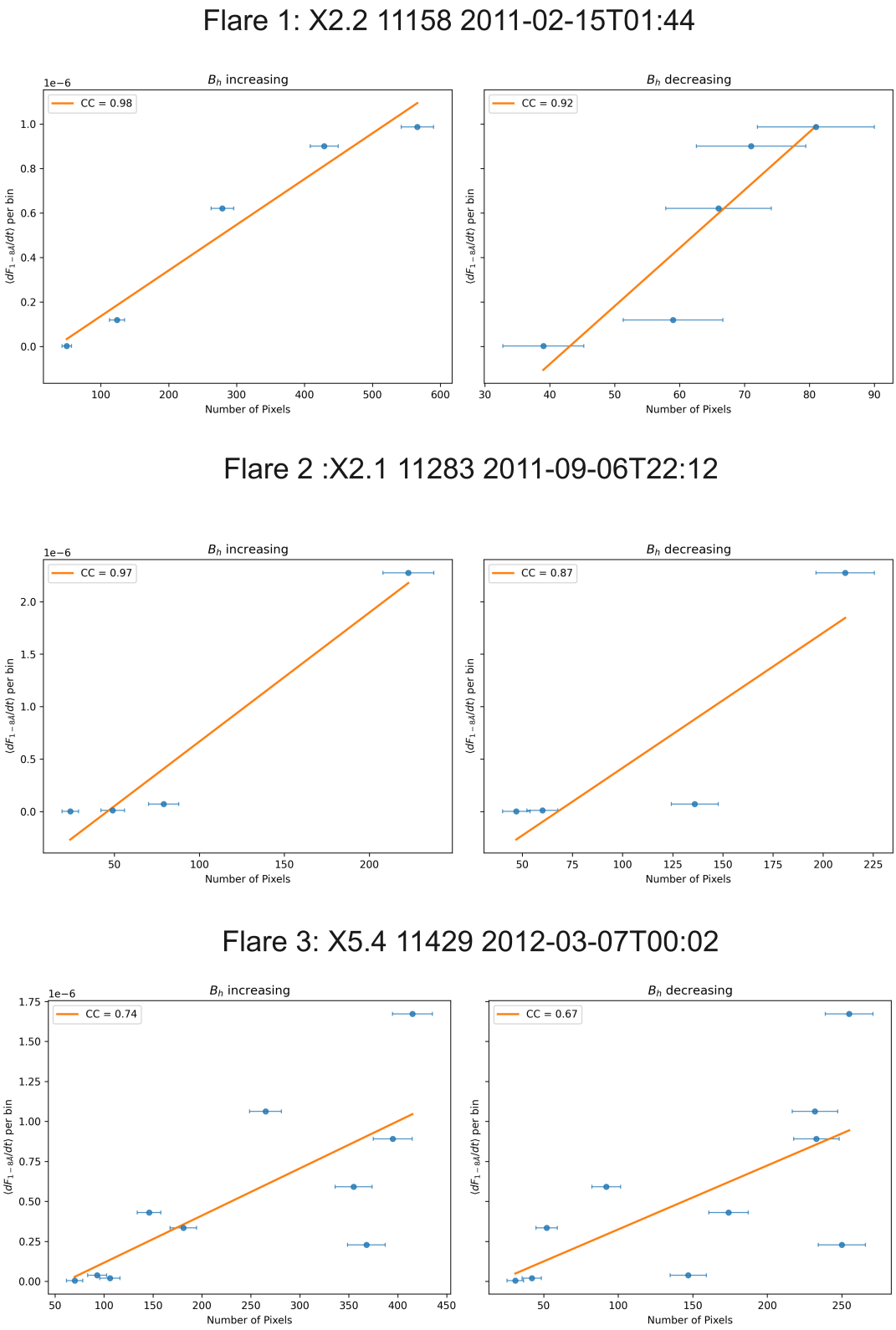

Figure 5.10: Scatter plots showing the relationship between the number of pixels exhibiting step-like changes in the horizontal magnetic field (B_h) per time bin (1-minute cadence) and the corresponding binned value of the GOES soft X-ray derivative ($dF_{1–8}/dt$) for Flares 1–3. Left panels show pixels with increasing B_h, and right panels show pixels with decreasing B_h. Error bars represent bin widths in pixel counts. The orange line indicates the best-fit linear regression, and the Pearson correlation coefficient (CC) is reported in each panel.

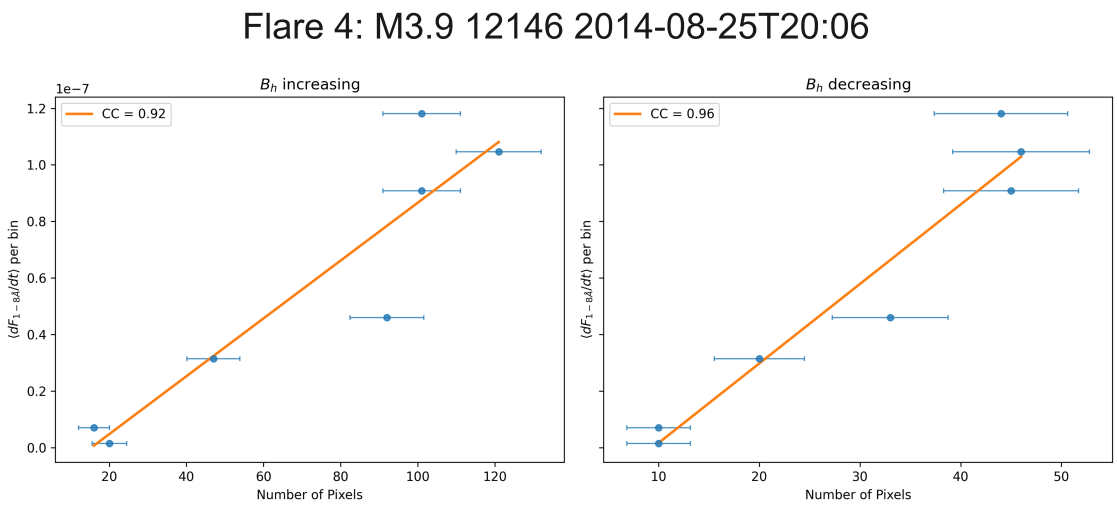

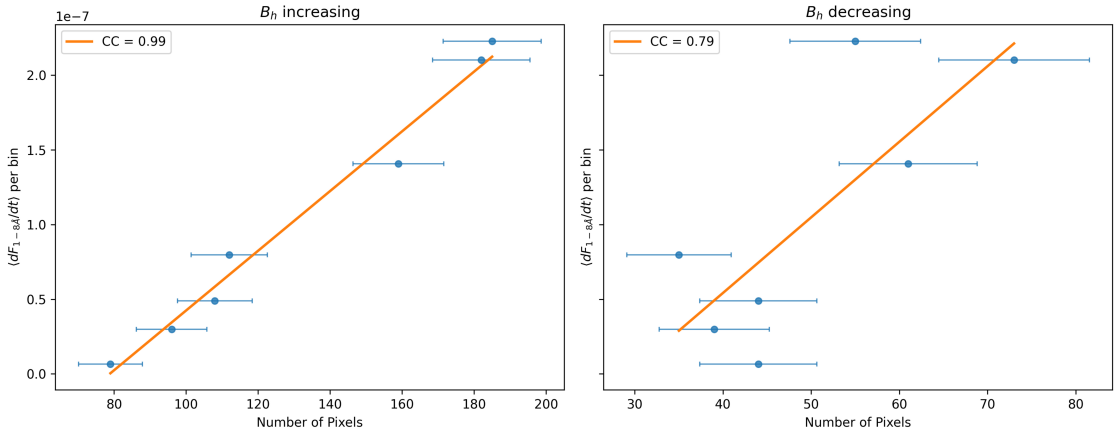

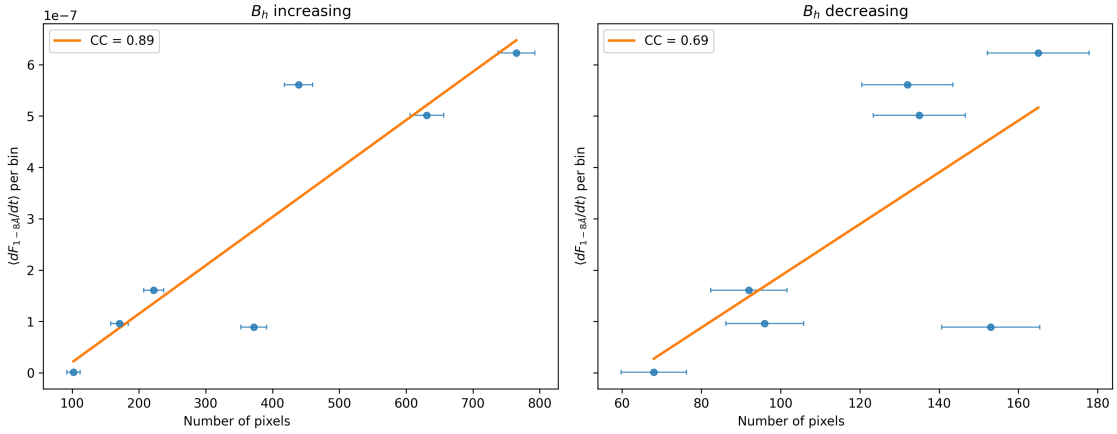

Figure 5.11: Same as Figure 5.10, but for three Flares 4–6.

found that GOES peak flux correlates with the magnitude and spatial extent of photospheric magnetic field changes. However, this study provides pixel-level, time-resolved evidence that the temporal evolution of coronal energy release dynamically tracks the photospheric magnetic response.

The strong statistical correlation between the number of pixels exhibiting step-like increases in $\boldsymbol{B}_h$ and the GOES soft X-ray derivative indicates that the spatial extent of the photospheric magnetic response scales linearly with the magnitude of the coronal energy-release rate, as proxied by the GOES derivative. This suggests that the high correlation coefficients obtained across all six flares indicate that more intense energy-release episodes are associated with a larger number of pixels undergoing horizontal magnetic field enhancement. Such behaviour is comparable to previous findings that flare ribbon area and reconnected magnetic flux increase systematically with flare magnitude (Qiu et al., 2004b; Kazachenko et al., 2017). By contrast, although pixels exhibiting decreasing $\boldsymbol{B}_h$ also show positive correlations, these are systematically lower, indicating that field weakening is less coherently related to the global coronal energy-release process.

The temporal-spatial association maps (Figures 5.5–5.9) reveal a coherent temporal–spatial correspondence between episodes in the GOES soft X-ray derivative and the distribution of step-like changes in the horizontal magnetic field. Sequential episodes of coronal energy-release are reflected in an ordered spatial progression of $\boldsymbol{B}_h$ changes across the active region. While early episodes are mostly associated with magnetic-field changes concentrated along the main polarity inversion line, later episodes correspond to progressively more extended and fragmented regions. When the derivative becomes negative (i.e. during the decay phase), the detected changes appear more spatially scattered and less coherent, suggesting that many of these signals may reflect random or noise-like fluctuations that are not necessarily directly associated with the flare. The structured progression identified here is consistent with such dynamically evolving reconnection, indicating that sequential coronal episodes leave clear photospheric magnetic signatures. Namely, magnetic reconnection during flares is understood to proceed in a time-dependent way, with reconnection

sites evolving spatially as flare ribbons expand and newly reconnected field lines map to the lower atmosphere (Shibata and Magara, 2011; Fletcher et al., 2011). Within the coronal implosion framework proposed by Hudson, 2000, flare energy release implies a reduction of coronal magnetic pressure and a consequent contraction of overlying field structures. Therefore, the temporally resolved behaviour observed here provides observational support for the implosion scenario, demonstrating that strong coronal energy-release episodes are systematically associated with structured photospheric magnetic changes. However, the present analysis is based on a sample of six flares, and extension to a larger statistical dataset will be necessary to assess the generality of the temporally structured behaviour identified here.

5.5 Conclusions

We have investigated the temporal and spatial coupling between coronal energy release and photospheric magnetic field change during six selected flares, using the GOES soft X-ray derivative as a proxy for the coronal energy release episodes. The main conclusions of this work are as follows:

1. The spatial association maps reveal a coherent evolution pattern. Early coronal energy-release episodes are concentrated along the main polarity inversion line (PIL), intermediate episodes extend along and around the PIL, and later episodes propagate into peripheral penumbral and plage regions. This indicates that the temporal sequence of coronal energy release is imprinted spatially across the active region.
2. Across all six flares, the dominant peaks in the distribution of t_B (the time of maximum $|dB_h/dt|$) are concentrated within the impulsive phase and coincide with the strongest peaks in the GOES 1–8 Å derivative. This confirms that coronal energy-release episodes are systematically accompanied by rapid horizontal magnetic field changes in the photosphere.

3. The measured time lags between the peak of the magnetic response and the dominant GOES derivative peak range from -33.9 s to 173.5 s. These delays are small compared to the impulsive-phase duration, indicating that the photospheric magnetic changes evolve nearly simultaneously with coronal energy release.
4. A substantial fraction of pixels exhibiting step-like increases in B_h occurs during the impulsive phase, frequently exceeding 60% in several events. This demonstrates that horizontal magnetic field changes are temporally confined to intervals of enhanced coronal energy release.
5. Increasing-B_h pixels show stronger temporal concentration within the impulsive phase and systematically higher correlation coefficients with the GOES derivative. In contrast, decreasing-B_h changes are more broadly distributed in time and exhibit weaker correlations
6. Linear regression analysis shows that the number of pixels undergoing step-like increases in B_h is strongly positively correlated with the GOES 1–8 Å derivative, with correlation coefficients reaching up to 0.99 across the six flares. This demonstrates that more intense coronal energy-release episodes are associated with a correspondingly larger area of photospheric magnetic-field enhancement.

Overall, the spatial association maps support a clear temporal–spatial link between coronal energy-release episodes and photospheric magnetic changes. The ordered progression of fluctuation on the coronal energy-release, from concentrated regions along the main polarity inversion line to more extended and fragmented areas, reflects the evolving nature of magnetic reconnection during flares. This behaviour is consistent with time-dependent reconnection and the coronal implosion scenario, in which changes in coronal magnetic pressure are rapidly transferred to the lower atmosphere. These results provide observational evidence that successive coronal energy-release episodes leave structured and measurable signatures in the photospheric magnetic field.

Chapter 6

Conclusion

6.1 Thesis Summary

It is broadly known that solar flares are driven by the rapid release of magnetic energy in the corona through magnetic reconnection. However, the response of the photospheric magnetic field to this energy release is still not fully understood. The primary aim of this work was to investigate the evolution of the photospheric magnetic field during solar flares. Specifically, we examine the temporal and spatial relationship between magnetic field changes, chromospheric flare emission and proxies of coronal energy release.

The first study in Chapter 3 investigated the spatially and temporally varying line-of-sight magnetic field behaviour exclusively within flare ribbon regions, which are recognised as visual markers indicating the chromospheric endpoints of the magnetic field that is undergoing coronal reconnection, the process thought to be the driver of flares. We studied six M-class flares, using 45s-cadence magnetograms obtained from (SDO/HMI, AIA). To characterise the temporal evolution of the magnetic field, we applied unsupervised machine learning techniques, namely k-shape clustering, to identify different patterns of behaviour within the time series. Our findings reveal that the strongest changes in the magnetic field can either precede or lag the UV peaks in different locations, but that in 4 of the

6 flares, on average the magnetic field changes preceded the UV peak typically by a few minutes. We report oscillations in the LoS magnetic field which might not be a flare-related change, as well as the previously-studied monotonic changes. We have identified a moderate correlation between the absolute magnetic field strength (|B|) and the rate of magnetic field change (|dB/dt|), indicating that on average stronger magnetic fields experience higher rates-of-change, up to a maximum of 8.6 $\mathrm{G\,min^{-1}}$ on average. These results provide insight into the dynamic magnetic processes governing flare evolution, caused by the reconfiguration of the magnetic field, and release of magnetic energy that results in the generation of ribbon radiation.

However, this study is limited by the small dataset and by the use of the line-of-sight magnetic field, which may not fully capture the magnetic field changes associated with flares, as these changes are expected to be stronger in the horizontal field. This motivated us to study a larger number of flares across a wider range of flare classes to obtain more general conclusions. Chapter 4 investigated the spatial and temporal changes in the behaviour of $\boldsymbol{B}_{\mathrm{h}}$ using unsupervised machine learning, namely k-shape clustering, to identify regions exhibiting step-like changes in $\boldsymbol{B}_{\mathrm{h}}$. We analysed 35 solar flares spanning X-, M-, and C-class events, using 135 s-cadence vector magnetograms obtained from SDO/HMI and ultraviolet observations from AIA. Our results show that (i) in 14 out of 35 flares examined, stepwise increases in the horizontal magnetic field are concentrated near the region of polarity inversion and show spatial and temporal association with the onset of flare ribbon emission; (ii) the peak rate of increase of $\boldsymbol{B}_{\mathrm{h}}$ generally lags the onset of UV ribbon brightening by several minutes and this time lag shows no statistically significant dependence on flare class; (iii) the lag increases with increasing distance from the region of polarity inversion; and (iv) decreases in $\boldsymbol{B}_{\mathrm{h}}$ are more scattered across the active region and its penumbra. The increase of $\boldsymbol{B}_{\mathrm{h}}$ progressing outwards from the region of polarity inversion provides strong observational evidence of the photospheric response to the sequential relaxation and downward contraction of coronal magnetic fields during energy release, sometimes identified as a coronal 'implosion'.

Finally, in Chapter 4, we found that the spatial distribution of the time lag between the magnetic field change and the onset of UV ribbon brightening tends to increase with distance from the polarity inversion line in some flares. This behaviour motivated a further investigation of the temporal–spatial relationship between coronal energy release and the evolution of the horizontal magnetic field in the photosphere, to determine whether this trend remains consistent across events. In Chapter 5, we investigated the temporal and spatial association between impulsive coronal energy-release episodes and step-like changes in the horizontal magnetic field (B_h) in six M- and X-class solar flares. The time derivative of the GOES 1–8Å soft X-ray flux is used as a proxy for coronal energy release. The results showed that the dominant peaks in the distribution of magnetic-field change times (t_B) occur during the impulsive phase of the flares and coincide with the strongest peaks in the GOES soft X-ray derivative. The measured time delays between coronal energy release and photospheric magnetic response range from -34 s to 174 s, indicating an evolution that is near-simultaneous relative to the cadence of 135 s of the magnetic field observations. Furthermore, spatial association maps revealed a systematic progression of magnetic-field changes from the main polarity inversion line outward across the active region. These results provide observational evidence for a close temporal–spatial coupling between coronal energy release and photospheric magnetic-field evolution, consistent with the coronal implosion scenario.

Overall, the results presented in this thesis provide new insight into the temporal and spatial coupling between flare emissions and photospheric magnetic-field evolution during solar flares. The findings show that changes in the photospheric magnetic field are closely associated with flare ribbon emission and the impulsive release of coronal magnetic energy. In this context, the observed increases in the horizontal magnetic field near the polarity inversion line are consistent with the downward contraction and relaxation of coronal magnetic fields during flares, supporting the coronal implosion scenario. These results contribute to our understanding of how magnetic energy released in the corona is communicated to the lower solar atmosphere during solar flares.

6.2 Future Work

The cadence of Solar Dynamics Observatory / Helioseismic and Magnetic Imager (SDO/HMI) vector magnetic field data is 135 s with a spatial sampling of approximately 0.6 arcsec per pixel. Therefore, it does not capture very rapid or fine-scale magnetic evolution. Future studies could benefit from observations with higher resolution provided by ground-based solar telescopes. For example, the Daniel K. Inouye Solar Telescope (DKIST), which offers improved capabilities, with spatial sampling as fine as 0.03 arcsec per pixel and cadences that can reach a few seconds (Rimmele et al., 2020). Such high-resolution observations would allow much finer structures within flare ribbons or around the magnetic polarity inversion line (PIL) to be resolved.

In addition, the analysis presented in Chapter 5 could be extended to estimate the magnetic energy change associated with the flare. Since the horizontal magnetic field evolution has already been determined for each pixel, the magnetic energy density could be approximated using:

$$u_B = \frac{B^2}{2\mu_0}, \tag{6.1}$$

where B is the magnetic field strength and μ_0 is the magnetic permeability of free space. By comparing the magnetic field before and after the flare, it would be possible to estimate changes in magnetic energy density across the region of interest. However, to estimate the total magnetic energy change, it would also be necessary to determine the corresponding volume change, ΔV, of the contracting or shrinking magnetic loops, such that the total released energy could be approximated as $u_B \times \Delta V$. This would require an estimate of the loop geometry before and after the flare, in particular, the loop length. A first geometrical approximation could be made using the observed change in the inclination angle of the magnetic field, which may provide a proxy for the contraction of the coronal field.

Another direction for future work is the investigation of the oscillatory behaviour identified in Chapter 3. It remains unclear whether these variations represent a real oscillatory response of the magnetic field or are due to observational or analysis effects. Since this behaviour was identified in the line-of-sight magnetic field, the analysis should be repeated using the horizontal magnetic field, where flare-related changes are expected to be stronger. At the same time, the coronal response should be examined to test whether oscillatory changes in the photospheric field are accompanied by oscillations of coronal magnetic loops. A combined analysis of photospheric magnetic evolution and coronal dynamics would help determine whether the observed oscillations are related to a flare.

Bibliography

Alanazi, N. and L. Fletcher (May 2025). 'The relationship between solar flare ribbons and magnetic field changes in the solar photosphere'. In: *Monthly Notices of the Royal Astronomical Society* 540.3, pp. 2474–2485. doi: 10.1093/mnras/staf882.

Alanazi, N. and L. Fletcher (Mar. 2026). 'Systematic Time Evolution of the Horizontal Magnetic Field Around the Polarity Inversion Line in Flares'. In: *Monthly Notices of the Royal Astronomical Society*, stag573. doi: 10.1093/mnras/stag573.

Aschwanden, M. J. (2004). *Physics of the Solar Corona: An Introduction*.

Astropy Collaboration et al. (Aug. 2022). 'The Astropy Project: Sustaining and Growing a Community-oriented Open-source Project and the Latest Major Release (v5.0) of the Core Package'. In: *ApJ* 935.2, 167, p. 167. doi: 10.3847/1538-4357/ac7c74. arXiv: 2206.14220 [astro-ph.IM].

Aulanier, G., E. DeLuca, S. Antiochos, R. McMullen and L. Golub (2000). 'The topology and evolution of the Bastille day flare'. In: *The Astrophysical Journal* 540.2, pp. 1126–1142.

Barczynski, K., G. Aulanier, S. Masson and M. S. Wheatland (2019). 'Flare reconnection-driven magnetic field and Lorentz force variations at the Sun's surface'. In: *The Astrophysical Journal* 877.2, p. 67.

Benz, A. O. (2017). 'Flare observations'. In: *Living reviews in solar physics* 14.1, p. 2.

Bi, Y., Y. D. Liu, Y. Liu, J. Yang, Z. Xu and K. Ji (2018). 'A survey of changes in magnetic helicity flux on the photosphere during relatively low-class flares'. In: *The Astrophysical Journal* 865.2, p. 139.

Borrero, J., S. Tomczyk, M. Kubo, H. Socas-Navarro, J. Schou, S. Couvidat and R. Bogart (2011). 'VFISV: very fast inversion of the Stokes vector for the helioseismic and magnetic imager'. In: *Solar Physics* 273.1, pp. 267–293.

Burtseva, O., J. Martínez-Oliveros, G. Petrie and A. Pevtsov (2015). 'Hard X-ray emission during flares and photospheric field changes'. In: *The Astrophysical Journal* 806.2, p. 173.

Carmichael, H. (1964). '54 A PROCESS FOR FLARES'. In: *NASA SP.* 50, p. 451.

Carrington, R. C. (Nov. 1859). 'Description of a Singular Appearance seen in the Sun on September 1, 1859'. In: *MNRAS* 20, pp. 13–15. doi: 10.1093/mnras/20.1.13.

Castellanos Durán, J. S., L. Kleint and B. Calvo-Mozo (2018). 'A statistical study of photospheric magnetic field changes during 75 solar flares'. In: *The Astrophysical Journal* 852.1, p. 25.

Charbonneau, P. (2014). 'Solar dynamo theory'. In: *Annual Review of Astronomy and Astrophysics* 52.1, pp. 251–290.

Cheng, C.-C., E. Oran, G. Doschek, J. Boris and J. Mariska (1983). 'Numerical simulations of loops heated to solar flare temperatures. I'. In: *The Astrophysical Journal* 265, pp. 1090–1119.

Cliver, E., G. Petrie and A. Ling (2012). 'Abrupt changes of the photospheric magnetic field in active regions and the impulsive phase of solar flares'. In: *The Astrophysical Journal* 756.2, p. 144.

Couvidat, S., J. Schou, R. A. Shine, R. I. Bush, J. W. Miles, P. H. Scherrer and R. L. Rairden (2012). 'Wavelength dependence of the Helioseismic and Magnetic Imager (HMI) instrument onboard the Solar Dynamics Observatory (SDO)'. In: *Solar Physics* 275.1, pp. 285–325.

Crosby, N. B., M. J. Aschwanden and B. R. Dennis (Feb. 1993). 'Frequency distributions and correlations of solar X-ray flare parameters'. In: *Sol. Phys.* 143.2, pp. 275–299. doi: 10.1007/BF00646488.

De Wijn, A., J. O. Stenflo, S. K. Solanki and S. Tsuneta (2009). 'Small-scale solar magnetic fields'. In: *Space Science Reviews* 144.1, pp. 275–315.

Dennis, B. R. and D. M. Zarro (1993). 'The Neupert effect: What can it tell us about the impulsive and gradual phases of solar flares?' In: *Solar Physics* 146.1, pp. 177–190.

Durán, J. S. C. and L. Kleint (2020). 'The statistical relationship between white-light emission and photospheric magnetic field changes in flares'. In: *The Astrophysical Journal* 904.2, p. 96.

Emslie, A., B. Dennis, A. Shih, P. Chamberlin, R. Mewaldt, C. Moore, G. Share, A. Vourlidas and B. Welsch (2012). 'Global energetics of thirty-eight large solar eruptive events'. In: *The Astrophysical Journal* 759.1, p. 71.

Ferrente, F., F. Zuccarello, S. Guglielmino, S. Criscuoli and P. Romano (2023). 'Photospheric and Chromospheric Magnetic Field Evolution during the X1. 6 Flare in Active Region NOAA 12192'. In: *The Astrophysical Journal* 954.2, p. 185.

Fletcher, L. and H. Hudson (2008). 'Impulsive phase flare energy transport by large-scale Alfvén waves and the electron acceleration problem'. In: *The Astrophysical Journal* 675.2, p. 1645.

Fletcher, L., B. R. Dennis, H. S. Hudson, S. Krucker, K. Phillips, A. Veronig, M. Battaglia, L. Bone, A. Caspi, Q. Chen et al. (2011). 'An observational overview of solar flares'. In: *Space Science Reviews* 159, pp. 19–106.

Garcia, H. A. (1994). 'Temperature and emission measure from GOES soft X-ray measurements'. In: *Solar Physics* 154.2, pp. 275–308.

Gontikakis, C., I. Kontogiannis, M. Georgoulis, C. Guennou, P. Syntelis, S. Park and E. Buchlin (2020). 'Differential emission measure evolution as a precursor of solar flares'. In: *arXiv preprint arXiv:2011.06433*.

Hayes, L. A., O. S. O'Hara, S. A. Murray and P. T. Gallagher (2021). 'Solar flare effects on the earth's lower ionosphere'. In: *Solar Physics* 296.11, p. 157.

Hinterreiter, J., A. M. Veronig, J. K. Thalmann, J. Tschernitz and W. Pötzi (2018). 'Statistical properties of ribbon evolution and reconnection electric fields in eruptive and confined flares'. In: *Solar Physics* 293.3, p. 38.

Hirayama, T. (1974). 'Theoretical model of flares and prominences: I: Evaporating flare model'. In: *Solar Physics* 34, pp. 323–338.

Hodgson, R. (Nov. 1859). 'On a curious Appearance seen in the Sun'. In: *MNRAS* 20, pp. 15–16. doi: 10.1093/mnras/20.1.15.

Hoeksema, J. T., Y. Liu, K. Hayashi, X. Sun, J. Schou, S. Couvidat, A. Norton, M. Bobra, R. Centeno, K. Leka et al. (2014). 'The Helioseismic and Magnetic Imager (HMI) vector magnetic field pipeline: Overview and performance'. In: *Solar Physics* 289.9, pp. 3483–3530.

Holman, G. D., M. J. Aschwanden, H. Aurass, M. Battaglia, P. C. Grigis, E. P. Kontar, W. Liu, P. Saint-Hilaire and V. V. Zharkova (2011). 'Implications of X-ray observations for electron acceleration and propagation in solar flares'. In: *Space science reviews* 159.1, p. 107.

Hudson, H. (2000). 'Implosions in coronal transients'. In: *The Astrophysical Journal* 531.1, p. L75.

Hudson, H., G. Fisher and B. Welsch (2008). 'Flare energy and magnetic field variations'. In: *Subsurface and Atmospheric Influences on Solar Activity*. Vol. 383, p. 221.

Hudson, H. S. (2011). 'Global properties of solar flares'. In: *Space Science Reviews* 158.1, pp. 5–41.

Janvier, M., G. Aulanier, V. Bommier, B. Schmieder, P. Démoulin and E. Pariat (2014). 'Electric currents in flare ribbons: observations and three-dimensional standard model'. In: *The Astrophysical Journal* 788.1, p. 60.

Ji, A., X. Cai, N. Khasayeva, M. K. Georgoulis, P. C. Martens, R. A. Angryk and B. Aydin (2023). 'A systematic magnetic polarity inversion line data set from SDO/HMI magnetograms'. In: *The Astrophysical Journal Supplement Series* 265.1, p. 28.

Jing, J., J. Chae and H. Wang (2007). 'Spatial distribution of magnetic reconnection in the 2006 December 13 solar flare as observed by Hinode'. In: *The Astrophysical Journal* 672.1, p. L73.

Johnstone, B., G. Petrie and J. J. Sudol (2012). 'Abrupt longitudinal magnetic field changes and ultraviolet emissions accompanying solar flares'. In: *The Astrophysical Journal* 760.1, p. 29.

Kazachenko, M. D., M. F. Albelo-Corchado, C. A. Tamburri and B. T. Welsch (2022a). 'Invited review: short-term variability with the observations from the helioseismic and magnetic imager (HMI) onboard the solar dynamics observatory (SDO): insights into flare magnetism'. In: *Solar Physics* 297.5, p. 59.

Kazachenko, M. D., B. J. Lynch, A. Savcheva, X. Sun and B. T. Welsch (2022b). 'Toward improved understanding of magnetic fields participating in solar flares: statistical analysis of magnetic fields within flare ribbons'. In: *The Astrophysical Journal* 926.1, p. 56.

Kazachenko, M. D., B. J. Lynch, B. T. Welsch and X. Sun (2017). 'A database of flare ribbon properties from the Solar Dynamics Observatory. I. Reconnection flux'. In: *The Astrophysical Journal* 845.1, p. 49.

Kleint, L. (2016). 'First detection of chromospheric magnetic field changes during an X1-flare'. In: *The Astrophysical Journal* 834.1, p. 26.

Kolmogorov, A. (1933). 'Sulla determinazione empirica di una legge didistribuzione'. In: *Giorn Dell'inst Ital Degli Att* 4, pp. 89–91.

Kopp, R. and G. Pneuman (1976). 'Magnetic reconnection in the corona and the loop prominence phenomenon'. In: *Solar Physics* 50, pp. 85–98.

Lang, K. R. (2001). *The Cambridge encyclopedia of the Sun*. Cambridge University Press.

Lemen, J. R., A. M. Title, D. J. Akin, P. F. Boerner, C. Chou, J. F. Drake, D. W. Duncan, C. G. Edwards, F. M. Friedlaender, G. F. Heyman et al. (2012). 'The atmospheric imaging assembly (AIA) on the solar dynamics observatory (SDO)'. In: *Solar Physics* 275, pp. 17–40.

Li, L. and J. Zhang (2009). 'On the brightening propagation of post-flare loops observed by TRACE'. In: *The Astrophysical Journal* 690.1, pp. 347–357.

Li, Y., J. Jing, C. Tan and H. Wang (2009). 'The change of magnetic inclination angles associated with the X3. 4 flare on December 13, 2006'. In: *Science in China Series G: Physics, Mechanics and Astronomy* 52.11, pp. 1702–1706.

Lin, R. (2011). 'Energy release and particle acceleration in flares: Summary and future prospects'. In: *Space science reviews* 159.1, p. 421.

Liu, C., W. Cao, J. Chae, K. Ahn, D. P. Choudhary, J. Lee, R. Liu, N. Deng, J. Wang and H. Wang (2018). 'Evolution of photospheric vector magnetic field associated with moving flare ribbons as seen by GST'. In: *The Astrophysical Journal* 869.1, p. 21.

Liu, L., Z. Zhou, Y. Wang, X. Sun and G. Wang (2022). 'On the nature of the photospheric horizontal magnetic field increase in major solar flares'. In: *The Astrophysical Journal Letters* 934.2, p. L33.

Mann, G., A. Warmuth and H. Aurass (2009). 'Generation of highly energetic electrons at reconnection outflow shocks during solar flares'. In: *Astronomy & Astrophysics* 494.2, pp. 669–675.

Mariska, J. T., A. G. Emslie and P. Li (June 1989). 'Numerical Simulations of Impulsively Heated Solar Flares'. In: *ApJL* 341, p. 1067. doi: 10.1086/167564.

Metcalf, T. R., K. Leka, G. Barnes, B. W. Lites, M. K. Georgoulis, A. Pevtsov, K. Balasubramaniam, G. A. Gary, J. Jing, J. Li et al. (2006). 'An overview of existing algorithms for resolving the 180 ambiguity in vector magnetic fields: Quantitative tests with synthetic data'. In: *Solar Physics* 237.2, pp. 267–296.

Miklenic, C. H., A. M. Veronig and B. Vršnak (June 2009). 'Temporal comparison of nonthermal flare emission and magnetic-flux change rates'. In: *A&A* 499.3, pp. 893–904. doi: 10.1051/0004-6361/200810947. arXiv: 0910.1701 [astro-ph.SR].

Miller, J. A., P. J. Cargill, A. G. Emslie, G. D. Holman, B. R. Dennis, T. N. LaRosa, R. M. Winglee, S. G. Benka and S. Tsuneta (July 1997). 'Critical issues for understanding particle acceleration in impulsive solar flares'. In: *JGR* 102.A7, pp. 14631–14660. doi: 10.1029/97JA00976.

Monson, A. J., M. Mathioudakis, A. Reid, R. Milligan and D. Kuridze (July 2021). 'Flare-induced Photospheric Velocity Diagnostics'. In: *ApJ* 915.1, 16, p. 16. doi: 10.3847/1538-4357/abfda8. arXiv: 2105.02199 [astro-ph.SR].

Naus, S. J., J. Qiu, C. R. DeVore, S. K. Antiochos, J. T. Dahlin, J. F. Drake and M. Swisdak (2022). 'Correlated spatio-temporal evolution of extreme-ultraviolet ribbons and hard X-rays in a solar flare'. In: *The Astrophysical Journal* 926.2, p. 218.

Neupert, W. M. (1968). 'Comparison of Solar X-Ray Line Emission with Microwave Emission during Flares'. In: *ApJ* 153, p. L59.

Paparrizos, J. and L. Gravano (2015). 'k-shape: Efficient and accurate clustering of time series'. In: *Proceedings of the 2015 ACM SIGMOD international conference on management of data*, pp. 1855–1870.

Pesnell, W. D. (2024). 'An Interesting Correlation Between the Peak Slope and Peak Value of a Sunspot Cycle'. In: *Solar Physics* 299.2, p. 14.

Pesnell, W. D., B. J. Thompson and P. Chamberlin (2012a). *The solar dynamics observatory (SDO)*. Springer.

Pesnell, W. D., B. J. Thompson and P. C. Chamberlin (Jan. 2012b). 'The Solar Dynamics Observatory (SDO)'. In: *Sol. Phys.* 275.1-2, pp. 3–15. doi: 10.1007/s11207-011-9841-3.

Petrie, G. J. D. (Oct. 2013). 'A Spatio-temporal Description of the Abrupt Changes in the Photospheric Magnetic and Lorentz-Force Vectors During the 15 February 2011 X2.2 Flare'. In: *Sol. Phys.* 287.1-2, pp. 415–440. doi: 10.1007/s11207-012-0071-0. arXiv: 1202.4192 [astro-ph.SR].

Petrie, G. (2012). 'The abrupt changes in the photospheric magnetic and Lorentz force vectors during six major neutral-line flares'. In: *The Astrophysical Journal* 759.1, p. 50.

Petrie, G. and J. J. Sudol (2010). 'Abrupt longitudinal magnetic field changes in flaring active regions'. In: *The Astrophysical Journal* 724.2, p. 1218.

Priest, E. (2014). *Magnetohydrodynamics of the Sun*. Cambridge University Press.

Priest, E. R. and V. Titov (1996). 'Magnetic reconnection at three-dimensional null points'. In: *Philosophical Transactions of the Royal Society of London. Series A: Mathematical, Physical and Engineering Sciences* 354.1721, pp. 2951–2992.

Qiu, J. (2009). 'Observational analysis of magnetic reconnection sequence'. In: *The Astrophysical Journal* 692.2, pp. 1110–1124.

Qiu, J., W.-J. Liu and D. W. Longcope (June 2012). 'Heating of Flare Loops with Observationally Constrained Heating Functions'. In: *ApJ* 752.2, 124, p. 124. doi: 10.1088/0004-637X/752/2/124. arXiv: 1201.0973 [astro-ph.SR].

Qiu, J., D. W. Longcope, P. A. Cassak and E. R. Priest (2017). 'Elongation of flare ribbons'. In: *The Astrophysical Journal* 838.1, p. 17.

Qiu, J., H. Wang, C. Z. Cheng and D. E. Gary (Apr. 2004a). 'Magnetic Reconnection and Mass Acceleration in Flare-Coronal Mass Ejection Events'. In: *ApJL* 604.2, pp. 900–905. doi: 10.1086/382122.

Qiu, J., H. Wang, C. Cheng and D. E. Gary (2004b). 'Magnetic reconnection and mass acceleration in flare-coronal mass ejection events'. In: *The Astrophysical Journal* 604.2, pp. 900–905.

Rimmele, T. R., M. Warner, S. L. Keil, P. R. Goode, M. Knölker, J. R. Kuhn, R. R. Rosner, J. P. McMullin, R. Casini, H. Lin et al. (2020). 'The Daniel K. Inouye solar telescope–observatory overview'. In: *Solar Physics* 295.12, p. 172.

Russell, A. J. B. and L. Fletcher (Mar. 2013). 'Propagation of Alfvénic Waves from Corona to Chromosphere and Consequences for Solar Flares'. In: *ApJ* 765.2, 81, p. 81. doi: 10.1088/0004-637X/765/2/81. arXiv: 1302.2458 [astro-ph.SR].

Sarkar, A., B. Vaidya, S. Hazra and J. Bhattacharyya (2017). 'Simulating coronal loop implosion and compressible wave modes in a flare hit active region'. In: *The Astrophysical Journal* 851.2, p. 120.

Savitzky, A. and M. J. E. Golay (July 1964). 'Smoothing and Differentiation of Data by Simplified Least Squares Procedures.' In: *Anal. Chem.* 36.8, pp. 1627–1639. doi: 10.1021/ac60214a047. url: http://dx.doi.org/10.1021/ac60214a047.

Scherrer, P. H., J. Schou, R. Bush, A. Kosovichev, R. Bogart, J. Hoeksema, Y. Liu, T. Duvall, J. Zhao, A. Title et al. (2012). 'The helioseismic and magnetic imager (HMI) investigation for the solar dynamics observatory (SDO)'. In: *Solar Physics* 275, pp. 207–227.

Shibata, K. and T. Magara (2011). 'Solar flares: magnetohydrodynamic processes'. In: *Living Reviews in Solar Physics* 8.1, pp. 1–99.

Simões, P. J. A., H. S. Hudson and L. Fletcher (2015). 'Soft X-ray Pulsations in Solar Flares'. In: *Solar Physics* 290.12, pp. 3625–3646. doi: 10.1007/s11207-015-0701-2. arXiv: 1412.3045 [astro-ph.SR].

Smirnov, N. (1948). 'Table for estimating the goodness of fit of empirical distributions'. In: *The annals of mathematical statistics* 19.2, pp. 279–281.

Solanki, S. K. (2003). 'Sunspots: an overview'. In: *The Astronomy and Astrophysics Review* 11.2, pp. 153–286.

Song, Y. L., H. Tian, M. Zhang and M. D. Ding (June 2018). 'Observations of white-light flares in NOAA active region 11515: high occurrence rate and relationship with magnetic transients'. In: *A&A* 613, A69, A69. doi: 10.1051/0004-6361/201731817. arXiv: 1801.04371 [astro-ph.SR].

Sterling, A. C. and R. L. Moore (2005). 'Slow-rise and fast-rise phases of an erupting solar filament, and flare emission onset'. In: *The Astrophysical Journal* 630.2, pp. 1148–1159.

Sturrock, P. (1966). 'Model of the high-energy phase of solar flares'. In: *Nature* 211.5050, pp. 695–697.

Sudol, J. J. and J. Harvey (2005). 'Longitudinal magnetic field changes accompanying solar flares'. In: *The Astrophysical Journal* 635.1, p. 647.

Sun, X., J. T. Hoeksema, Y. Liu, M. Kazachenko and R. Chen (2017). 'Investigating the magnetic imprints of major solar eruptions with SDO/HMI high-cadence vector magnetograms'. In: *The Astrophysical Journal* 839.1, p. 67.

Tanaka, K. (1978). 'Measurement and analysis of magnetic field variation during a class 2b flare'. In: *Solar Physics* 58.1, pp. 149–163.

Tavenard, R., J. Faouzi, G. Vandewiele, F. Divo, G. Androz, C. Holtz, M. Payne, R. Yurchak, M. Rußwurm, K. Kolar and E. Woods (2020). 'Tslearn, A Machine Learning Toolkit for Time Series Data'. In: *Journal of Machine Learning Research* 21.118, pp. 1–6. url: `http://jmlr.org/papers/v21/20-091.html`.

The SunPy Community, W. T. Barnes, M. G. Bobra, S. D. Christe, N. Freij, L. A. Hayes, J. Ireland, S. Mumford, D. Perez-Suarez, D. F. Ryan, A. Y. Shih, P. Chanda, K. Glogowski, R. Hewett, V. K. Hughitt, A. Hill, K. Hiware, A. Inglis, M. S. F. Kirk, S. Konge, J. P. Mason, S. A. Maloney, S. A. Murray, A. Panda, J. Park, T. M. D. Pereira, K. Reardon, S. Savage, B. M. Sipőcz, D. Stansby, Y. Jain, G. Taylor, T. Yadav, Rajul and T. K. Dang (2020). 'The SunPy Project: Open Source Development and Status of the Version 1.0 Core Package'. In: *The Astrophysical Journal* 890 (1), pp. 68–. doi: `10.3847/1538-4357/ab4f7a`. url: `https://iopscience.iop.org/article/10.3847/1538-4357/ab4f7a`.

Toriumi, S., C. J. Schrijver, L. K. Harra, H. Hudson and K. Nagashima (2017). 'Magnetic properties of solar active regions that govern large solar flares and eruptions'. In: *The Astrophysical Journal* 834.1, p. 56.

Veronig, A., M. Temmer, A. Hanslmeier, W. Otruba and M. Messerotti (2002a). 'Temporal aspects and frequency distributions of solar soft X-ray flares'. In: *Astronomy & Astrophysics* 382.3, pp. 1070–1080.

Veronig, A., B. Vršnak, M. Temmer and A. Hanslmeier (2002b). 'Relative timing of solar flares observed at different wavelengths'. In: *Solar Physics* 208.2, pp. 297–315.

Wang, H. and C. Liu (2010). 'Observational evidence of back reaction on the solar surface associated with coronal magnetic restructuring in solar eruptions'. In: *The Astrophysical Journal Letters* 716.2, p. L195.

Wang, H., T. J. Spirock, J. Qiu, H. Ji, V. Yurchyshyn, Y.-J. Moon, C. Denker and P. R. Goode (2002). 'Rapid changes of magnetic fields associated with six X-class flares'. In: *The Astrophysical Journal* 576.1, p. 497.

Wang, J., C. Liu, N. Deng and H. Wang (2018). 'Evolution of photospheric flow and magnetic fields associated with the 2015 June 22 M6. 5 flare'. In: *The Astrophysical Journal* 853.2, p. 143.

Wang, J., S. Liu, X. Ao, Y. Zhang, T. Wang and Y. Liu (2019). 'Parameters Derived from the SDO/HMI Vector Magnetic Field Data: Potential to Improve Machine-learning-based Solar Flare Prediction Models'. In: *The Astrophysical Journal* 884.2, p. 175. doi: 10.3847/1538-4357/ab441b.

Wang, J., P. Simões, L. Fletcher, J. Thalmann, H. Hudson and I. Hannah (2016). 'Arcade implosion caused by a filament eruption in a flare'. In: *The Astrophysical Journal* 833.2, p. 221.

Wang, S., C. Liu, R. Liu, N. Deng, Y. Liu and H. Wang (2012). 'Response of the photospheric magnetic field to the X2. 2 flare on 2011 February 15'. In: *The Astrophysical Journal Letters* 745.2, p. L17.

Wyper, P. F., S. K. Antiochos and C. R. DeVore (2017). 'A universal model for solar eruptions'. In: *Nature* 544.7651, pp. 452–455.

Yadav, R. and M. D. Kazachenko (2022). 'A statistical study of magnetic field changes in the photosphere during solar flares using high-cadence vector magnetograms and their association with flare ribbons'. In: *SHINE 2022 Workshop*, p. 81.

Zharkova, V. V., K. Arzner, A. O. Benz, P. Browning, C. Dauphin, A. G. Emslie, L. Fletcher, E. P. Kontar, G. Mann, M. Onofri, V. Petrosian, R. Turkmani, N. Vilmer and L. Vlahos (Sept. 2011). 'Recent Advances in Understanding Particle Acceleration Processes in Solar Flares'. In: *SS* 159.1-4, pp. 357–420. doi: 10.1007/s11214-011-9803-y. arXiv: 1110.2359 [astro-ph.SR].